DEVELOPMENT OF HIGH ANGULAR RESOLUTION DIFFUSION IMAGING ANALYSIS PARADIGMS FOR THE INVESTIGATION OF NEUROPATHOLOGY

Luke Bloy

A DISSERTATION

in

Bioengineering

Presented to the Faculties of the University of Pennsylvania

in

Partial Fulfillment of the Requirements for the

Degree of Doctor of Philosophy

2012

Supervisor of Dissertation

Ragini Verma, Associate Professor, Radiology, UPenn

Graduate Group Chairperson

Beth Winkelstein, Professor, Bioengineering, UPenn

Dissertation Committee

Timothy P. L. Roberts, Profesor, Radiology, UPenn
Andrew Tsourkas, Associate Professor, Bioengineering, UPenn
Ragini Verma, Associate Professor, Radiology, UPenn
Felix Wehrli, Professor, Radiology, UPenn
Carl-Fredrik Westin, Associate Professor, Radiology, Harvard

This work is dedicated to my family:

Mom, Dad, Dory, Rob, Bonnie and Gabriel

ACKNOWLEDGEMENT

This thesis, and more importantly the research that it describes, are the culmination of more than four years of work. It would not have been possible without the support and effort of many people who have contributed to it as well as to my development as a scientist, to whom I am deeply indebted.

Firstly, I would like to thank my mentor, Dr. Ragini Verma. Ragini has always been incredibly supportive and encouraging. Our endless discussions were crucial to development of the ideas and problems central to this research, and provided valuable insight and training in the many skills required by the modern research environment.

In many ways research is a collaborative effort and I have been lucky enough to work in a lab full of excellent researchers, who have made coming to work each day both interesting and fun. For this I thank Dr. Christos Davatzikos and Dr. Verma for assembling this group of people and creating an engaging and focused atmosphere in which to work. I am particularly thankful to Madhura Ingalhalikar, Drew Parker, Alex Smith, Yasser Ghanbari and Kayhan Batmanghelich, who were a sounding board for all of my ideas, no matter how absurd, and were central to the identification and development of the good ones. I would also like to thank Mark Bergman, Evi Parmpi and Amanda Shacklett for all of their help in navigating the many facets of being a graduate student.

I never would have been able to undertake, let alone complete, this work without the love and support of my family. My parents, Bruce and Marta Bloy, have always stressed the enjoyment that comes with learning and discovery. Their unconditional love and support throughout my life has enabled me to be the person that I am today and for that I am eternally grateful. Without the support, encouragement and understanding of my wife, Bonnie, none of this would have been possible.

ABSTRACT

DEVELOPMENT OF HIGH ANGULAR RESOLUTION DIFFUSION IMAGING ANALYSIS PARADIGMS FOR THE INVESTIGATION OF NEUROPATHOLOGY

Luke Bloy

Ragini Verma

Diffusion weighted magnetic resonance imaging (DW-MRI), provides unique insight into the microstructure of neural white matter tissue, allowing researchers to more fully investigate white matter disorders. The abundance of clinical research projects incorporating DW-MRI into their acquisition protocols speaks to the value this information lends to the study of neurological disease. However, the most widespread DW-MRI technique, diffusion tensor imaging (DTI), possesses serious limitations which restrict its utility in regions of complex white matter. Fueled by advances in DW-MRI acquisition protocols and technologies, a group of exciting new DW-MRI models, developed to address these concerns, are now becoming available to clinical researchers.

The emergence of these new imaging techniques, categorized as high angular resolution diffusion imaging (HARDI), has generated the need for sophisticated computational neuroanatomic techniques able to account for the high dimensionality and structure of HARDI data. The goal of this thesis is the development of such techniques utilizing prominent HARDI data models. Specifically, methodologies for spatial normalization, population atlas building and structural connectivity have been developed and validated. These methods form the core of a comprehensive analysis paradigm allowing the investigation of local white matter microarcitecture, as well as, systemic properties of neuronal connectivity. The application of this framework to the study of schizophrenia and the autism spectrum disorders demonstrate its sensitivity sublte differences in white matter organization, as well as, its applicability to large population DW-MRI studies.

TABLE OF CONTENTS

LIST OF TABLES

LIST OF ILLUSTRATIONS

CHAPTER 1 : Introduction

The human brain consists of approximately 100 billion neurons, organized into a vastly complex network of interconnections. This network, consisting of both local neural circuits and long distance fiber pathways, is thought to provide the anatomical substrate allowing for the distributed interactions between brain regions [70, 128, 157]. While neural anatomy has been extensively studied using cerebral dissection [66, 144], relatively little is known about this complex set of connections which mediate brain function and give rise to the richness of human behavior and experience. Chemical tracing, where markers are locally injected into the cortex and their subsequent distribution is observed, has facilitated the probing of this network yielding connectivity information in many animal models [110, 145]. However, the invasiveness of this technique precludes its use in human subjects particularly, within a clinical setting.

More recently, diffusion weighted magnetic resonance imaging (DW-MRI) has emerged as the prominent noninvasive methodology able to quantitatively probe neuronal white matter (WM), enabling the *in-vivo* investigation of tissue microstructure and organization. By describing the average molecular diffusion of water molecules, DW-MRI probes tissue structure at biological scales typically unavailable to noninvasive imaging techniques. The fact that water molecules in highly organized fibrous tissues, such as neuronal WM, diffuse preferentially along fibers, allows DW-MRI to obtain information related to the local tissue architecture. This knowledge of the local WM organization can also be extrapolated to infer global patterns of neuronal connectivity, previously available only via dissection, as in Figure 1.1, or chemical tracing techniques. The ability to investigate both local architecture and global structural connectivity, *in-vivo*, has garnered DW-MRI an important place in many clinical studies focused on evaluating WM tissue structure, fidelity and development.

As a field of research, DW-MRI is relatively new. While diffusion sensitivity has long been used within magnetic resonance (MR) spectroscopy [158, 159], it was not until the mid 1980s [23, 115, 184] that it began to be used to study neuronal WM. Since that time, the

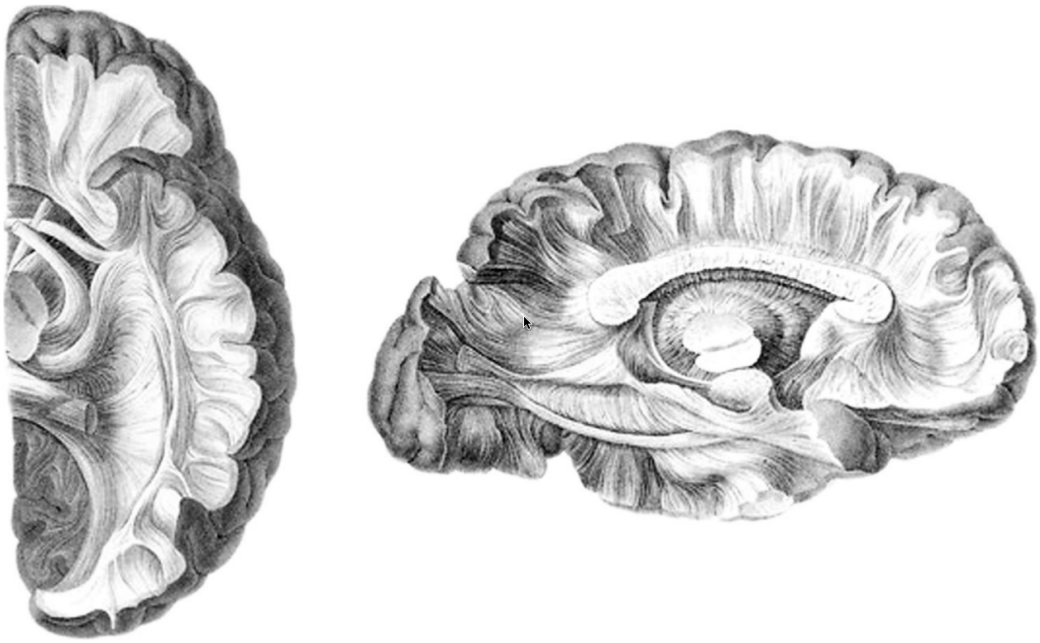

Figure 1.1: Illustrations by Friedrich Arnold [10] of gross dissections of the cerebral hemisphere. From [145, Schmahmann2007a].

complexity of the mathematical models used to represent the diffusion signal has continually increased. Initially a single scalar, the apparent diffusion coefficient (ADC) [23], was used to measure the degree of diffusion at each voxel. Subsequent improvements in MR hardware and image acquisition have led to improved signal to noise (SNR), enabling a more formal treatment of *in-vivo* diffusion, the diffusion tensor (DT) model [17], to be developed.

The use of a Gaussian distribution of molecular displacements allows diffusion tensor imaging (DTI) to model molecular diffusion in three dimensions enabling researchers to quantitatively investigate the amount of diffusion per voxel (the ADC), its anisotropy (the acuteness of its directionality), as well as its spatial orientation. The more robust information available from the DT model has proved to be very useful in the study of both normal and pathological brains, as discussed in section 2.4. DTI is now routinely included in research protocols studying a range of pathologies, such as multiple sclerosis [35, 75], schizophrenia [96], autism [26, 87], as well as normal development [64].

Despite the growing foothold of DTI within the imaging community, the DT model is not

without limitations. Most importantly, its dependence on a single Gaussian distribution limits its ability to model architectures with multiple fiber orientations. Voxels with a more complex microarchitecture, such as fiber crossings or fanning configurations, are thus poorly characterized. This represents a serious limitation, as it is currently thought that between one and two thirds of the WM voxels [21], at the current clinical resolutions of 1-3 mm isotropic, show evidence of complex fiber organization [133, 174]. The recognition of this limitation has led to the development of a group of more complex diffusion models that are better able to describe the complexities of these tissue architectures.

Diffusion spectrum imaging (DSI) exploits the Fourier relationship [172, 183, 181] between the DW-MRI signals and the underlying diffusion process to compute a three dimensional probability distribution function (PDF), at every imaging voxel, describing the local diffusion process. In an attempt to reduce the high data acquisition requirements of DSI, other models have been introduced that have lower acquisition requirements. The most prominent, the orientation distribution function (ODF) [2, 47, 170, 173] and the fiber orientation distribution (FOD) [8, 168], require a single shell DW-MRI acquisition and are often referred to as high angular resolution diffusion imaging (HARDI) [173] diffusion models.

The anatomical differences that occur in many neurological disorders, particularly neuropsychiatric disorders, are often subtle and diffuse in nature and requires the use of large group studies to identify them. With as many as two thirds of the WM voxels consisting of complex architectures, the improved modeling ability offered by these new techniques will presumably translate to benefits in quantifying group differences and improved understanding of neurological disorders. The achievement of such gains necessitates the development of high throughput processing and analysis methods and algorithms capable of leveraging this additional information. Much of the research effort to date has concentrated on the development of these diffusion models and on the acquisition schemes that facilitate their use. Unfortunately, the development of analytic tools, required for population studies, has not kept pace with the improved higher order data acquisition, greatly limiting their adoption for studying neural pathologies and diseases.

The focus of this thesis is the development of such an analysis framework. Two types of analysis are enabled by the methods developed here. First, local features derived directly from the diffusion models can be used to investigate regional differences in WM architecture. This necessitates the establishment of the spatial correspondence between the WM anatomy of each subject, which is accomplished through the developed HARDI-based spatial normalization process. Homogeneous WM regions of interest (ROIs) can then be defined by parcellating the WM volume based on its local architecture, thereby enabling the generation of population specific atlases and facilitating regional statistics. The second type of analysis, is achieved through the development of a structural connectivity algorithm. Registration is again used to establish spatial correspondence between subjects, in this case between the gray matter (GM) nodal regions. This correspondence enables the direct statistical analysis of the connection strengths, in addition to the analysis of the global topological features of these networks. Combined, these tools form the core of a HARDI neuroimaging toolkit, from which more complex statistical analysis methods can be developed in the future.

In designing any analysis framework, care must be taken with the initial decision of which data models will be utilized going forward. The framework being presented in this thesis is based around diffusion models that can be expressed as real-valued symmetric functions defined on the unit sphere. This includes three of the most prominent HARDI models, the ADC profile, the ODF and the FOD. These functions are naturally represented by their real spherical harmonic (RSH) expansions, allowing for the development of a general framework based solely on the properties of the real spherical harmonics. While algorithms presented here are applicable to any diffusion model representable in the RSH, the FOD was utilized both in their individual validation, as well as, in the clinical applications that were performed. A number of factors contributed to this choice. Principal among them is the interpretability of the FOD, as describing the orientation of fibers, as well as its applicability to a wide range of b-values as can be seen in Figure 1.2 adapted from [168].

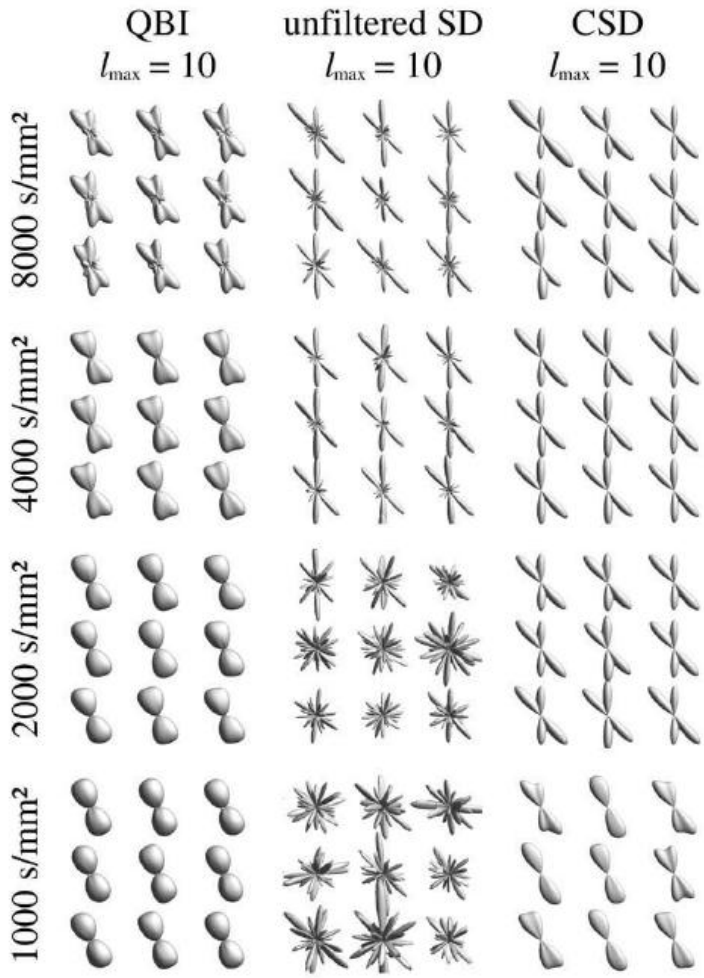

Figure 1.2: Orientation distribution function (QBI) and FODs computed with spherical deconvolution and constrained spherical deconvolution, are shown for a range of b-values. The CSD produces more robust profiles then either the QBI or the SD. Adapted from [168, Tournier 2008].

Organization and Contributions of this Thesis

The following chapter discusses the development of DW-MRI modeling leading to the HARDI diffusion models that are used in this work, including some of the insights that have been gained through the application of DTI to a number of different clinical populations. This overview allows us to identify the key algorithms required for successful population studies which are currently lacking in the HARDI community. The mathemat-

ics of the RSH basis functions, that form the core of our analysis methods, are discussed in Appendix B. In combination, these present the requisite background information required to place the remainder of this work in context. The main contributions of the thesis are then presented as independent chapters.

The spatial normalization method, presented in Chapter 3, utilizes the RSH coefficients of the FOD data model to inform a diffeomorphic Demons registration framework used to align each subject's anatomy with that of a template subject. The method is a two phase framework, using an orientation invariant approach in the initial phase followed by an orientation sensitive secondary phase. Simulation studies show that this overall approach is able to maintain the registration accuracy achieved from the more intensive orientation sensitive method, in reduced computational time. The proposed approach is also compared with state of the art DTI-based registration techniques, illustrating the ability of the HARDI based approach to better align the WM anatomy, as indicated by lower population variances, lower residuals and improved overlap of the population's WM volumes.

Chapter 4 describes a data-driven WM parcellation algorithm which utilizes local variations in an FOD image to delineate regions of homogeneous tissue architecture. This approach allows the generation of population specific atlases at various levels of granularity, enabling researchers to tailor the process to their specific application. The use of a local similarity measure and an iterative process, focused on minimizing regional variance, yields ROIs that are more homogeneous then those typically available from anatomically defined atlases.

The final methodological development, presented in Chapter 5, revolves around the use of network models to represent the structural connectivity of an individual. The HARDI-based method utilizes efficient algorithms and physiologically inspired constraints to compute network models from the FOD images of each subject. These models are shown to be highly repeatable within the same subject while retaining that ability to discriminate between the connectivity patterns of different individuals, a critical trait for any measure to be used to differentiate clinical populations.

It should be noted that while the above methods were all developed and validated using the FOD diffusion model, they can be seamlessly applied to any spherical diffusion model possessing a representation in the RSH basis. This ability provides a simple means for evaluating the utility of the alternate diffusion models within the context of a group study, while controlling for the analysis methods being used.

Finally, the utility of these methodologies to elucidate group differences is demonstrated through the investigation of two disorders, schizophrenia and autism, thought to possess a degree of aberrant connectivity. These studies illustrated the ability of the proposed methods to localize differences in both the WM microstructure and in the patterns of structural connectivity. While these preliminary findings are intriguing, additional studies with larger numbers of subjects are needed to replicated them. None the less, these studies serve as validation that the proposed methods are able to capture group differences and provide a solid basis from which additional analysis may be performed.

Software Contributions

The overarching goal of the project is the development of methodologies enabling the use of HARDI within clinical group studies. As such, the dissemination of these tools and ideas both to our clinical collaborators and to the medical image analysis community as a whole, is of importance. In order to facilitate this process, the software developed as part of this project utilizes available open source software libraries [132] where possible. The majority of the algorithms presented in this manuscript are now available upon request.

CHAPTER 2 : Diffusion Weighted MRI in Neuroimaging

The focus of this thesis is the development of an analysis framework enabling the use of HARDI diffusion models within research studies of human WM and neuropathology. It is important to recognize that since DW-MRI became a viable *in-vivo* imaging modality in the early 1990s, the mathematical tools being used to investigate and model diffusion in the brain have undergone continuous development. The purpose of this chapter is to present this development with a particular focus on those models that are applicable to the framework developed in this thesis. Additionally, we present some of the insights that have been garnered using DTI within population studies, suggesting areas where the more complex HARDI modeling may be particularly beneficial.

2.1. Principles of DW-MRI

All particles, at temperatures above absolute zero, undergo random Brownian motion. Within populations or ensembles of particles, this random motion results in a diffusion process, where the population of particles gradually spreads. When concentration gradients exist this process explains the net movement of particles from regions of higher concentration to those of lower concentrations, although diffusion also occurs in the absence of a concentration gradient.

Statistically, the diffusion process has been well characterized by Einstein [53], who described diffusion in a free medium, using basic linear differential equations, showing that molecular displacements (x) in a given time frame obey a three dimensional Gaussian distribution governed by the diffusion coefficient, D. The diffusion coefficient is affected by the particle's size and temperature, as well as the viscosity of the surrounding medium. In the absence of a concentration gradient the average particle displacement, $\langle x \rangle$, is zero. However the average mean squared distance that each particle travels in a time (τ_d), is

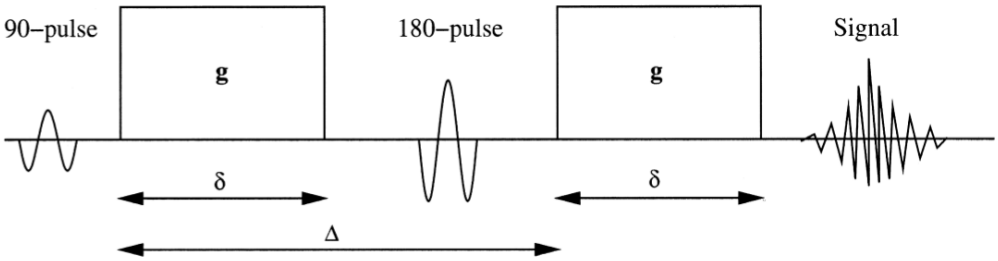

Figure 2.1: The Stejskal and Tanner pulsed gradient spin echo sequence. Adopted from [185, Westin2002]

directly related to the diffusion coefficient:

$$\langle x^2 \rangle = 6D\tau_d$$

DW-MRI's sensitivity to the diffusion process is due to the introduction, by Stejskal and Tanner [158], of a series of diffusion encoding pulse sequences prior to either a spectroscopic readout or an imaging pulse sequence. The most basic pulse sequence demonstrating this pre-encoding block, is the pulsed gradient spin echo (PGSE) sequence (seen in Figure 2.1). The diffusion sensitivity is due to a pair of balanced linear gradients separated by a 180° pulse. These gradient pulses, separated by a time Δ, are applied along the direction $\mathbf{u}$ with a strength g for a duration of δ. The first gradient imparts each spin with a phase proportional to its location along the encoding direction. The 180° pulse inverts the spins allowing the second gradient, balanced in respect to time and magnitude, to refocus the spins. Those spins that do not experience any displacement along $\mathbf{u}$, during the time separating the two gradient lobes, are completely refocused. However, those that have diffused along $\mathbf{u}$ experience a slightly different field strength during the second gradient lobe than was experienced during the first resulting in an incomplete rephasing and a subsequent signal loss.

If we assume that water molecules undergo 'free' diffusion, meaning that it can be well described by a three dimensional Gaussian with a constant diffusion coefficient, D, then the

subsequent signal can be expressed by the common form of the Stejskal-Tanner equation:

$$S(\mathbf{u}) = S_0 e^{-bD} \tag{2.1}$$

where $S(\mathbf{u})$ is the measured signal resulting from a gradient direction of $\mathbf{u}$, S_0 is the signal in the absence of diffusion sensitive gradients (often referred to as a b0 image in DW-MRI). D is the diffusion coefficient or when used to describe the average response from a DW-MRI voxel, the apparent diffusion coefficient (ADC). The 'b-value' [23],

$$b = \gamma^2 \delta^2 \left(\Delta - \frac{\delta}{3} \right) g^2$$

is related to the gradient strength (g), the gyromagnetic ratio of water protons (γ) as well as the pulse duration (δ) and separation (Δ). Typical DW-MRI acquisitions utilize Δs on the order of 30-60 ms, meaning that DW-MRI is probing the tissue microstructure on length scales in the 23–32 μm range (assuming a $D = 3\text{x}10^{-3}$mm/s), a scale much smaller then those available from other in-vivo imaging modalities.

It is important to note that each diffusion weighted image (DWI) is sensitive to a single diffusion direction, however, diffusion is a three dimensional process and water displacements may not be uniform in all directions [122]. This anisotropic diffusion may be due to the local tissue organization, such as membranes or other obstacles impeding diffusion in certain directions. The desire to account for this phenomenon has led to the development of a diffusion model capable of capturing the true anisotropic nature of the water diffusion in biological tissue, the DT model [17].

2.2. The Diffusion Tensor Model

At the present time, the most widely accepted form of DW-MRI, utilizes the DT data model to represent the diffusion process at each location. The DT model treats the diffusion process

within each imaging voxel as full three dimensional Gaussian process of the form:

$$P(x,\tau) = \frac{1}{4\pi\tau 3|D|} e^{\frac{-1}{4\tau}x^t \mathbf{D} x} \tag{2.2}$$

where the probability of a displacement, x, occurring in a time τ is controlled by a symmetric 3x3 covariance matrix describing the Brownian motion of water molecules at each imaging voxel, the diffusion tensor ($\mathbf{D}$). Using this form, the solution to the Stejskal-Tanner equation is:

$$S(\mathbf{u}) = S_0 e^{-b\mathbf{u}^t \mathbf{D}\mathbf{u}} \tag{2.3}$$

The symmetric nature of the DT means that it posseses six unknown elements that must be estimated from the DWIs, requiring a minimum of six DWIs be acquired using non-colinear gradient directions, in addition to a single b0 image. Estimating the DT from these measurements has been extensively studied, with proposals ranging from traditional linear least squares approaches, to more sophisticated methods that account for the strict positivity of the diffusion process [11, 54].

The largest benefit of the DT model is its ability to characterize the local diffusion process using measures beyond the ADC, which can be computed as 1/3 of the trace of the DT. An eigensystem analysis can be used to diagonalize the DT, identifying the principal diffusion directions (the eigenvectors), as well as, the diffusivity in those directions (the eigenvalues, λs). This yields information concerning both the shape and orientation of the diffusion process. Additionally, many scalars have been introduced to quantify the amount of anisotropic diffusion that is present in each voxel. For instance, the linear anisotropy (CL), planar anisotropy (CP), and spherical anisotropy (CS), have been proposed [185] to measure different types of anisotropy in each voxel. However, the most widely accepted measure remains the fractional anisotropy (FA) [19]. The FA measures the severity of the anisotropy of the DT by:

$$FA = \sqrt{\frac{3}{2}\frac{(\lambda_1 - \bar{\lambda})^2 + (\lambda_2 - \bar{\lambda})^2 + (\lambda_3 - \bar{\lambda})^2}{\lambda_1^2 + \lambda_2^2 + \lambda_3^2}} \tag{2.4}$$

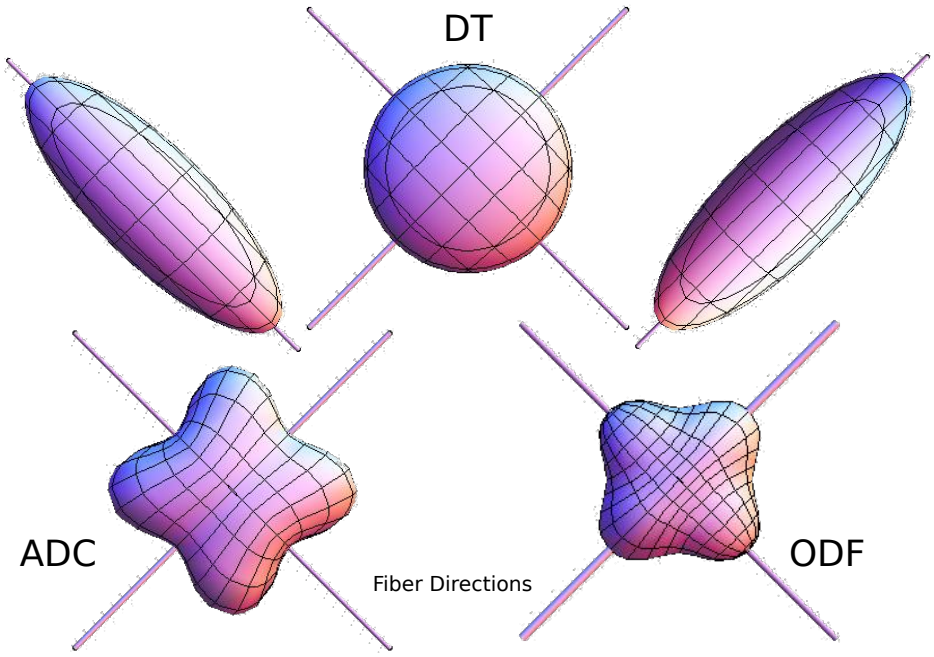

Figure 2.2: A simulated example of a simple crossing geometry where two fiber pathways intersect at 90°. As can be seen the DT model is able to identify the fiber plane but is unable to distinguish the individual peaks representing each fiber population whereas the HARDI models, ODF and ADC, are better able to capture the complex structure. Only the peaks of the ODF align with the simulated fiber directions.

where λ_1, λ_2 and λ_3 are the eigenvalues of the DT.

In addition to providing a mathematical treatment of diffusion anisotropy in biological tissue, the DT model allowed researchers to begin to quantitatively investigate the local orientation of the tissue architecture. The most obvious utilization of this is the development of tractography algorithms, that utilize this orientational information to trace the anatomical fiber bundles that connected the brain. The first approaches [101, 118] used simple propagation algorithms, that generate streamlines from the principal diffusion directions at each voxel. Later, probabilistic methods were introduced [22, 73], which account for the uncertainties in determining the principal diffusion direction. These algorithms provided the first steps toward the *in-vivo* investigation of the network of anatomical connections that make up the brain.

The improved modeling fidelity of the DT has led to the increased ability to discern differences in WM structure, which in turn has benefited the study of many neurological processes, discussed below in Section 2.4. Despite this, the DT model is not without limitations. Most critically, the underlying assumption of a single diffusion Gaussian PDF (equation 2.2), limits the DT's ability to model WM geometries with more than one principal diffusion direction. Figure 2.2 illustrates this example for a simple crossing geometry, where two fiber pathways intersect at 90°. As can be seen, the DT model is able to identify the fiber plane but is unable to distinguish the individual peaks representing each fiber population. In contrast, the more complex HARDI models are better able to capture this complex structure. This limitation hinders the DT's ability in modeling voxels with complex geometries, such as crosses, branchings, fannings, etc., prompting the need for improved modeling approaches.

2.3. Beyond the DT Model

While many of the limitations of the DT model were understood early in the adaptation of DTI, it wasn't until 1999 that they were first illustrated within human WM tissue [174]. Since that time, a large effort has gone into the development of more complex higher order models of diffusion, as well as, the acquisition strategies to provide the data they require.

2.3.1. Q-Space Imaging

While the signal models of DTI and ADC imaging (equations 2.3 and 2.1) utilize a Gaussian approximation (Equation 2.2) of the diffusion process at each voxel to model the DW-MRI signal, it is possible to utilize DW-MRI in a model free way. If the width of each gradient lobe is assumed to be small compared to the separation of the lobes ($\delta << \Delta$) then the signal resulting from a PGSE sequence ($S(\mathbf{q}, \tau)$) can be expressed as the 3-dimensional Fourier transform $\mathcal{F}$ of the diffusion PDF, P,

$$S(\mathbf{q}, \tau) = S_0 \int_{\mathbb{R}} P(\mathbf{x}, \tau) e^{-2\pi i \mathbf{q}^t \mathbf{x}} dr = \mathcal{F}[P(x, \tau)] \tag{2.5}$$

where $\mathbf{q} = \gamma\delta\mathbf{u}/2\pi$, with γ being the water proton gyromagnetic ratio, and $\mathbf{u}$ the direction of the applied gradient. The Fourier relationship between the measured signal intensity and diffusion PDF implies that by performing many measurements with different gradient orientations and strengths, fully sampling the 3-dimensional $\mathbf{q}$-space, researchers can use the inverse Fourier transform to investigate the local diffusion process in a model free way [33].

Single dimensional q-space imaging (QSI), where measurements are acquired only in the radial direction, has been used to investigate the local geometry of porous materials [32], as well as, the axonal architecture (principally the axon diameter) [15, 125]. Full 3-dimensional acquisitions requiring a large number of radial and angular measurements, along with the 3-dimensional Fourier transform, have been performed under the name of DSI [106, 172, 182]. While in many ways this approach represents the most theoretically complete form of DW-MRI, its data requirements currently make it ill suited for use within clinical research studies. The key drawback is the requirement of a rectilinear sampling of $\mathbf{q}$-space, which requires many measurements with very large gradient strengths. Current research into compressed sensing [48, 99, 114] has shown promise at reducing these requirements but has yet to develop into a reliable alternative. Other attempts to deal with this practical limitation have prompted the development of approaches that utilize data acquired on a single shell of $\mathbf{q}$-space but with a higher angular resolution (HARDI) than was typically utilized in DTI.

2.3.2. Single Shell HARDI

The data acquisition scheme underlying HARDI is relatively straight forward. Essentially, a large number of DWIs are acquired, all with the same b-value, with the gradient directions chosen to evenly sample a sphere. In fact, DTI acquisitions are single shell approaches, although generally the term HARDI is reserved for acquisitions that use b-values above $1500\,\mathrm{s/mm^2}$. The b-values typically used in HARDI acquisitions range between $b = 2000\,\mathrm{s/mm^2}$ and $b = 4000\,\mathrm{s/mm^2}$, although HARDI data models have successfully

been applied to lower b-value ($b = 1000\,\mathrm{s/mm^2}$) datasets. The use of smaller b-values, relative to those used in DSI ($b = 20000\,\mathrm{s/mm^2}$ [182]), combined with the lower required number of samples makes these data acquisitions more feasible within a clinical setting. A number of higher order diffusion models have been developed to take advantage of this type of data. The most prominent are discussed below.

The Apparent Diffusion Coefficient Profile

One of the first uses of DW-MRI was the characterization of the diffusion process by the ADC value (equation 2.1). This approach can be extended by treating the ADC as a continuous function as opposed to a constant, leading to the following definition of the ADC profile:

$$D(\hat{\mathbf{u}}) = -\frac{1}{b} Log \frac{S(\hat{\mathbf{u}})}{S_0}$$

There are 2 common and equivalent representations of the ADC profile. First is the representation of the ADC profile as an l^{th} order fully symmetric Cartesian tensor [126]. This representation reduces to the DT model when $l = 2$. The second representation is as a RSH series [3, 57]. There are a number of drawbacks to the ADC model, mainly the extraction of orientation information is hindered by the fact that the maxima of the ADC profile (see Figure 2.2) do not necessarily coincide with the underlying fiber directions [195], preventing its clear interpretation in terms of physiology.

Q-ball imaging

In contrast to QSI or DSI where the Fourier relationship between the signal and the diffusion PDF is used to compute the complete PDF in 3-dimensions, q-ball imaging (QBI) [172] attempts to compute only the radial projection of the PDF, the ODF, from a HARDI dataset. The ODF describes the probability that a water molecule will diffuse along a particular direction. A number of estimation strategies have been proposed. The most popular utilize the Funk-Radon transform in spherical coordinates [47, 83] to relate the ODF to the measured signals. Recently improved techniques have been proposed [2, 170]

to better marginalize the ODF yielding a sharper profile. Unlike the ADC profile, the correspondence between the peaks of the ODF and the principal directions of the underlying fibers, has been established experimentally [130].

Fiber Orientation Distribution

The FOD HARDI data model [8, 167] represents the DW-MRI signal as the spherical convolution of the FOD and a fiber impulse response (FIR). The FIR describes the DW signal that would be measured for a single fiber or fiber bundle aligned along the z-axis, and is computed from the subject's DW-MRI data. The FOD contains information relative to both the orientation of any fiber bundles that may be present and partial volume fractions relating these different fiber populations.

Since the FOD is of particular interest to the work presented here, its estimation is discussed in additional detail. The FOD estimation is based on the process of spherical deconvolution (SD) [78, 166, 167]. The coefficients of the DW-MRI signal's RSH expansion ($\tilde{S}$) are related to those of the FOD ($\tilde{F}$) by $\tilde{S} = \mathbf{H}\tilde{F}$, where $\mathbf{H}$ is a square matrix representing the l^{th} order rotational harmonic decomposition of the FIR. The FOD can be computed as $\tilde{F} = \mathbf{H}^{-1}\tilde{S}$. The FIR is determined for each subject, by first finding the voxels with high fractional anisotropy (> 0.6). The directionality of the diffusion process is removed from $\tilde{S}$ by aligning the major eigenvector of a diffusion tensor model with the z-axis. The signal profiles are then averaged to create the FIR.

A drawback of the spherical deconvolution method is that $\mathbf{H}$ is often ill-conditioned, making the deconvolution process unstable in the presence of noise. To counter this, a constrained spherical deconvolution (CSD) method [166] is often used to compute the FOD. The CSD recognizes the fact that the FOD is a positive function. It iteratively performs the SD process, where constraints are added to $\mathbf{H}$, at each iteration, to encourage positivity.

Mixture Models

In addition to the estimation methods mentioned above, a number of researchers have proposed the utilization of mixture models [113, 138] to describe the diffusion process at each imaging voxel. The most popular of these are the multi-tensor models [95, 129] where the DW-MRI signal is modeled as a linear combination of different DTs. An advantage of this approach is that common terms, such as FA, are directly applicable. They do typically require the number of components being modeled to be fixed, resulting in possible inaccuracies when modeling voxels with a different configuration. An example of such a situation would be the modeling of a single fiber bundle by a three tensor model. Additionally these approaches require multiple b-value acquisitions to fully determine multiple tensors in a single voxel [142, 143].

2.4. Applications of DW-MRI in Clinical Populations

Since its introduction, DW-MRI has offered researchers unique insight into the structure and fidelity of neuronal WM. As it has matured the percentage of neuroimaging research protocols that include a form of DW-MRI, has continued to increase. While the majority of these studies utilize DTI to characterize the local diffusion process, the proportion of studies including HARDI acquisitions is beginning to rise. Here we highlight some of the central findings of these studies illustrating DW-MRI's potential to elucidate group differences in the local and global architecture of the human brain.

2.4.1. Stroke

By far the most clinically significant application of DW-MRI has been in the realm of identifying acute brain ischemia and managing the care of stroke patients. Cat models were initially used to demonstrate water diffusivity decreases of 30% – 50% [116, 121] in ischemic tissue within minutes of the occlusion of the middle cerebral artery. This finding was confirmed in other animal models [155] and later in human stroke patients [154]. The ability to identify ischemia during this early window, is particularly critical as many treatment

options are only viable within this early time frame. While the physiological interpretation of this decrease is not completely understood [155], DW-MRI remains the main imaging modality used to monitor patient progress and predict clinical outcome.

2.4.2. Neural Development

The investigation of normal development of the brain has been a recent topic of study. While longitudinal studies are still rare, there have been a number of cross sectional studies to investigate WM development. DTI lifespan studies have shown that FA values in WM increase during adolescence and early adulthood, peaking roughly around 33 years of age [76]. This parabolic increase is followed by an equally gradual decrease. Not all fiber pathways develop with identical FA trajectories, pathways connecting the frontal and temporal lobe develop latest [102], while those thought to involve more critical processing, such as, the corpus callosum (CC), the inferior longitudinal fasciculus (ILF) and the fornix develop earlier.

Structural connectivity models have also been utilized to study differences in the organizational properties of the neural networks with age. Gong et al. [64], focused on changes across the entire lifespan (19 – 84 years) finding decreases in cortical regional efficiency, particularly in the parietal and occipital neocortex with increases in the frontal and temporal regions. Global efficiencies did not show significant changes. Hagmann et al. [72], focused on adolescent development (2 – 18 years), finding increases in global efficiency, node strength and decreases in clustering coefficient. This suggests that the overall effect of development on network properties is increased network integration and decreased segregation.

2.4.3. Schizophrenia

One of the more dominant hypotheses concerning the etiology of schizophrenia centers on disruptions of neuronal connectivity [29, 58]. Due to this fact, DTI has been extensively used to study schizophrenia's affect on neuronal WM. The majority of these studies have shown local decreases in FA in a variety of regions [164]. The most consistent of these findings are

decreases in the cingulate, the CC and frontal WM [96, 186], while the superior longitudinal fasciculus (SLF), the inferior fronto-occipital fasciculus (IFOF) and the uncinate have also been implicated. It is important to note that these finding have not been consistent in all studies [186], however the general theme of these results indicate a reduction in WM integrity, as measured by FA. Connectivity analysis has demonstrated altered topological properties of the brain networks of schizophrenic patients as compared to controls. Again the overall picture resulting from these studies is one of a decrease in global network efficiency [179, 194] with decreases in regional efficiency found in frontal [175, 179, 194] regions and limbic regions [194].

2.4.4. Autism

The autism spectrum disorders (ASDs) are developmental disorders characterized by impaired social interaction, impaired communication abilities and repetitive behaviors. Increasingly, they are being viewed as disorders of functional networks suggesting that DW-MRI may provide critical insights into their neuropathology. In the last 5 years, DTI has been increasingly used to study children diagnosed with autism spectrum disorder (ASD). This work suggests reduced FA and increased ADC, often referred to as mean diffusivity, in subjects diagnosed with ASD. While there has been some variability in reported findings, the predominant pattern is one of compromised WM of the frontal and temporal lobes [6, 104, 161]. Tract and region based analysis has implicated the ILF, the IFOF and the SLF [123, 150, 151], as well as, the CC and cortical spinal tract (CST). The more complex structural connectivity models are just now beginning to be used to study ASD, hoping to further inform the concept of ASD being a connectivity disorder [42].

2.4.5. Other

The pathologies discussed in the preceding sections are by no means exhaustive. DW-MRI has been used to study numerous other disorders such as Dyslexia, Attention deficit hyperactivity disorder and mood disorders (see [24, 51, 164, 186] for reviews). It has also

been utilized in identifying WM lesions due to multiple sclerosis and cardiac disease, as well as in the study of brain tumors and neurosurgical planning [103, 120, 148].

2.4.6. Summary

These studies illustrate the unique ability of DW-MRI in providing *in-vivo* information related to the organization and structure of neuronal WM as it relates to disease. Despite these successes, there are a number of areas where the improved contrast offered by the HARDI data models may be particularly beneficial. The principal hindrance of the DT model is its inability to model multiple fiber populations in a single imaging voxel. The most immediate benefit of models that can describe multiple fiber populations, are the studies based on fiber tracking and connectivity. By being able to accurately track through fiber crossings, these improved models should offer more robust connectivity results in many of the pathologies mentioned above. Additionally, many of the regions identified as abnormal in the disease populations, consist of regions that traverse multiple fiber architectures and are thus poorly modeled by DTI. This fact may be result in the variability of findings seen in these regions suggesting the possibility of more robust and reliable findings when using improved modeling techniques.

2.5. The Anatomy of a Population Study

Clearly DW-MRI, in its present form of DTI, offers researcher a unique and valuable tool with which to study neural development and disease. With the exception of using ADC measurements to characterize acute brain ischemia, the majority of the analysis performed in the above mentioned studies can roughly be grouped into five categories:

1. **Voxel-Based**: The most common approach to DTI analysis is the voxel-based investigation of scalar images, generally FA or ADC, derived from the DT images of each subject. These approaches require that each image be spatially normalized into a standard template space prior to being subjected to statistical analysis.

2. **Manual ROIs**: A more time intensive approach involves the manual determination of individual WM ROIs in each subject and the subsequent statistical analysis of scalars extracted from each of these ROIs. An advantage of the manual ROI approach is that each region is determined based on the individual anatomy of the subject, perhaps reducing inter-subject variability in the ROI definition. This comes at the expense of the time consuming manual delineation step, which often limits the number of regions being investigated, resulting in studies that are highly hypothesis driven as opposed to being more exploratory.

3. **Atlas ROIs**: An alternative to the use of manually defined ROIs is the use of a WM atlas that has already been parcellated into regions. Each subject is then spatially normalized into the atlas space and regional measures are extracted and subjected to statistical analysis. The utilization of this approach clearly rests on the availability of a suitable WM atlas (defined on a similar population, containing regions that are of interest, etc) as well as, a reliable spatial normalization algorithm.

4. **Track-Based**: These approaches are in someways a variant of the manual ROI-based approaches. Essentially, fiber tracking algorithms are used to identify particular structures that are of interest. Scalars can then be computed along the points of each fiber track and investigated to determine how they vary as the fiber track advances through the anatomy [41, 65]. Alternatively, the voxels that these fibers pass through can be accumulated into an ROI allowing for statistical analysis similar to the previous two approaches.

5. **Connectivity**: The most recent analysis tool utilized in DW-MRI studies, uses fiber tractography to model the structural connectivity network. This analysis allows researches to investigate the pattern of interconnections between brain regions at a system-wide/whole brain level. The majority of this work has focused on investigating topological properties derived from these networks but the hope is that more in-depth analysis will identify specific circuits or functional systems that are affected

by pathology.

The success of these analysis approaches in elucidating the affects of pathology on neuronal WM, has been enabled by the development of image analysis methodologies that take full advantage of the DT data model. These include methods for spatial normalization/registration [68, 88, 188, 191, 197], spatial smoothing [54], tractography [18, 21, 22, 40, 101], as well as, the availability of DTI-based WM atlases [119, 124, 178].

While the HARDI data models, discussed in the Section 2.3, have improved our ability to model complex WM, their utility in the study of WM disease cannot be fully appreciated until similar analysis methods have been developed to take advantage of this improved WM contrast. For this reason, the focus of this thesis has been the development of methods critical to these analysis paradigms. Specifically, the development of HARDI-based spatial normalization and WM parcellation algorithms (Chapters 3 and 4) enable both voxel-based and atlas-based analyses, while the development of an algorithm (Chapter 5) used to extract structural connectivity measures enables the investigation of pathology effects on the connectivity patterns. The culmination of this work is the creation of analysis pipelines that will enable to the use of the prominent HARDI diffusion models within the clinical populations.

CHAPTER 3 : HARDI Spatial Normalization

3.1. Introduction

The process of spatial normalization, or image registration, lies at the center of large population based studies. Its ability to capture individual anatomical variation allows both the direct exploration of geometric and volumetric anatomical differences, as well as, the establishment of a standard coordinate frame where scalar features, such as those derived from the diffusion models (FA for instance), can be subjected to statistical analysis. The process of spatial normalization attempts to determine the anatomical correspondence between the brains of two subjects (or a subject and a template) by minimizing the differences between the two images. A direct analysis of the parameters of the spatial transforms permits a quantification of the geometric differences [13, 14, 45] between subjects, while the registered images allow for the investigation of differences not attributable to differences in geometry.

It is worth noting that the use of anatomical landmarks to achieve spatial correspondence and subsequently performing measurements on the registered images, rests on two basic assumptions. First, it assumes a relationship between global anatomy (the region's location) and the function of each region. Secondly, it assumes that this structure/function relationship is conserved between individuals. While both of these assumptions are lacking in some cases, such as in the presence of large focal pathologies such as tumors or stroke, in cases where differences due to pathology are thought to be less extreme, this approach offers the only way to address the statistical analysis of large population studies.

The imaging contrast available from structural magnetic resonance imaging (MRI) has been widely used to inform the spatial normalization process. This approach has had great success in measuring volumetric differences in GM regions, by examining the deformations directly, or in elucidating functional differences between groups via functional magnetic resonance imaging (fMRI) at either the regional or voxel level. While structural MRI provides excellent

contrast between GM, WM and cerebrospinal fluid (CSF) yielding detailed information concerning cortical anatomy, it provides considerably less information about WM anatomy [165], thereby severely limiting its use in aligning WM anatomy.

Alternatively, by providing an *in-vivo* WM contrast, DW-MRI can be used to distinguish WM structures, providing detailed anatomical information that is unavailable from structural MRI. The use of DW-MRI within a spatial normalization framework is complicated by the inherent high dimensionality of the data (diffusion models typically consist of more than a single intensity), as well as, the orientational nature of the data. This second issue requires an additional reorientation step that is not required when performing structural MRI registration. DTI-based spatial normalization [36, 88, 189, 191, 196] has been an active area of research and has shown to improve the alignment of WM structures over comparable structure based registration.

The DTI based approaches inherit, from the DT modeling, the difficulty in describing complex WM. Thus it could be expected that the use of more complex HARDI based diffusion models within the registration framework, would further improve the registration result. This chapter describes a spatial normalization framework that makes use of the FOD diffusion model but could be trivially expanded to utilize other RSH based diffusion models.

3.2. FOD-based Non-Linear Spatial Normalization

The goal of the proposed spatial normalization framework is to determine the spatial correspondence between two subjects by using the FOD image of each. This will enable the computation of an average FOD image suitable for parcellation or the computation of regional scalar measurements on each individual. A number of spatial normalization algorithms have been developed, in parallel to the one presented here, that make use of HARDI data models. These methods can be differentiated based on their treatment of orientational information.

The first group of algorithms use orientation invariant (OI) scalar measures to define image similarity measures, that are invariant to the orientation of the diffusion model. These image similarities are used to drive the registration framework to determine a spatial transformation relating the two images. Once the transformation is determined, it is applied to the subject image with a suitable reorientation strategy. OI representations and similarity measures that have been investigated and used for registration include the T2-weighted signal (b0) [85], the regional diffusivity and anistropy derived from each voxel's ADC profile [190]. A second group of methods utilize similarity measures defined on the models themselves and are implicitly sensitive to orientation; for instance, the L_2 norm of the RSH coefficients of the ODF [59] or the norm and the cross correlation of the FOD coefficients [135].

The algorithms which utilize OIs tend to be faster and less computationally complex, as they only perform a single reorientation step after the spatial transformation has been determined. In contrast, the orientation sensitive (OS) methods must incorporate reorientation into the optimization problem used to determine the optimal spatial transform and therefore presumably benefit from access to this additional information yielding a more accurate result. The proposed method seeks to utilize both OI and OS approaches into a single two-phase framework.

Diffeomorphic Demons FOD Registration

The registration framework is designed to incorporate valuable orientational information, while attempting to limit the computation cost of performing many reorientation operations, by utilizing a two-phase approach (Figure 3.1). In **Phase I** we compute orientation independent feature maps of both the moving (Subject) and fixed (template) FOD images. A multichannel Demons [176, 163] registration algorithm is then utilized to compute the deformation between these feature maps. Since these maps do not depend on orientation, there is no need to incorporate a reorientation step during the Phase I optimization. The resultant deformation field is then used to initiate the second registration phase. **Phase II**

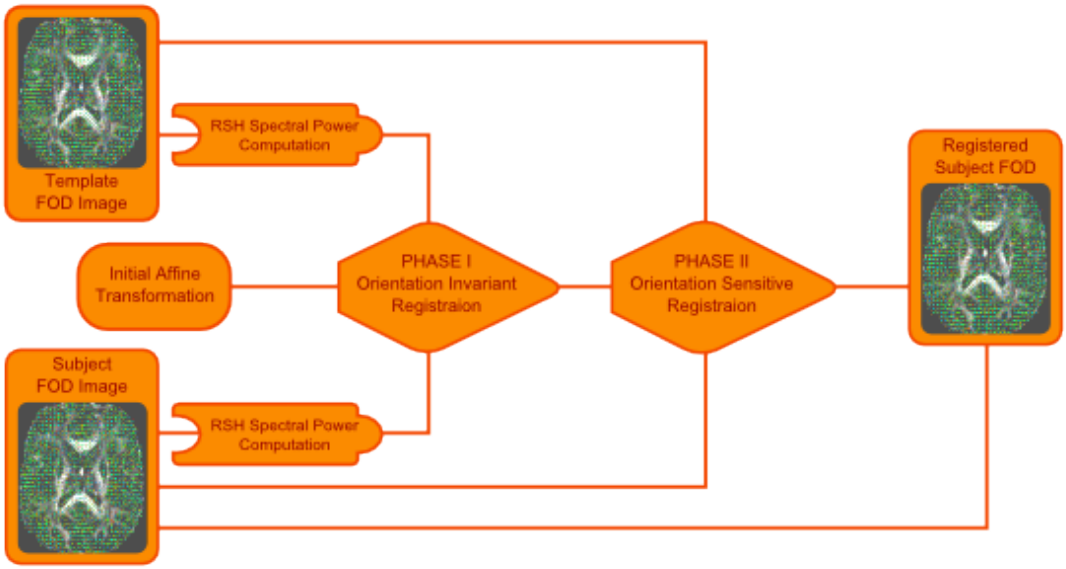

Figure 3.1: FOD registration is accomplished using a two phase registration scheme. First spectral power features are computed and registered. This registration is then improved during a second registration phase where the FODs are directly registered, while reorienting the FOD at each iteration.

utilizes a multichannel Demons registration framework to minimize the difference between the complete FOD images, represented by their RSH coefficients. This representation is dependent on the FOD orientation requiring the finite strain (FS) reorientation method (discussed below) to be used to reorient the FODs at each iteration of the registration process. The utilization of the two phase process reduces the computational complexity and convergence time, by removing the need to reorient the images in half of the iterations, without sacrificing the accuracy garnered from the inclusion of orientation information.

In phase I, both the fixed and moving images are represented by their RSH spectral power images (discussed in Section B.3) which are rotationally invariant. These images are comprised of feature vectors of the form $\mathbf{v}_l = \sum_m (\tilde{f}_{l,m})^2$, where $\tilde{f}$ are the RSH coefficients of the FOD at the particular voxel. The Diffeomorphic Demons framework minimizes the L_2 metric between the given images thus the phase I registration seeks to minimize the

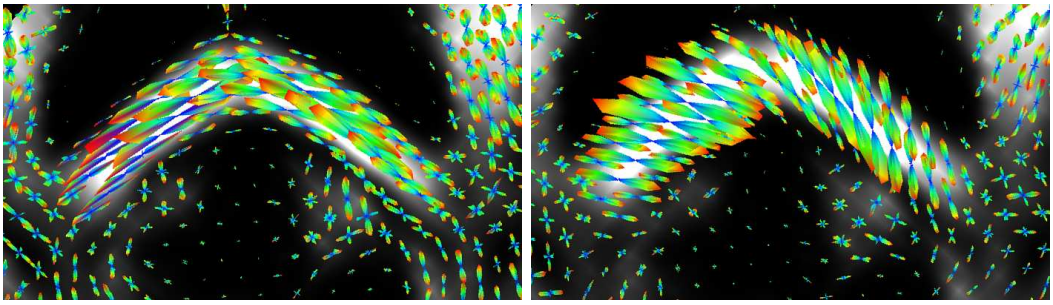

(a) (b)

Figure 3.2: Images of the posterior corpus callosum, with (a) and without (b) finite-strain reorientation of an FOD image following a 45 degree rotation. Note that without reorientation, the principal directions of the FODs do not coincide with the underlying anatomy.

following metric between the moving and fixed FOD images at each voxel,

$$\sqrt{\sum_{l=0,l\ \text{even}}^{l\text{Max}} (\sum(\tilde{f}_{l,m})^2 - \sum(\tilde{g}_{l,m})^2)}$$

where $\tilde{f}$ and $\tilde{g}$ are the RSH coefficients of corresponding voxels in F and M.

Phase II uses the full vector of RSH coefficients to represent the FOD at each voxel, minimizing the L_2 metric in the full RSH space,

$$\sqrt{\sum_{l=0,l\ \text{even}}^{\text{lMax}} \sum_{m=-l}^{l} (\tilde{f}_{l,m} - \tilde{g}_{l,m})^2} = \int d\omega f(\theta,\phi) - g(\theta,\phi) \tag{3.1}$$

This metric measures the total amplitude difference between the two spherical functions, f and g, and is inherently sensitive to the orientations of both. Owing to this sensitivity, during the Demons optimization process, we reorient the moving image, using the finite strain reorientation scheme [4], when applying the transformation at the current iteration.

Finite Strain FOD Reorientation

Based on the work that has been done within the DTI community [4, 188], we utilize the finite strain (FS) algorithm [4] to estimate the rotational component (R) of the transform based on its Jacobian at a particular location. The FS algorithm was chosen due to its

computational simplicity, as well as, its unbiased treatment of the maxima of the data model. Thus at each voxel, the FOD (f) is replaced by $f' = f \circ R^{-1}$. In the RSH representation, this takes on the form of $\tilde{f}' = \widetilde{R^{-1}}\tilde{f}$, where $\widetilde{R^{-1}}$ is the matrix representation of R^{-1} in the RSH space, the details of which are discussed in Appendix B.2. The effect and need for performing reorientation can be seen in Figure 3.2.

Multichannel Diffeomorphic Demons

The multichannel diffeomorphic Demons algorithm forms the central mechanism that drives both phases of our registration method. It seeks to determine a correction to the current spatial transformation, s, of the form $exp(u)$. This update minimizes a global energy functional defined in terms of the fixed and moving image, F and M,

$$E_s(u) = \sum_{p \in \Omega} ||F(p) - M \circ s \circ exp(u(p))||^2_{L2} + \left(\frac{\sigma_i}{\sigma_x}\right)^2 ||u||^2$$

where p are points in Ω, the domain of the fixed image, F. While the $\frac{\sigma_i}{\sigma_x}$ term accounts for image noise and interpolation error and acts, as can be seen from equation 3.2, as a regularizer for determining the update field. We can linearize the image similarity term in the region of $u = 0$ as:

$$F(p) - M \circ s \circ exp(u(p)) = F(p) - M \circ s(p) + J_p u$$

In the case where F and M are images of vectors, J_p is the Jacobian matrix. With the above linearization, the energy functional simplifies to

$$E_s(u) = \sum_{p \in \Omega} \left|\left| \begin{bmatrix} F(p) - M \circ s(p) \\ 0 \end{bmatrix} + \begin{bmatrix} J_p \\ \frac{\sigma_i}{\sigma_x} I \end{bmatrix} u(p) \right|\right|^2_{L2}$$

If we make the assumption that the voxels are independent, which is not strictly true when performing reorientations, the optimization of $E_s(u)$ can be broken up in to individual

equations for each point p.

$$\begin{bmatrix} F(p) - M \circ s(p) \\ 0 \end{bmatrix} + \begin{bmatrix} J_p \\ \frac{\sigma_i}{\sigma_x} I \end{bmatrix} u(p) = 0$$

which simplifies to

$$(J_p^t J_p + \frac{\sigma_i}{\sigma_x} I) u(p) = -J_p^t (F(p) - M \circ s(p))$$

yielding following update step

$$u(p) = -(J_p^t J_p + \frac{\sigma_i}{\sigma_x} I)^{-1} J_p^t (F(p) - M \circ s(p)) \tag{3.2}$$

In our application, we have chosen to use the symmetric computation of the Jacobian, $J_p = -\frac{J_p(F) + J_p(M \circ s)}{2}$, where $J_p(F)$ and $J_p(M \circ s)$ are the Jacobians of the fixed and deformed moving images at the point p.

Each iteration of the multichannel diffeomorphic Demons method can be summarized as follows

1. compute an update step u using equation 3.2
2. smooth u with a Gaussian filter
3. $s \leftarrow s \circ u$
4. deform the moving image using s
5. apply reorientation if using OS features (Phase II)

This process is repeated either until the update steps no longer substantially reduce the image difference or for a prescribed number of steps.

In summary, our method consists of two applications of the multichannel Demons algorithm. In the first phase, it is applied to align the orientation invariant RSH power spectrum images

computed from the fixed and moving images. The resultant transformation is then used as the initial transformation for the second phase, which uses the entire RSH representation of the FOD images and necessitates a reorientation at each iteration.

3.3. Validation: Simulated Experiments

The proposed method was validated by comparing it to each of its constituent registration processes (Phase 1 and Phase 2) as well as to a scalar Demons algorithm that utilizes the non-diffusion weighted (T2 weighted) images from the DW-MRI datasets to drive the registration. These four methods (Phase 1, Phase 2, Combined, T2) were applied to a simulated dataset to evaluate their ability in registering prominent WM structures.

Simulated Datasets

A DW-MRI dataset was acquired on a healthy human using a Siemens (Siemens Medical Systems, Iselin, NJ) Verio 3T scanner and a spin-echo, echo-planar imaging sequence, TE = $106ms$, TR = $16.9s$, $2mm$ isotropic voxels, $b = 3000\,\mathrm{s/\,mm^2}$ and 128 gradient directions with 4 images, with no diffusion weighting (b0). An FOD image, of order 12 (91 components), was computed using the CSD method. This would serve as the template image. A T1 structural image was also acquired. Prominent WM regions of interest (corpus callosum, corona radiata, internal capsule) were determined by registering the template T1 image with the Eve atlas [124]. A WM mask was created using the FSL's FAST algorithm [198].

The template b0 image was registered, using a scalar Demons algorithm, to the b0 image of 10 subjects, yielding 10 deformation fields from the subject space into the template space. The 10 deformation fields were then applied to the template FOD image using the finite strain reorientation strategy. This process yielded 10 simulated *subject* datasets along with deformation fields describing the transformation from the subject space to the template space.

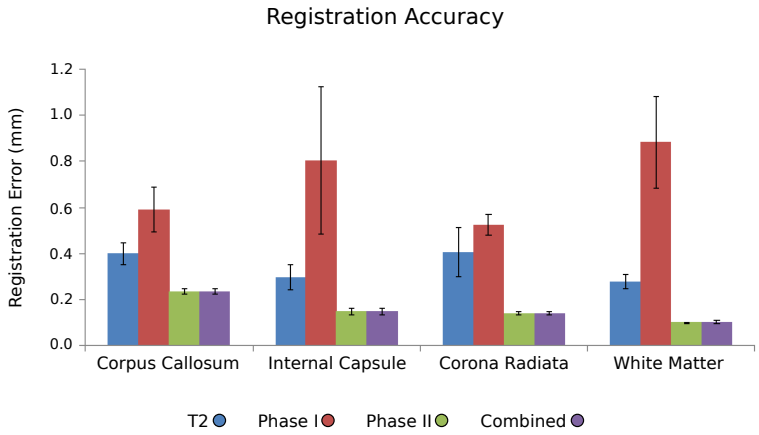

Figure 3.3: Average displacement error is shown for prominent white matter regions (Corpus Callosum, Internal Capsule, Corona Radiata) and whole brain white matter, for each of the registration methods.

Results

The four registration algorithms (Phase 1, Phase 2, Combined and T2) were then performed on these 10 datasets. The resultant deformations were subtracted from the known deformations yielding a displacement error vector at every voxel. The magnitude of the displacement error vectors were then averaged within the ROIs and across subjects.

All methods were robust and produced reliable results for all simulated datasets. Figure 3.3 shows the average displacement error within the ROIs and in the whole brain WM. There are three things to note from Figure 3.3. First, the inclusion of orientational information (Phase 2 and Combined) improves the registration accuracy compared with the other methods. Second, there is no significant difference between results of the Phase 2 method and the combined method. Finally, the decrease in accuracy when using the Phase 1 method as compared to the T2 method is surprising, although it may be attributed to the fact that the T2 method was used to initially create the simulated datasets.

The primary computational cost of including orientational information in the similarity measure, is the need to perform a reorientation operation at each iteration of the Demons

Figure 3.4: A: Average registration error for the internal capsule as a function of the RSH order of the FOD fit. B: Computation time for each registration as a ratio to the T2 registration method.

algorithm. As discussed in Section B.2, reorientation is a linear operation in the RSH space, and as the dimension of this space, determined by the order of the RSH fit, increases the complexity of determining the reorientation operator also increases. Figure 3.4 shows the average registration error for the internal capsule for the Phase 2 and combined registration methods, as well as the computation time relative to the T2 registration method. The internal capsule was chosen for its small size and thus its susceptibility to registration errors. Even at the lowest order tested ($l = 4$), we see that both the Phase 2 (0.162mm error) and the combined (0.165 mm error) registration methods out perform the T2 (0.29 mm) and Phase 1 methods (0.8 mm). As the fit order is increased we see a growing separation in computational time between the Phase 2 and combined methods while we see no difference in accuracy improvement between the two. This suggests that it isn't until the higher order fits ($l > 4$) are being used that the befits of the combined approach be come significant.

3.4. Validation: *In-vivo* Experiments

In order to evaluate the utility of the proposed FOD registration algorithm within DW-MRI population studies, it was compared with state of the art DTI based registration techniques in a population of typically developing adolescents. Within the same scanning session, optimized HARDI ($b = 3000\,\mathrm{s/mm^2}$) and DTI ($b = 1000\,\mathrm{s/mm^2}$) datasets were acquired on each subject. Once corrected for imaging artifacts and motion, these different

DW-MRI modalities offer different representations of the same anatomy. Thus, the *best* spatial normalization should correctly align both images. The registration algorithms are evaluated based on the their ability to adequately register the DTI, FOD and WM images of the population.

The subjects used for the experiment were the 27 typically developing controls acquired as part of the ASD dataset. A description of this imaging dataset can be found in Section A.1.1. Both the HARDI and DTI datasets were corrected for Rician noise and eddy current artifact. FOD and DTI images were then fit to their respective datasets. A WM image was determined using tissue segmentation performed on each subject's structural MP-RAGE image. All three images were then aligned to the FOD image, resulting in co-registered FOD, DTI and WM images for each subject. The details of these procedures can be found in Section A.2.

Registration Results

For each subject, three spatial transformations are computed, registering their anatomy to that of a 10 year old male chosen to act as a template subject. This process begins with both the FOD and DTI images of each subject being linearly registered to the template space via an affine transformation, computed using the subject's b0 image. These linearly registered images serve as the starting point for the three registration procedures.

First, the subject's FOD image is registered to that of the template subject using the proposed non-linear registration process, referred to as FOD-Demons. The DTI image of each subject is then registered into the template space using the DTI-Droid registration algorithm [88] as well as a DTI based version of the Demon's method presented in Section 3.2, referred to as DTI-Demons. Phase I of the DTI-Demons method uses FA as the rotationally invariant DT feature, while Phase II uses the log-Euclidean [11] representation of the DTs and a finite strain reorientation strategy.

At the culmination of this process, there are three non-linear transformations (FOD-Demons, DTI-Droid and DTI-Demons) relating the anatomy of each subject to the anatomy of the

template subject. These deformations are then applied to both the FOD and DTI images of each subject, generating registered images. Residual images, consisting of the voxel-wise difference between the subject's registered image and the template, are also computed, for each registration method and for each modality. The RSH L_2 distance (equation B.5) was used to measure the voxel-wise difference of the FOD images while the Log-Euclidean metric [11] was used for the DTI images.

In addition to computing residual images, population variance images were computed for both the FOD and DTI contrasts, for all three registrations, using equation 3.3 at each voxel x, where $f_i(x)$ is the model of interest and n is the number of subjects in the population. Again when computing the DTI variance the Log-Euclidean metric was used as the distance measure ($d(.,.)$), while the L_2 RSH distance (equation B.5) was used when computing the FOD variance.

$$V(x) = \frac{1}{n}\sum_{i}^{n} d(f_i(x), \mu)^2 \tag{3.3}$$

Figure 3.5 shows representative slices of the population variance FOD and DTI images computed using each of the three registration techniques. When examining Figure 3.5 it is important to recognize that the FOD and DTI variances are scaled differently since they are computed from inherently different modalities. However, the same scaling is used across the registration types (rows of Figure 3.5).

There are a number of conclusions that can be drawn from this figure. Firstly, the highest variances, in both modalities and across all registration techniques, occurs in the splenium of the CC. This is likely caused by that region's proximity to the ventricles, coupled with the highly curved structure of the CC in that region. Secondly, all three transformations perform similarly when the DTI variance is used to compare them, suggesting that the contrast provided by the FOD modeling is sufficient to align the DTI images. However, this is not the case when using the FOD variance images as a point of comparison. There are clear areas, highlighted in green in Figure 3.5, showing increased variance as measured by the FOD images, when registered by the DTI based registration techniques, than is

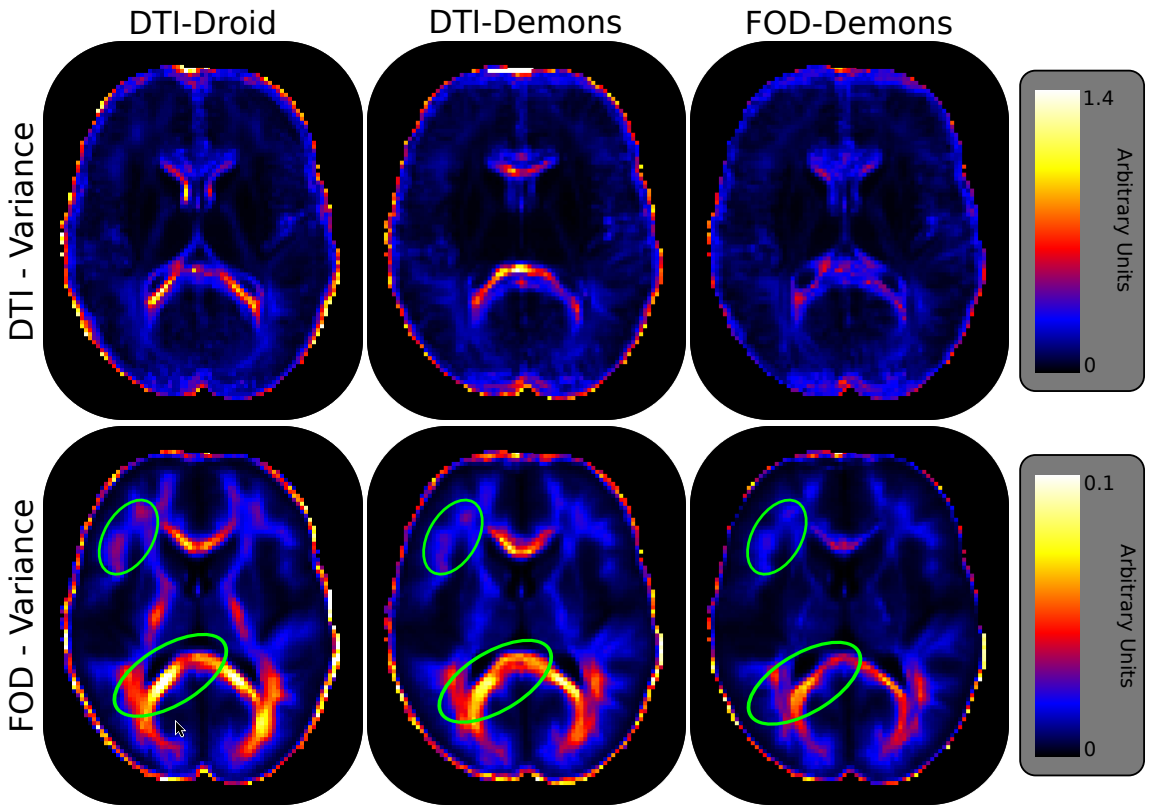

Figure 3.5: Representative slices of the FOD and DTI population variance images computed for each registration method, DTI-Droid, DTI-Demons and FOD-Demons. Each row is scaled independently since different difference metrics, the Log-Euclidean for DTI and equation B.5 for FOD, are used within equation 3.3 to compute the respective variances. The FOD-Demons registration method is able to minimize both the DTI variance as well as the FOD variance suggesting that it better captures the true anatomical differences between subjects better.

observed using the FOD based technique.

To better quantify these differences, the residuals were submitted to t-tests seeking to identify regions where residuals computed using the proposed FOD-Demons registration technique were lower than those computed using the DTI based methods. Representative slices from these statistical maps are shown in Figure 3.6, thresholded at an FDR (False Discovery Rate) [60] corrected p-score of 0.001. From this, it is clear that the FOD-based registration produces significantly lower residuals than either DTI-based techniques when the FOD residual is used, while performing similarly when compared using the DTI residual.

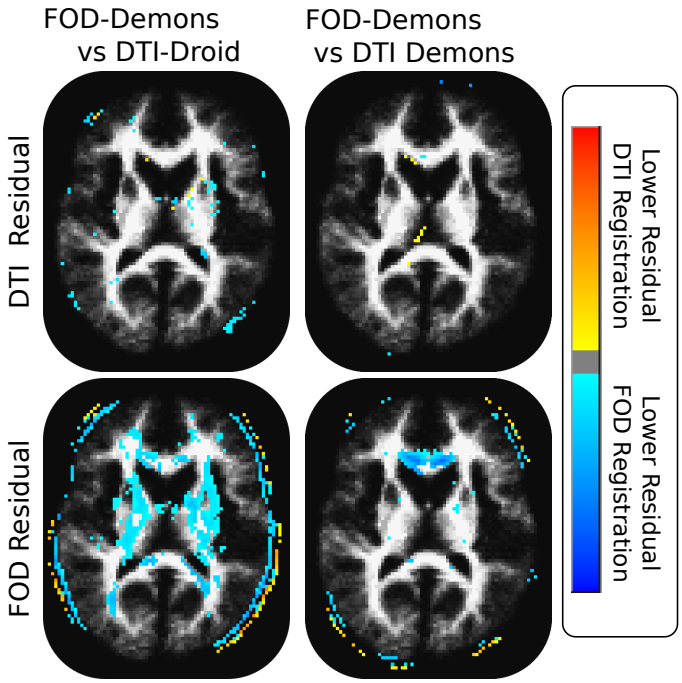

Figure 3.6: Statistical maps determined by four t-tests, performed to identify regions where the registration methods yield different FOD and DTI residuals. Representative slices, thresholded at an FDR correct p-score of 0.001, are shown. The FOD based registration performs significantly better, i.e. yields lower residuals, than either DTI-based technique when the FOD residual is used, while performing similarly when compared on the DTI residual.

A final point of comparison is the ability to register WM volumes of the population. Figure 3.7 shows the population averaged WM masks created by transforming each subject's WM mask, using each of the three registration techniques. The values of this image at each voxel are the proportion of the subjects where that voxel is considered WM. Thus, higher values signify a greater overlap of the population's WM masks, indicative of superior registration accuracy in these regions. The WM mask of the template subject is shown as a comparison. Again the similarity between the two DTI based registration techniques is clear, as is the improvement, evident in the higher values in the cortical WM regions, achieved using the registration technique based on the FOD contrast.

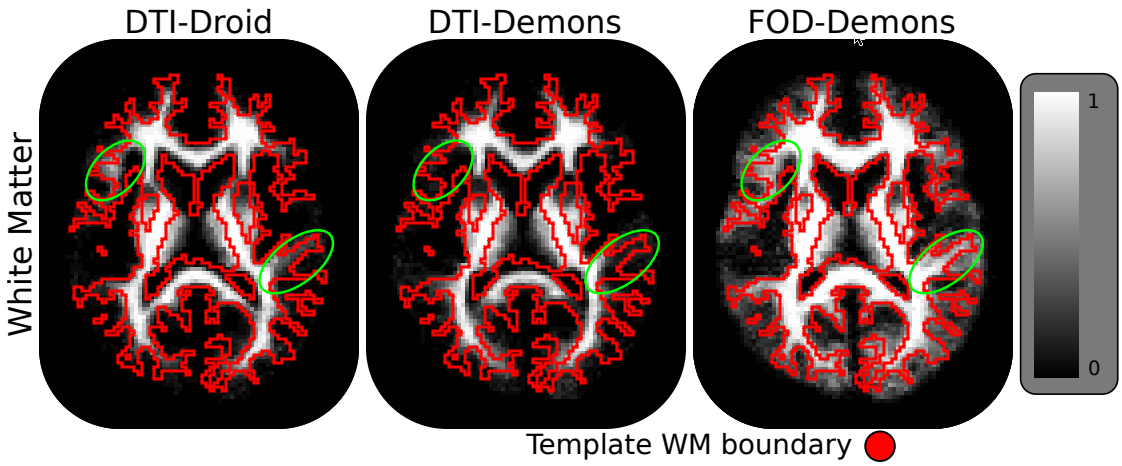

Figure 3.7: Representative slices of WM masks averaged over the population for each of the registration methods overlaid with the template WM mask (red contour). Higher values in these maps signify a higher degree of overlap in the registered WM masks of the population. Areas where the FOD-Demons registration results in improved alignment of cortical WM structures are indicated in green.

3.5. Conclusions

The general aim of performing spatial normalization, within neuroimaging, is to capture the spatial relationship between the neuroanatomy of different subjects. Once this information is captured, it can be exploited to either study the geometric (volumetric) differences between the anatomy of individual subjects [13, 14, 45], or to study the population within a *standard* reference frame using other modalities, such as fMRI or DW-MRI. The work contained in this thesis focuses primarily on examining group differences in regional WM architecture, as represented by diffusion models. Thus we are principally concerned with establishing a correspondence at the voxel level between the WM anatomy of different subjects. This necessitates the use of registration techniques that utilized modalities sensitive to differences in WM anatomy, namely those derived from DW-MRI.

In this chapter, we presented one such method which utilizes the FOD HARDI diffusion model to drive the registration. It should be noted that the formulation of the method does not explicitly depend on the FOD model and could therefore be applied to any diffusion

model representable in the RSH basis. The method presented is a two phase diffeomorphic Demons based framework, using an orientation invariant approach in the initial phase followed by an orientation sensitive secondary phase. Simulation studies show that this overall approach is able to maintain the registration accuracy achieved from the more intensive orientation sensitive method, in reduced computational time (Figures 3.3 and 3.4).

Additionally, the proposed method was compared with the DTI-Droid based registration algorithm as well as a DTI version of the proposed algorithm (DTI-Demons), in a population of 27 typically developing children. An analysis of both the FOD and DTI population variances (Figure 3.5) computed by these techniques indicate that the proposed FOD method is better able to align the anatomy of these subjects, since it better minimizes both forms of variance, while increasing the overlap of cortical WM (Figure 3.7). The FOD-Demons technique is able to significantly ($p < 0.001$) reduce the population residuals (Figure 3.6) of the FOD images, when compared to either of the DTI based techniques. However, all the methods were able to adequately reduce the DTI residuals, indicating that by considering the additional information content, available from the FOD modeling, the proposed method is able to better capture the geometric differences in the population.

Although the endpoints of many population studies are not directly related to spatial normalization, it is none the less of critical importance to their success. As DW-MRI methods continue to advance, the need for population analysis methodologies, and therefore registration methods, that take full advantage of this additional information will grow. The proposed method is one of the first such methods, that utilizes the FOD diffusion model to perform image registration and serves as a foundation for much of the work that follows.

CHAPTER 4 : White Matter Parcellation

4.1. Introduction

The use of brain atlases in neuroimaging studies allows researchers to register, identify and perform measurements on individual subjects within a common spatial coordinate system enabling large scale group studies. Such studies leverage their greater statistical power to elucidate smaller or more subtle anatomical differences that exist in specific diseases. Since the introduction of the Talairach [162] human cortical atlas, a number of MRI atlases have been introduced to assist with these measurement issues. T1-weighted MRI atlases [12, 39, 98, 97, 111, 112] have been used extensively to illustrate differences in gray matter anatomy as well as to localize functional signals within these structures. While T1-weighted MRI provides detailed information concerning cortical anatomy, it provides considerably less information concerning white matter anatomy [165], thus these atlases have focused primarily on the identification of GM regions and possess limited detail concerning WM regions.

By providing an *in-vivo* WM contrast mechanism, DW-MRI has reinvigorated the study of WM pathologies. More recently, DTI-based anatomical atlases [119, 124, 178] have been introduced to address the relative lack of information provided by the existing cortical atlases. While DTI is able to model WM regions possessing a single fiber population, it is ill-suited to model areas of more complex WM, such as fiber crossing. This limitation makes delineating boundaries within these regions difficult and the labeling within them suspect. HARDI data models, such as the FOD, provide contrast in areas of fiber crossing and orientation change that is unavailable from conventional DTI and better reflects the underlying structure of the WM tissue.

This chapter proposes a novel methodology for building WM atlases by utilizing the contrast within a population average HARDI image to identify and automatically label regions of homogenous WM. The utilization of an automated data driven clustering algorithm for

region labeling, permits the generation of population/study specific atlases without the need for manual delineation of anatomical regions.

In general, atlases identify spatial regions consisting of voxels that meet some conceptual criterion of *sameness*. The majority of imaging atlases attempt to label regions based on named neuroanatomical constructs, such as the prefrontal cortex or the internal capsule. This typically requires a neuroanatomist/neuroradiologist to manually label a template image to identify each region. A process that is inherently variable, due to the underlying variability of human neuroanatomical boundaries, resulting in different labellings by different neuroanatomists [46, 180]. Recent work within the registration community [74, 79, 80, 196] suggests that choosing a registration template from the population under study, improves the accuracy of spatial normalization. However the labor intensive labeling process makes the accurate transfer of atlas defined regions to a population specific atlas difficult, a particularly acute issue when the population has unique characteristics (such as being of a younger age than the anatomical atlas) or when the new imaging modalities, such as HARDI, are being used.

Another important consideration, is whether labeling based on anatomical boundaries provide sufficient demarcation, particularly in areas of complex WM, for applications such as ROI based WM statistical analysis. For instance, most large fiber bundles such as the CC or SLF, sensible targets for anatomical ROI labeling, are known to traverse a variety of WM architectures and thus may not be well suited for ROI studies where they are represented by a single average diffusion model or a single scalar feature derived from the entire region.

To address the limitations of existing WM atlases, we propose the use of an automated data driven clustering routine to generate a population-specific HARDI atlas. A population averaged FOD image is generated by spatially normalizing each subject to a template subject, using the method described in Chapter 3, and then averaging the FOD images. The clustering routine is then applied to create a large number of spatial regions, each consisting of homogeneous WM architecture, as measured by the FOD image. As regional

homogeneity is the driving force behind the clustering process, each region can be confidently represented by its average. This makes these regions ideal for ROI statistical studies or for the extraction of spatial WM features for use in a classification framework.

While neuroanatomical labeling may not provide suitable delineation of boundaries needed to identify homogeneous WM regions, it does aid in interpretability by providing researchers and clinicians with a means of investigating the structure and function of these regions and providing a comparative basis to other published studies. To improve the interpretability of our regions, we assign each homogeneous WM region with neuroanatomical labels based on its spatial overlap with an existing WM atlas. While not designed merely to identify these named anatomical constructs, the neuroanatomical relabeling of the data-based atlas, allows for describing the ROI as belonging to the anatomical region, thereby instilling it with joint information of the underlying fiber orientation as well as the global anatomy and function, thereby facilitating interpretability.

We demonstrate the application of our framework by generating an atlas from a dataset consisting of typically developing pediatric and young adolescent subjects, although the method is generalizable to any population under study. By comparing regional FOD spatial variances in anatomical labels to the variances computed from the regions determined by our clustering method, we demonstrate the ability of our algorithms to generate atlases consisting of homogeneous WM regions well beyond what is achievable using the neuroanatomical labeling available in existing WM atlases. Average measures in these homogenous regions can then be used for subsequent statistical analysis and as the basis for between group and longitudinal within-group investigations. Anatomical interpretability of these study specific atlases generated by our method is imparted by establishing a correspondence with an existing atlas such as the EVE-DTI [124] atlas in the presented case. Which could in principle, be replaced by any anatomical atlas deemed of importance by the hypotheses of the study for which the atlas is being created.

Algorithm 1 Spatially Coherent Normalized Cuts

Require: Initial ROIS: C
Require: N-CUTS parameters: σ_f, σ_s
Require: Stopping criteria: ϵ
Ensure: Final ROIS: C'
  $C' \leftarrow C$
  while $max_{R \in C'} \Phi(R) > \epsilon$ **do**
    Identify the region, C_i, with the maximal degree of non-uniformity.
    Remove C_i from collection C'.
    Partition C_i using normalized cuts into $C_{i,1}$ and $C_{i,2}$.
    Extract all the spatially connected regions from both $C_{i,1}$ and $C_{i,2}$.
    Add new spatially connected regions to collection C'.
  end while

4.2. White Matter Parcellation

WM regions, that are defined anatomically either based on fiber bundles such as the SLF or the CST, or based on their spatial location such as the internal capsule (IC) or the sagittal stratum (SS) often extend through a range of diverse WM architectures (orientations, crossings etc). This heterogeneity is problematic, particularly when using robust WM features such as the DT or the FOD diffusion models in subsequent analysis, as it makes the representation of these ROIs, by their averages, suspect. These anatomical ROIs are intended to represent anatomical structures and are therefore often not uniform in the feature space of interest. This non-uniformity is the main trait we would like to avoid when defining regions.

To address this, we utilized an approach similar to that of the superpixel [117] methodology. Within this framework, a single WM region or a set of anatomically or otherwise defined regions are iteratively divided into spatially connected subregions, using a normalized-cut clustering routine and a seed growing algorithm to enforce spatial connectedness.

Spatially Coherent Normalized Cuts for WM Clustering

The proposed method takes an FOD image, either a population average or that of a single subject, and a collection of initial regions and partitions these ROIs into spatially connected regions based on the similarity between the FODs making up the output regions. The input

ROIs are supplied as a labeled image, with each label specifying a unique ROI.

The initial step of the algorithm is to parse the supplied labeled image into a collection of fully connected regions. Any region that contains more than one spatially connected component, is divided into those components. This process yields a collection, C, of fully spatially connected regions derived from the supplied labeled image. From C, we identify the region which is most heterogeneous with respect to the FODs it contains. A region's heterogeneity is represented by the average squared distance (equation 4.1) between the mean FOD (μ) and the FOD (f_i) of every voxel in the region. This measure has an interpretation similar to a variance.

$$\Phi(R) = \frac{1}{n} \sum_{i \in R} d(f_i, \mu)^2 \tag{4.1}$$

For the purposes of clustering we utilize the L_2 metric on the RSH coefficients of the normalized FODs, equation B.6, to measure the distance between pairs of FODs ($d(\cdot)$).

Once the region with the highest non-uniformity ($\Phi(R)$) is determined, it is partitioned in two using the normalized cuts (N-Cut) algorithm, discussed below. This process is mediated by the chosen form of the similarity function (equation 4.2). We make the canonical choice of a Gaussian kernel over the FOD domain, with standard deviation σ_f and another Gaussian kernel (standard deviation σ_s) over the spatial locations, to describe the similarity between two WM voxels. The N-Cuts algorithm has no explicit criteria for enforcing spatial connectedness. Therefore the two resultant clusters are further partitioned into spatially connected subcomponents using the seed growing algorithm, also described below. Thus at each iteration, the region with the highest non-uniformity is replaced by a number of spatially compact subregions. This process is repeated until every region is below a predefined non-uniformity threshold ϵ, or until the number of clusters exceed a user defined value. Finally these regions are used to generate an output label map.

Normalized Cuts

The normalized cuts (N-Cut) algorithm [136, 149] is a means of partitioning a set of data points x, in our case a set of WM voxels, based on a predefined similarity measure $k(.,.)$. Using the similarity measure, we build an affinity matrix such that $K_{i,j} = k(x_i, x_j)$. The affinity matrix describes the weights of a fully connected undirected graph using elements of x as the nodes. The N-cut algorithm labels each node, dividing the vertices into 2 sets A and B. The cost $Cut(A, B)$ is the sum of all connections between elements of A and elements of B. The goal is to find the labeling that minimizes the normalized cut, $Cut(A, B)\left(\frac{1}{Vol(A)} + \frac{1}{Vol(B)}\right)$ where $Vol()$ is the sum of the weights within a set.

The labeling is found via a relaxation to the above problem by finding the second largest eigenvector, $\mathbf{v}$, of the matrix $\mathbf{D}^{-\frac{1}{2}}\mathbf{K}\mathbf{D}^{-\frac{1}{2}}$, where $\mathbf{D}$ is a diagonal matrix whose iith element is the sum of all elements in the ith row of $\mathbf{K}$. The labels are determined by examining the sign of $\mathbf{v}$. For a complete description please see [136, 149].

Our application of the N-Cut algorithm, concerns the ability to label WM voxels based on their FOD. As discussed above, we use a Gaussian kernel with standard deviation of σ_f as the basis of our similarity measure. When working without initial anatomic regions our datasets can be on the order of 80,000 elements making storage of the $\mathbf{K}$ matrix infeasible. In order to increase the sparsity of $\mathbf{K}$, we can optionally include a second Gaussian kernel sensitive to the spatial locations of the voxels, yielding the following similarity measure:

$$k(x_i, x_j) = \begin{cases} e^{\frac{-d(f_i,f_j)^2}{2\sigma_f^2}} & \sigma_s = 0 \\ e^{\frac{-d(f_i,f_j)^2}{2\sigma_f^2}} e^{\frac{-\left|\left|p_i - p_j\right|\right|^2}{2\sigma_s^2}} & \sigma_s > 0 \end{cases} \tag{4.2}$$

where x_i and x_j are WM voxels with f_i, f_j, p_i, and p_j being the corresponding FODs and spatial locations and $d(\cdot)$ being the L_2 metric on the RSH coefficients of the normalized FODs, equation B.6.

Given a collection of WM voxels, we compute the affinity matrix, $\mathbf{K}$, using the above

Algorithm 2 Seed growing algorithm to extract spatially connected components

Require: List of voxels X
Ensure: List of labels L
  labelValue = 1
  labelMembers = $\emptyset$
  for all $x \in X$ **do**
    if x is not labeled **then**
      add x to labelMembers
      repeat
        y = next element of labelMembers
        $L[y]$ = labelValue
        add all unlabeled neighbors to labelMembers
      until all members of labelMembers have been visited
      labelValue = labelValue+1
      labelMembers = $\emptyset$
    end if
  end for

similarity function. To further increase sparsity any elements of $\mathbf{K}$, that are less than 10^{-2} are set explicitly to 0. We then compute the matrix $\mathbf{D}$ and determine the second largest eigenvector, $\mathbf{v}$, of $\mathbf{D}^{-\frac{1}{2}}\mathbf{K}\mathbf{D}^{-\frac{1}{2}}$ using the SLEPc [81] software package. Two new regions are determined based on the sign of $\mathbf{v}$.

Connected Component Extraction

In order to extract all spatially connected subcomponents of a region, we use a simple seed growing algorithm. A supplied region consists of a set of voxels, that are initially unlabeled. These voxels are then labeled using the seed growing algorithm described in algorithm 2. Each unique label is then used to create a new spatially connected region.

Anatomical Labeling

It is advantageous, for instance when interpreting the location of abnormalities, to know the anatomical label of a specific region. This requires the additional step of labeling each of these data-defined ROIs with anatomical labels, provided by a co-registered anatomical atlas. We accomplish this by using an existing WM anatomical atlas, for instance the ICBM-DTI-81 [119] or EVE-DTI [124] atlases, to provide anatomical labels to each of the homogeneous WM regions that are determined. This is accomplished by using non-linear

registration to spatially normalize the atlas structural image to the population average structural image. The percent overlap between each WM region and the existing anatomical atlas regions are computed. For each WM region any anatomical label with greater than a 10% overlap is assigned to that WM region, allowing for the possibility of multiple anatomical labels being assigned to regions that span the boundaries of anatomically defined regions.

The final result of the entire parcellation algorithm is a hierarchical two level WM atlas. Each WM voxel is first assigned a label representing the data driven ROI to which it belongs. Secondly, each of these ROIs is assigned a combination of anatomical labels based on the regional overlap to an existing anatomical atlas. The finer data driven ROIs are designed to consist of homogenous WM, as measured by a low FOD variance (equation 4.1) and may be useful for statistical analysis or to extract regional features to comprehensively represent a subjects WM architecture. The anatomical labels provide a more global anatomical context to each ROI allowing both the location and in some cases function of each ROI to be ascertained and communicated to other researchers.

4.3. Validation: Simulated Experiments

Simulated Fiber Cross

A 64 direction, $b = 3000\,\mathrm{s/mm^2}$, DW-MRI dataset, with Rician noise ($\sigma = 0.05$), was simulated using the Numeric Fibre Generator (NFG) [37]. A fiber crossing between a straight and curved fiber bundle was modeled. Each bundle was segmented into smaller fibers, each modeled as a diffusion tensor with fractional anisotropy of 0.8 and mean diffusivity of $0.0009\,\mathrm{mm^2/s}$. FODs were computed using constrained spherical deconvolution [166] to estimate an order 8 FOD at each voxel and the parcellation method was applied using the following parameters, $\sigma_f = 0.3$, $\sigma_s = 0$ and $\epsilon = 0.1$. Other parameter sets were used but with negligible difference.

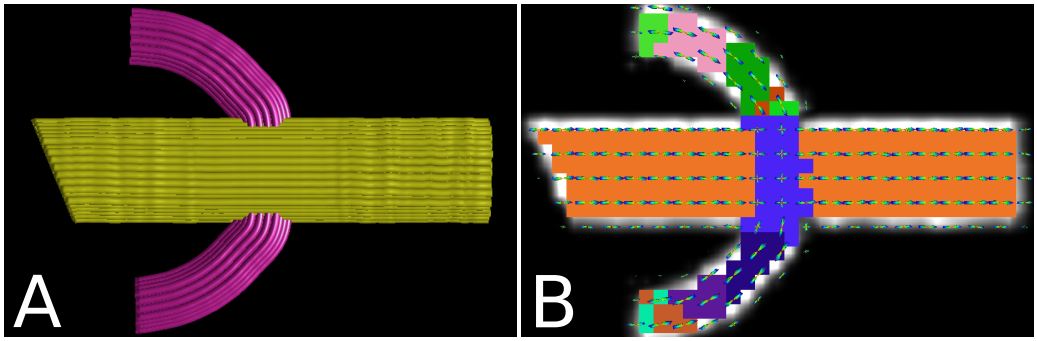

Figure 4.1: A) Simulated crossing fiber bundles generated by Numeric Fiber Generator [37], B) WM parcellation with variance below $\epsilon = 0.1$, generated via the proposed method using a Gaussian kernel ($\sigma_f = 0.3$) to measure FOD similarity. The area containing the fiber crossing is clearly distinguished, as are regions with similar orientations.

Results

The regions determined by the method can be seen in Figure 4.1. A single ROI was determined for the fiber crossing region as well for the remaining portions of the horizontal fiber bundle. The curved fiber bundle is separated into a number of regions containing similarly oriented FODs. For each of these ROIs, we would have confidence that the average FOD is a good representation of the region's WM architecture. Contrast this with anatomical ROIs defined by the actual fiber bundles. Since both bundles pass through the crossing region, the FODs of the cross would contaminate the averages of both bundles. More problematically, the FODs being averaged for the curved fiber bundle have a wide range of orientations obfuscating any directional information. These factors would cause neither fiber bundle to be well represented by its average.

4.4. Development of a Adolescent WM Atlas

The problem of atlas generation or ROI delineation occurs in any population study where regional imaging measures serve as the basis of group comparison, such as ROI statistical analysis or subject based classification. The problem is most acute when new imaging modalities, such as HARDI, are being utilized (for which no anatomical atlases exist) or when the population under study has not been used for generating atlases previously (such

as in a younger population). For this reason, we illustrate the application of our WM parcellation technique by creating a population atlas from a dataset of typically developing adolescent and pre-adolescent healthy subjects (6 – 18 years). This specific population is of interest to many WM researchers involved in studies of younger populations, at varying developmental stages, specifically those studying autism spectrum disorder and schizophrenia, which are believed to effect WM architecture and development [96, 177]. This is an illustrative atlas to demonstrate the methodology. The intended usage of the framework is the generation of study specific atlas which may need to be regenerated with a larger sample size, or to suit specific clinical purposes.

Forming the Population Averaged FOD Image

The dataset consisted of 23 typically developing children (TDC) between the ages of 6 and 18 years (mean 11.2 $\pm$ 2.7 years) chosen from the ASD control population (Section A.1.1). FOD images were computed following eddy current and Rician noise reduction. A co-registered WM mask was also computed via tissue segmentation of the subject's structural image. Please see Section A.2 for a description of these procedures.

The FOD image of each subject was then non-linearly registered, via the method described in Chapter 3, to that of a 10 year old male, who was chosen to serve as the template subject. Once this process was completed for each of the 23 subjects, a population average FOD image was computed by averaging each RSH component of the registered subject FOD images individually. Using the computed deformation fields, each subject's WM segmentation mask was deformed into the template coordinate frame and then averaged and thresholded to yield a binary WM mask describing the voxels that were considered WM in over 40% of the subjects. These 2 images, the population average FOD image and the population WM mask are then used to determine the atlas regions.

Region Delineation

The key aspect of the atlas generation framework is the method, described in Section 4.2, used to delineate regions of spatially homogeneous WM. Our automated WM parcellation

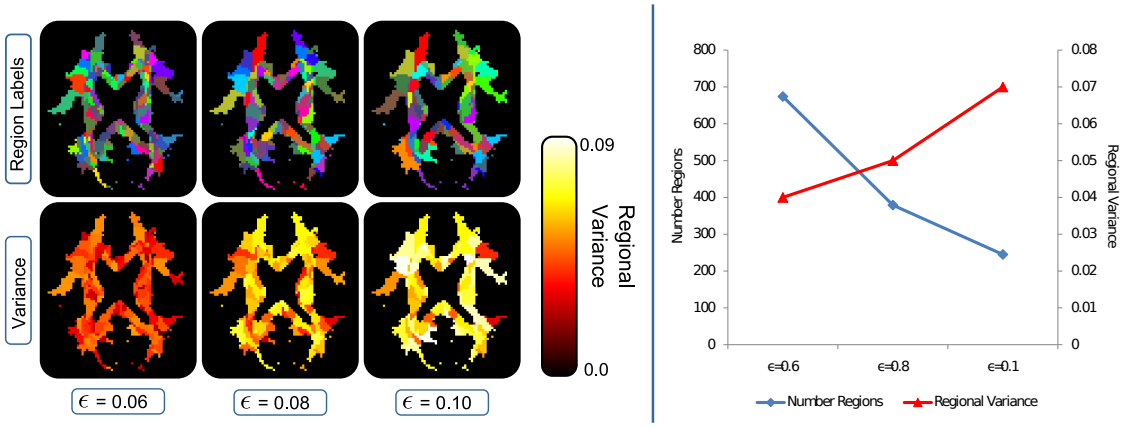

Figure 4.2: As the stopping variance threshold, ϵ, is decreased, the expected decrease in the regional FOD variance is seen. This decrease coincides with an increase in the number of regions, as well as, an increase in the coarseness of the parcellation results.

method was applied, using the population average FOD image to model the WM architecture and using the population WM mask to identify WM voxels.

An investigation of the parameters used to define the WM similarity kernel, σ_s and σ_f, as well as the stopping variance threshold, ϵ, was performed. Adjusting the σ_f and σ_s parameters had the expected behavior of controlling the spatial smoothness of the determined regions. Similar results, in terms of both the number of regions, average region size, and average regional FOD variance were found when varying σ_s in the 0.1 – 0.3 range and σ_f in the 6mm – 10mm range. Adjusting ϵ has the most direct effect on the resulting parcellations as it determines at what point the subdivision process is halted. Figure 4.2 shows the results of our method as ϵ is changed between 0.06 and 0.1. As ϵ is decreased there is a clear decrease in the regional variance as well as an increase in the number of regions determined, resulting in finer regional delineation. This relationship, between the achieved regional variance and the number of regions, suggests that in practice this parameter must be tailored to the population under study as well as to the intended use of the derived atlas regions.

Based on these results, two atlases were generated. A coarse atlas generated using the parameters $\sigma_s = 6mm$, $\sigma_f = 0.3$ and $\epsilon = 0.15$ and a finer atlas using a lower halting

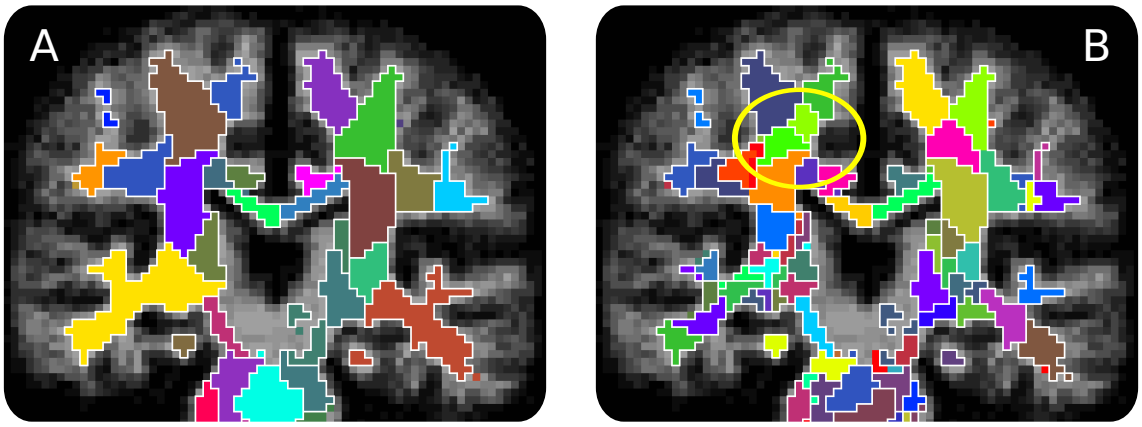

Figure 4.3: The general anatomical bilateral symmetry is apparent in the atlas regions. At a higher stopping variance of $\epsilon = 0.15$ (A), this symmetry is more apparent than in the finer regions obtained using a lower stopping variance of $\epsilon = 0.08$ (B) where the division of complex regions is more heavily influence by the local characteristics of the data. For instance the two regions circled in panel B correspond to a single contralateral region.

threshold of $\epsilon = 0.08$. The iterative nature of the parcellation algorithm yields a hierarchical relationship between these atlases, with the $\epsilon = 0.15$ regions being supersets of the $\epsilon = 0.08$ regions. The finer atlas consists of 379 spatially compact regions with an average regional size of 105 $(2mm)^3$ voxels and a mean regional FOD variance of 0.06, while the coarse atlas

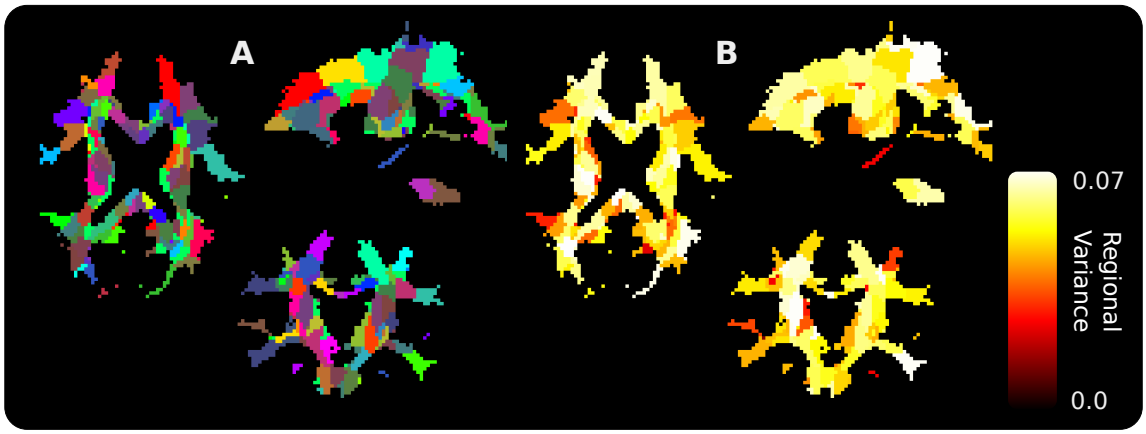

Figure 4.4: Population Atlas generated from 23 young adolescents generated using the parameters $\sigma_s = 6mm$, $\sigma_f = 0.3$ and $\epsilon = 0.08$. Representative slices are shown of the label map identifying homogenous WM regions (**A**) and the corresponding FOD variance (**B**) images.

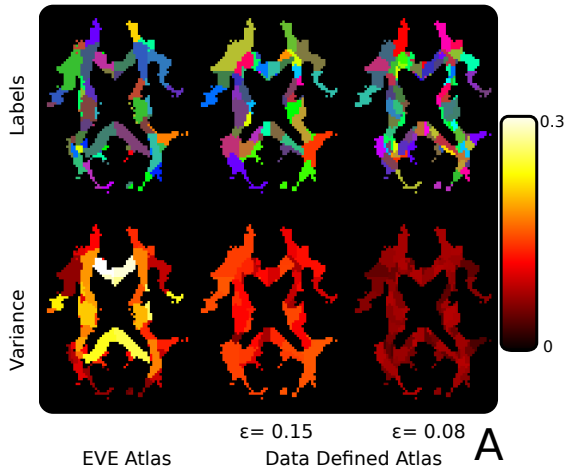

	Eve	Data Defined (ε=0.15)	Data Defined (ε=0.08)
Number of Regions	127	94	379
Mean Regional Variance	0.12	0.10	0.06
Max Regional Variance	0.30	0.15	0.08

B

Figure 4.5: Representative slices of the EVE-DTI atlas' anatomically defined regions and their corresponding regional FOD variances are shown in panel **A**, compared with the data defined WM regions generated using two stopping variances $\epsilon = 0.15$ and 0.08. The EVE-DTI anatomical regions are conspicuously more heterogeneous, indicated by high regional variance, even in central WM areas. A table listing characteristics of each parcellation is shown in panel **B**.

consists of 94 regions with an average regional size of 423 $(2mm)^3$ voxels and mean regional FOD variance of 0.10. Representative coronal slices of the coarse and fine atlases are shown in Figure 4.3. The rough bilateral symmetry of the regions is clearly visible in the coarse atlas, while at the finer scale the bilaterality is less apparent particularly in complex WM regions. Figure 4.4 shows representative slices of the finer atlas and corresponding regional variance maps. The orientation sensitive aspect of the similarity kernel groups voxels with similar orientation, as seen in the genu and splenium of the corpus callosum, while sensitivity to the WM complexity aids in parcellating the cortical WM.

We utilized the EVE-DTI atlas to create an anatomical WM parcellation that would be used both as a comparison as well as to provide our data defined regions with anatomical context. This was achieved by using a nonlinear spatial normalization algorithm to transform the structural, T1 weighted image provided as part of the EVE-DTI atlas into the space defined by the group average T1-weighed image (T1-weighted images were used for registration as this was the common modality between the HARDI population and the DTI anatomical

atlas). Using this deformation field, the anatomical labels provided by the EVE-DTI atlas were then transformed into the template space yielding an alternative parcellation. Figure 4.5 shows a comparison between the population atlases, generated using $\epsilon = 0.15$ and $\epsilon = 0.08$, and the anatomical regions inherited from the EVE-DTI atlas. A clear improvement in regional FOD variance is achieved using the $\epsilon = 0.15$ data driven atlas regions, with a further improvement at the expense of generating a moderately larger number of regions when using the finer atlas ($\epsilon = 0.08$).

4.5. Conclusions

The proposed automated atlas building procedure utilizes HARDI data and the FOD diffusion model, to provide improved contrast in complex WM regions using a novel data-driven WM parcellation algorithm. This algorithm allows automated regional labeling based on models of the local WM architecture, as opposed to the traditional time consuming anatomical labeling. The automatic nature of these methods permits researchers to generate their own atlas based on the datasets of their specific study. This overcomes many issues that occur when attempting to use published atlases, such as different clinical populations (ages) or different imaging protocols being utilized to generate the atlas.

Similar to the cytoarchitectural mapping of the brain [27], where local variations in cell type are used to delineate cortical regions, our method uses the FOD as a non-invasive imaging measure of local tissue architecture to delineate WM regions. Through the application of this methodology to the problem of generating an age specific population atlas, adolescent and pre-adolescent healthy subjects in our case, we show that these regions are more homogenous, with respect to WM orientation and complexity, than the regions inherited from an existing DTI based anatomical atlas. This suggests that these regions are better suited for regional statistical analysis or the extraction of regional features of WM architecture to be used in subsequent applications such as pattern classification and are thus perhaps more faithful to the overall goal of identifying regions of biological homogeneity.

The generation of the illustrative WM atlas (Section 4.4) demonstrates that the proposed

WM parcellation method outperforms the typical processing methods that are generally utilized for determining WM atlases. A comparison between the anatomical regions of the EVE-DTI atlas and those determined by our method, shown in Figure 4.5, demonstrate the benefit of using data-driven regions to represent local WM architecture, through the marked decrease in regional FOD variance. This decrease suggests that the data determined regions are more tightly related to the local WM anatomy, which may have significant benefits when examining clinical populations (e.g., schizophrenia, autism spectrum disorder). While bilateral symmetry is not considered in the region delineation process, the roughly bilateral nature of WM anatomy is still clearly apparent in the data defined regions, shown in Figure 4.3, particularly at the coarser spatial scalars.

The proposed framework provides three parameters which effect the regions that are determined. Of these three, the stopping criterion, ϵ, has the most pronounced effect on both the number of regions determined and, more significantly, the regional variances of these regions. The other two parameters, σ_s and σ_f, determine the kernels used in the similarity functions, effecting the smoothness of the ROIs, in the spatial and feature domain and in turn, the number and size of the resulting regions, but have little effect on the regional variances of the regions. In practice, selection of ϵ should be based on the desired degree of uniformity required for the regions while the other parameters are best set based on qualitative assessment of the resulting atlas. This process need only be done once for a new population and requires little effort, particularly when compared with the process of manually correcting anatomical regions.

The stability of the clustering, in terms of specific boundary locations, is mainly governed by the robustness of the population average. For this reason it is important to ensure that a sufficient number of subjects are used to make up the population average. If this number is suitably large the effect of additional subjects on the population average and thus on the parcellation results will be negligible. In practice, the study specific atlas is generated when the study is ready for a statistical analysis, having reached a suitable sample size determined by the study's power calculations, and reflects the local variation in the specific

dataset.

The fact that a general atlas generation methodology is described as opposed to simply the description of a single population HARDI atlas, like the ICBM-DTI-81 [119], is indicative of the belief that optimal results from a group study are obtained when the specific traits of the population and data are utilized. While we have focused on WM, developing novel clustering methods based on the state of the art modeling of WM architecture, the central theme of this work is applicable to many other atlas building problems. For instance GM regions could be parcellated based on their structural and functional connectivity profiles, ostensibly generating regions that more closely respect the structure/function relationship within the population under study.

CHAPTER 5 : Structural Connectivity

5.1. Introduction

The *in-vivo* mapping of brain connectivity, either structurally or functionally, is now often included in research studies investigating neuronal development [72], as well as specific diseases such as attention deficit hyperactivity disorder [94] and schizophrenia [192]. This new analysis paradigm seeks to utilize fiber tracking algorithms and diffusion weighted DW-MRI, to elucidate the anatomical connections that exist between various brain regions.

With this goal in mind, there are two traits which could be expected from a structural connectivity framework. First, while DW-MRI possesses information concerning the orientation of the local WM anatomy, it cannot distinguish between afferent and efferent axonal fiber bundles. Thus the functional directionality of the axonal fiber bundles connecting two regions cannot be determined and one should expect a symmetric structural connectivity measure between any pair of regions (the measure from A to B should equal that from B to A). Secondly, the anatomical connections we would like to model, namely axons, originate and terminate from neurons located within the GM. While many of these are commissural or long association tracks, others are short range connections between regions within the same gyrus or neighboring gyri. Thus we would expect that contrast provided by the paths of the connections to be somewhat evenly balanced between the major central WM tracks and the more cortical WM.

The most prominent work on structural connectivity [70, 71, 193] rely on whole brain tractography to provide a single set of fiber streamlines that are used to represent the axonal fiber bundles of the brain. Connectivity weights between GM regions are determined by counting the number of streamlines whose endpoints lie within those regions, sometimes normalized by the length of the tracks. These streamlines can also be used to generate fiber or track density imagings (TDIs) [31] providing a WM contrast by counting the number of streamlines passing through each voxel. Thus both the track density images and the

connectivity weights between GM nodes are descriptions of the same set of fiber tracks used to represent structural connectivity.

These methodologies, by using fiber streamlines as surrogate fiber bundles, achieve the symmetry expected from a structural connectivity measure. However, the use of every voxel, either white or gray matter, as a fiber tracking seed causes an oversampling of large central fiber bundles that traverse many voxels. In the process, shorter U-fibers or association fibers are under sampled, which might be problematic for studies of pathologies such as autism, that may require the investigation of short as well as long range connectivity.

Alternative approaches have been proposed that track directly from the GM nodal regions. Robinson et al. [140] uses a probabilistic monte-Carlo (MC) based fiber tracking [22] strategy, where the paths of individual particles are tracked, to determine the connecting fibers between regions. Gong et al. [63, 64] use MC fiber tracking to compute the connection probability between two nodes. The inherent dependence on the seed region generates a non-symmetric connectivity measure which is also difficult to attribute a physiological meaning to.

Several approaches have been proposed that combine anisotropy measures with fiber tracking methods, to produce a connection weight between nodes. The authors of [89, 90] determine the most probable path connecting any two nodes. The connection weight is then determined as the lowest anisotropy along that path. Similarly, Robinson et al. [140] integrate the anisotropy along MC generated paths yielding a connection weight. An additional confound of the MC based methods is the dependence on the number of particles used in the model. The use of smaller GM nodal regions necessitates an increased number of particles per region, placing an additional computational burden on the model.

The goal of this work is to present a structural connectivity framework designed explicitly around the physiological constraints discussed above. The method utilizes a discrete stochastic tractography algorithm, similar to [86], to model the transition of particles through the neuronal WM volume. The efficiency of this approach allows the investigation

of large networks of small nodal regions, yielding a more detailed description of a subject's connectivity, while removing the dependence on the number of particles, as required for modeling by the MC techniques. Using the discrete stochastic tractography algorithm, we compute a conditional probability matrix relating the GM regions that serve as nodes in the structural connectivity network. The network nodes are defined along the boundary of the WM volume, avoiding the preferential sampling of larger fiber bundles that occurs when seeding directly in WM voxels.

From the conditional probability matrix, we determine the nodal connection density (nCD), defined as the steady state distribution of particles terminating at each nodal region. The nCD is computed by an optimization framework incorporating physiologic constraints, namely the conservation of structural connections, as well as, the expected symmetry of the final structural connectivity matrix. This provides an *in-vivo* contrast for GM regions that may prove interesting in investigating pathologies which affect local connectivity and cytoarchitecture. The structural connectivity matrix is then computed by combining the nCD and the conditional probability matrix. This removes the conditional dependence on the seeding regions, while imparting the connectivity measure with a physiological interpretation, proportionality to the number of physical connections between regions. Finally, the nCD can be mapped back into the WM voxels yielding a WM connection density image whose contrast is based on the number of particles traversing each voxel. This image provides a means to investigate spatial differences in WM integrity and, perhaps, focal effects of pathology.

5.2. An Integrated Structural Connectivity Framework

Our method is built upon a similar foundation of other probabilistic fiber tracking techniques. Namely, we compute a probability distribution function at every voxel of a subject's DW-MRI dataset, describing the orientation of the anatomical fibers. In this work, the normalized FOD function is used for this purpose, although other models could be used. From the FOD field and a parcellation of the brain identifying the GM nodes and the WM voxels,

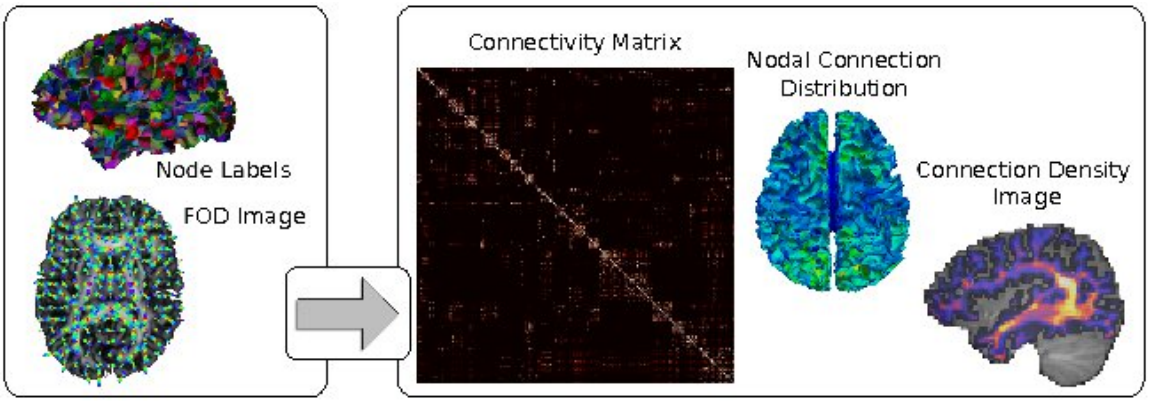

Figure 5.1: The framework utilizes a set of GM nodal regions and an FOD image to determine three features related to the structural connectivity of the subject: 1) a structural connectivity matrix (only left hemisphere is shown) describing the number of connections between each pair of nodes, 2) the nCD, describing the proportion of connections terminating in each node, and 3) a connection density image describing the density of connections as they traverse the WM.

we seek to determine a measure proportional to the number of physical connections between the GM nodes, culminating in the creation of the *structural connectivity matrix*. In doing so, two other connectivity features are computed: the *nodal connection distribution* and the *connection density* image. These three elements, seen in Figure 5.1, possess different information concerning the structural connectivity of the individual and could potentially be useful for a variety of tasks, ranging from characterizing and localizing group differences, to identifying novel structural and functional parcellations of the cortex. The details of procedure are discussed below.

Conditional Probability Matrix Computation

The first part of the framework is the computation of the conditional probability matrix ($\mathbf{C}$). This matrix describes the likelihood that fibers terminate in a specific GM node, given that the other end is known to terminate in another specified GM node. This is accomplished by modeling the transport of particles assumed to travel along anatomical fiber pathways through the WM. The method determines each element of this matrix, $(\mathbf{C}_{ij})$, as the proportion of particles injected into the system from the j^{th} node, that traverse the WM volume and exit into the i^{th} node. This approach shares the basic assumption of the

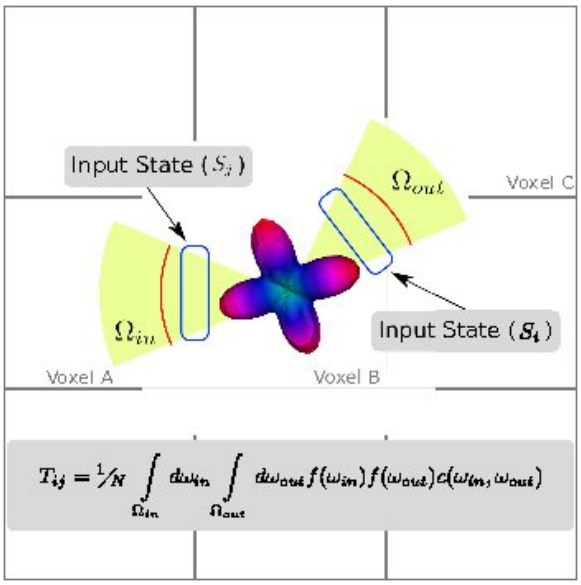

Figure 5.2: States are defined as directed voxel edges. S_j describes particles traveling from voxel A to B, while S_i describes those moving from B to C. The transition probability between these states ($\mathbf{T}_{ij}$) is defined by integrating the product of the FOD, at the intermediate voxel (voxel B) evaluated at the acceptance angle (ω_{in}) and the outgoing angle (ω_{out}) and a directional coupling term ($c(\omega_{\text{in}}, \omega_{\text{in}})$), which penalizes large deviations.

MC fiber tracking approaches [22, 64], namely that particles will travel along the underlying anatomical fibers. However, as opposed to modeling the transport of each particle individually, making the accuracy dependent on the total number of particles simulated, a Markov process is used to model the transport of a population of particles through the WM, allowing the conditional probability matrix to be efficiently computed.

The efficiency of this approach derives from the discretization of the states that particles traversing the WM volume can take. The collection of these states ($\mathcal{S}$) make up the state space of the Markov process. A state is defined as a directed edge of the WM voxels (see figure 5.2), and is, therefore, fully described by its base voxel and its target voxel. A state, S_j in Figure 5.2 for instance, representing particles moving from voxel A into voxel B, would have a base voxel A and target voxel B. In order to aid in determining feasible connections between states, each state is labeled based on the tissue types it connects. The available labels are WM-internal (WM to WM transitions), CSF-boundary (WM to CSF transitions), GM-out (WM to GM transitions) and GM-in (GM to WM transitions).

For each voxel in the WM region, 26 states are formed, connecting the WM voxel to its 26 spatial neighbors. Each of these states is formed by the WM voxel acting as the base voxel and the neighboring voxel acting as the target voxel. These states are labeled as WM-

internal, CSF-boundary, or GM-out based on the segmentation label of the target voxel. Once all the WM voxels and neighbors have been visited, we determine the GM-in states by inverting the base and target voxel of each GM-out states. The GM-in and GM-out states are then investigated to identify which GM nodes they are interacting with. This information is used to build two linear operators that map from the state space ($\mathcal{S}$) to the space defined by the GM nodes ($\mathcal{N}$). The first operator, $\mathbf{B}$, describes the mapping from $\mathcal{N}$ to the incoming GM boundary states of $\mathcal{S}$. While the second operator, $\mathbf{L}$, describes the mapping from the outgoing GM boundary states to the GM nodes. For instance, if $\mathbf{g}$ is a distribution of particles in the GM nodes (a vector in $\mathcal{N}$), then $\mathbf{L}\,\mathbf{g}$ represents those particles entering into state space of the system. Similarly, if $\mathbf{s}$ is a distribution of particles in the state space, then $\mathbf{B}\,\mathbf{s}$ yields the number of particles that are transitioning out of the WM system into each of the GM nodes.

With the state space fully defined, we can describe how a distribution of particles (represented as a state vector) evolves in time. This evolution is governed by the transition matrix ($\mathbf{T}$), where the ij^{th} element, $\mathbf{T}_{ij}$, is the probability that particles in the j^{th} state will be in the i^{th} state at the next time point. Once $\mathbf{T}$ is defined, the dynamics of the system are expressed as, $\mathbf{s}_t = \mathbf{T}\,\mathbf{s}_{t-1}$ where s_t and s_{t-1} are state vectors at time step t and $t-1$ respectively.

The computation of each $\mathbf{T}_{ij}$ is made simpler by considering the tissue types connected by the first state. For instance, if S_j is a GM-out state, then its particles are leaving the WM system and not transitioning to other states, resulting in $\mathbf{T}_{ij} = 0$ for all possible target states(S_i). Alternatively if S_j is either a WM-internal or GM-in state, then $\mathbf{T}_{ij}$ is computed only for situations, like those shown in figure 5.2, where the transition from S_j to S_i represents a continuous trajectory, meaning that the base voxel of state S_i is the target voxel of S_j. Transitions to non connected states cannot occur, resulting in a transition probability of zero.

Figure 5.2 demonstrates a case where the transition probability is non-zero. In this case,

the transition probability is the likelihood that fibers travel from voxel A through voxel B and then into voxel C. The possible incoming particle trajectories connecting B and A are designated by the solid angle, Ω_{in}. Similarly, Ω_{out} describes the possible exit trajectories into voxel C. Thus a possible trajectory through voxel B consists of a pair of incoming and outgoing directions, ω_{in} and ω_{out}. The likelihood that a particle would take that path through the voxel, is the product of voxel B's normalized FOD, f, evaluated at those two directions, multiplied by a coupling or inertia term ($c(\cdot)$) that penalizes large turning angles. By integrating this product over the incoming and outgoing solid angles we arrive at the final transition probability connecting S_j to S_i:

$$T_{ij} = \frac{1}{N} \int_{\Omega_{\text{in}}} \int_{\Omega_{\text{out}}} f(\omega_{\text{in}}) f(\omega_{\text{out}}) c(\omega_{\text{in}}, \omega_{\text{out}}) \, d\omega_{\text{out}} \, d\omega_{\text{in}} \tag{5.1}$$

where $N = \int_{\Omega_{\text{out}}} f(\omega_{\text{in}}) f(\omega_{\text{out}}) c(\omega_{\text{in}}, \omega_{\text{out}}) \, d\omega_{\text{out}}$ normalizes the transition probabilities. Making columns of $\mathbf{T}$ sum to 1 ensures that every particle that enters a state, transitions to a subsequent state in the next time point.

In this work, $c(\cdot)$ is chosen to have the form of rejecting turns greater than 60°, which has the desired result of greatly reducing particle deflections greater than 90°. Other cutoffs are possible; however, preliminary results indicated that variations of up to 10° had little effect on the final connectivity result. Finally, because physiological fibers do not terminate in the CSF, the CSF boundary is treated as a particle sink, absorbing all particles that enter it, by zeroing the transition probabilities into states connecting WM and CSF voxels and then renormalizing the transition probabilities of those states.

With the dynamics of particle transport defined, the steady state behavior of the system under a constant input can be examined. Let $\mathbf{b}$ be a state vector describing a distribution of particles being injected into the system from the GM nodes. The dynamics of the system are captured by $\mathbf{s}_{t+1} = \mathbf{T}\,\mathbf{s}_t + \mathbf{b}$, allowing for the computation of the equilibrium state

vector ($\mathbf{x}$) as

$$\mathbf{x} = \mathbf{T}\,\mathbf{x} + b \tag{5.2}$$

$$\mathbf{x} = (\mathbf{I} - \mathbf{T})^{-1} b \tag{5.3}$$

This approach possesses a number of advantages over methods which track the progression of a single bolus of particles [86]. First, by utilizing the equilibrium behavior of the system, as opposed to tracking an initial impulse of particles, this method is immune to geometries where particles exit the system very slowly, such as circular paths or loops. Secondly, while the matrix $(\mathbf{I} - \mathbf{T})$ is not easily invertible, due mainly to its high dimensionality, robust software tools [16, 82] exist for efficiently solving such systems. Finally, this approach allows us to directly express a formula for the conditional connectivity matrix ($\mathbf{C}$) relating the GM nodes

$$\mathbf{C} = \mathbf{L}\,(\mathbf{I} - \mathbf{T})^{-1}\,\mathbf{B} \tag{5.4}$$

where $\mathbf{B}$ is used to map a distribution in the space of GM nodes ($\mathcal{N}$) into the state space or the system ($\mathcal{S}$), $(\mathbf{I} - \mathbf{T})^{-1}$ determines the equilibrium behavior and finally $\mathbf{L}$ maps the outgoing particles of the equilibrium state into their destined GM nodes. In this way, $\mathbf{C}_{ij}$ is the proportion of particles injected into the system from the j^{th} node that exit the WM volume into the i^{th} node and is equivalent to a conditional probability.

The algorithm used for computing $\mathbf{C}$ solves for each column individually, essentially solving for the conditional connectivity of each GM node individually. The first step of this procedure is to compute an ILU preconditioner for the operator $(\mathbf{I} - \mathbf{T})$. Then for each column of $\mathbf{B}$, we use an iterative solver to compute $\mathbf{x} = (\mathbf{I} - \mathbf{T})^{-1}\,\mathbf{B}_{:i}$, where $\mathbf{B}_{:i}$ is the i^{th} column of $\mathbf{B}$. Both the preconditioner and the iterative solver are supplied as part of the Trilinos [82] software package. Once $\mathbf{x}$ is determined, the corresponding column of $\mathbf{C}$ is filled with $\mathbf{L}\,\mathbf{x}$. This approach can be fully parallelized, allowing for multiple columns of $\mathbf{C}$ to be determined simultaneously.

Nodal Connection Density and the Connectivity Matrix

The columns of $\mathbf{C}$ describe the proportions of particles traveling from one GM node to another. For instance, if $\mathbf{C}_{ij} = 0.25$, then one quarter of the particles entering the WM from the j^{th} node, exit into the i^{th} node. Under the assumption that particle traffic between nodes is proportional to the number of anatomical connections between those nodes, this implies that a quarter of the connections that terminate at the j^{th} node have their other endpoint in the i^{th} node. If the distribution of connections across the GM nodes, the nCD, is known, it can be combined with the conditional probability matrix ($\mathbf{C}$) yielding a connectivity matrix, $\mathbf{M}$, where each element is proportional to the number of connections between each pair of nodes.

$$\mathbf{M}_{:i} = \mathbf{C}_{:i}\, d_i \tag{5.5}$$

$$\mathbf{M} = \mathbf{M}\,\mathbf{D} \tag{5.6}$$

where $\mathbf{D}$ is a diagonal matrix with the nCD, $\mathbf{d}$, along the diagonal.

The nCD is computed via an optimization problem that stipulates that the number of incoming connections from the other nodes must equal the number of connections outgoing from that node. As this may not lead to a unique solution, we also require that $\mathbf{M}$, computed by equation 5.5, is symmetric. Thus $\mathbf{d}$ should obey the following relations

$$\mathbf{d} = \mathbf{C}\,\mathbf{d} \tag{5.7}$$

$$\mathbf{M} = \mathbf{M}^t \tag{5.8}$$

These constraints, combined with the non-negativity of $\mathbf{d}$ ($\mathbf{d}_i \geq 0; \quad \text{for all} i$) and the requirement that the elements of $\mathbf{d}$ sum to 1, form a convex quadratic optimization problem which is solved using the cvxopt[1] software package.

[1] http://abel.ee.ucla.edu/cvxopt/

White Matter Connection Density Maps

Once the nCD has been computed, the Markov model can be used to map those connections from the nodes back into the WM volume, generating an image displaying the concentration of connections as they traverse the WM. This is accomplished by using the steady state model to map nCD ($\mathbf{d}$) into the states space via

$$\mathbf{s} = (\mathbf{I} - \mathbf{T})^{-1}\,\mathbf{B}\,\mathbf{d} \tag{5.9}$$

The connection distribution in the state space, $\mathbf{s}$, is then mapped into the image space using the base index of each state as the imaging voxel containing those connections, resulting in an image of the spatial distribution of connections throughout the WM volume.

In summary, the presented framework represents the structural connectivity of an individual using three interconnected measures: the nCD describing the percentage of connections terminating in each of the GM nodal regions, the connection density images describing these connections as they traverse the WM and finally the structural connectivity matrix representing the interconnections between all of the GM nodes in a holistic fashion.

5.3. Validation: *In-vivo* Human Datasets

There are two traits that are critically important to the utility of any proposed measure of anatomy or biology. First, a measure must be reliable, meaning that if two measurements are performed sufficiently close in time, such that one could expect no anatomical difference, these two measurements should be the same. Secondly, in order to be of use, a measure must be sensitive to the biological variation that exists between individuals. The sensitivity and repeatability of the proposed method was evaluated on a DW-MRI dataset consisting of imaging 9 subjects (2 Female/7 Male, Age 31.25 $\pm$ 4.2 years) at two time points separated by two weeks. A full description of the imaging parameters can be found in Section A.1.3.

The FOD image for each subject was computed using the procedures described in Section

A.2. The nonlinear, FOD based, spatial normalization method, discussed in Chapter 3, was used to register each subject's FOD to that of a template FOD image, where nodal regions were defined. The registered FOD images where then normalized yielding an image of FODs each with unit integral to be used to compute the transition probabilities.

Nodal regions were determined within the template coordinate system by first segmenting the structural image of the template, into GM, WM, CSF using Freesurfer [55]. The set of GM nodes was determined by downsampling the GM tissue segmentation, to an isotropic resolution of 8mm. Each of these GM voxels were then given a unique label and then resampled at the native 2mm resolution. This yielded a set of 2744 unique GM nodes comprised of both cortical and sub-cortical regions. Additionally each GM node was assigned an anatomical label from the Desikan atlas [50].

Using this set of 2744 GM nodes, a structural connectivity matrix, a node connection distribution and a connection density image were computed for each subject. In order to aid in visualization and provide a means of comparability to published methods, the connectivity matrices were downsampled to the anatomical nodes defined in the Desikan atlas. Each of the 2744 nodes corresponding to the same anatomical label, had its rows and columns summed to create a connectivity matrix in the coarser GM node space.

Repeatability of Measures

Two measures, the Pearson's correlation coefficient and the average percent error, were used to measure the reliability of each of the three components of the proposed framework. For each WM voxel, the connection densities at time point 0 were correlated to those at time point 1, yielding a correlation coefficient at every voxel. Similarly, the values of the nodal distribution and of the non-zero weights of structural connectivity matrix, determined by a student's t-test thresholded at $p < 0.025$, can be used to generate correlation coefficients for each of these measures. These are shown in Figure 5.3-A, along with a box plot illustrating the spread of these correlation coefficients. Similarly, Figure 5.3-B, displays the percent error of these measures computed at each WM voxel, GM node and connectivity weight.

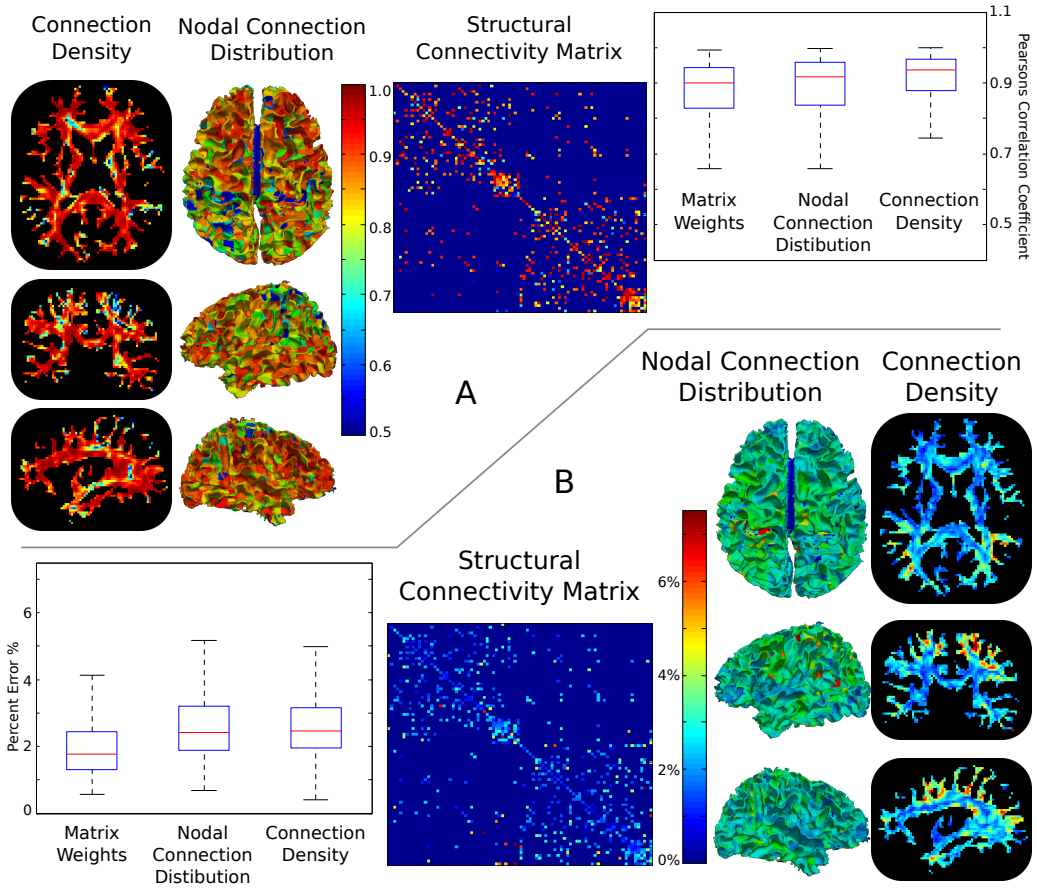

Figure 5.3: Results from a test/retest study performed on nine subjects scanned at two time points two weeks apart. Pearson's correlation coefficients computed from each WM voxel's connection density value, each GM node's nodal distribution value, and each non-zero ($p < 0.025$) connection weight, are shown in **A**. **B** shows the percent error of each of these measures. The high correlation coefficients, typically above 0.75, and low percent errors ($\leq 5\%$) are indicative of a highly repeatable measure.

The majority of measures obtained correlation coefficients above 0.75 and errors below 5%, demonstrating the high degree of repeatability of the proposed method.

The sensitivity of the proposed framework to differences in individual anatomy was investigated by quantifying the degree that each of these measures can be used to differentiate between subjects. For each measure the difference between any two subjects was computed using the L_2 difference of the measures. The difference between the connection density images of two subjects was computed as the square root of the sum of squared difference in connection density of every WM voxel. Similarly the differences in nCD and structural

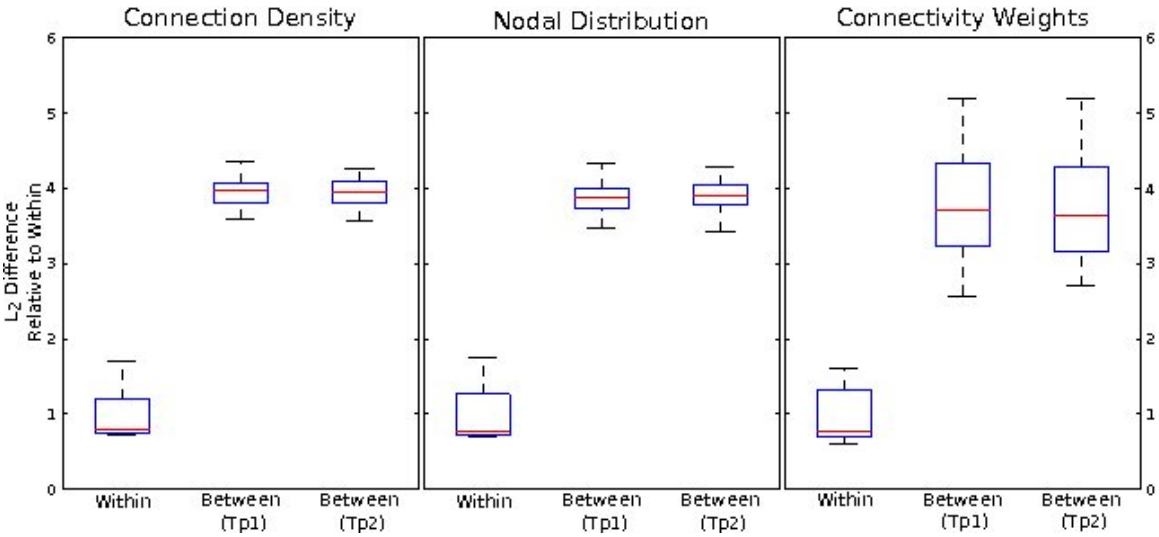

Figure 5.4: Boxplots indicating the average L_2 difference between connection density images, nodal distributions and connectivity matrices derived from the same subject ('Within') and different subjects at each time point ('Between TP1 and TP2'). The average difference between subjects is roughly 4 times higher than the difference within the same subject, indicating that these measures are able to capture individual anatomy and may be able to reveal group differences.

connectivity matrix were computed as the square root of the sum of squared difference of the nCD at every node and the difference of each non-zero connection weight respectively. Non-zero connection weights were determined by a student's t-test thresholded at $p < 0.025$. Boxplots showing the average inter (between) and intra (within) subject differences for each of these measures are shown in Figure 5.4.

Population Averages

In order to demonstrate the contrasts provided by the three measures computed as part of the proposed method, population averages were computed using the DW-MRI data of each subject's first time point. The high repeatability of the measures suggest that either time point would have sufficed to illustrate these principles, thus the use of the timepoint 0 dataset is justified. For the remainder of this section, unless otherwise specified, the term population average refers to the average computed only from the initial timepoint.

While the utilization of smaller nodal regions provides useful information (Figure 5.5-B), the

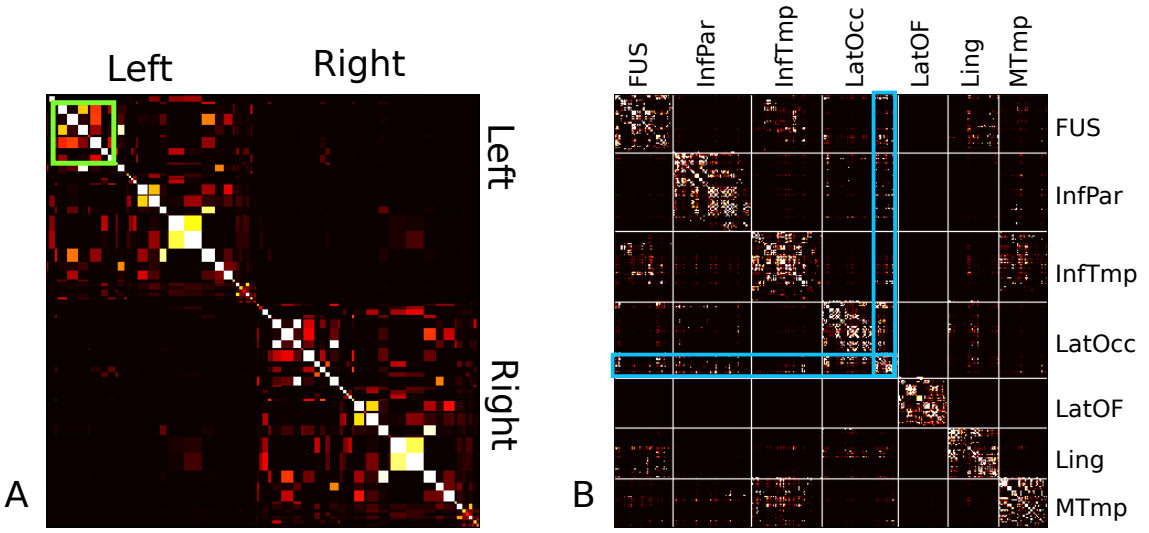

Figure 5.5: The average connectivity matrix (A), computed using the Desikan atlas. A large number of self connections (along the diagonal) are evident. The average connectivity matrix in the 8mm nodes (B) for a section (green inset) of the larger network consisting of the fusiform (FUS), the inferior parietal (InfPar) and inferior temporal (InfTmp) lobes, the lateral occipital (latOcc), lateral oribital frontal (LatOF) and lingual (Ling) cortices and the middle temporal (Mtmp) lobe. A clear structure of inter-regional connections is evident within these larger anatomical nodes, as well as, in the connections between them. An example of such a network involving the latOcc is highlighted in blue.

direct visualization and interpretation of entire structural connectivity network consisting of 2744 GM nodes is difficult. As many of the published works have been on smaller anatomically defined node definitions, we downsampled the connectivity matrices. Figure 5.5-A shows the population average connectivity matrix downsampled to the anatomical (Desikan) nodes. Figure 5.5-B shows a portion of the higher resolution connectivity matrix for 7 anatomically defined nodes, highlighted in green, in Figure 5.5-A.

The population average nCD, computed from the 2744 GM regions, mapped to the surface separating cortical gray and white matter of the template subject, is shown in Figure 5.6-A. The population histogram (Figure 5.6-B) of the coefficients of variation (the ratio of the standard deviation to the mean) of the nodes, shows all values to be below 0.55 with the majority below 0.25. The peak of the histogram of coefficients of variation occurs around 0.15 indicating that for most GM nodes the population average nCD value is 6.5 times its

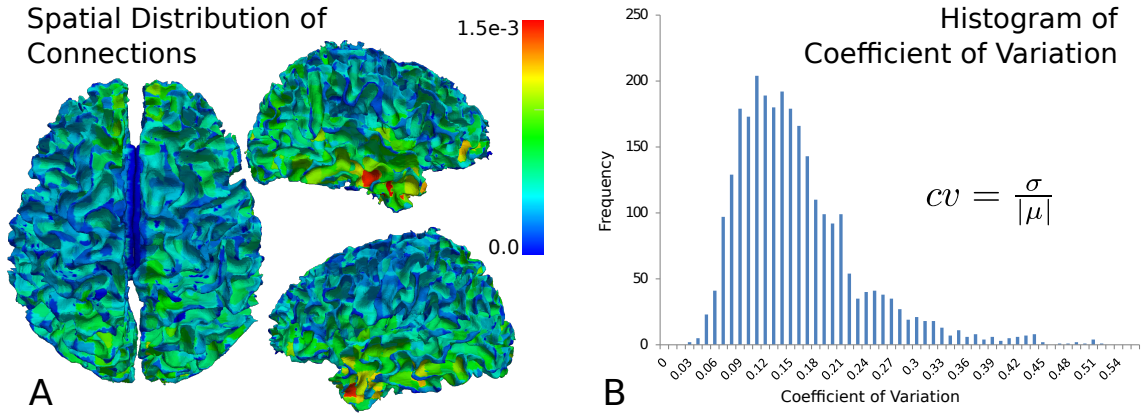

Figure 5.6: The average nodal connection distribution (A) mapped to the gray/white matter surface. The nodal connections possess a rough bilateral symmetry, with areas of increased connections found in the temporal lobe. A histogram (B) of the nodes coefficient of variation (ratio of the standard deviation to the mean) shows values predominantly below 0.5, indicating the relative low variance of the nodal connection distribution in the population

standard deviation in the population.

The CC is one of the few pieces of neuronal WM anatomy where research has focused on

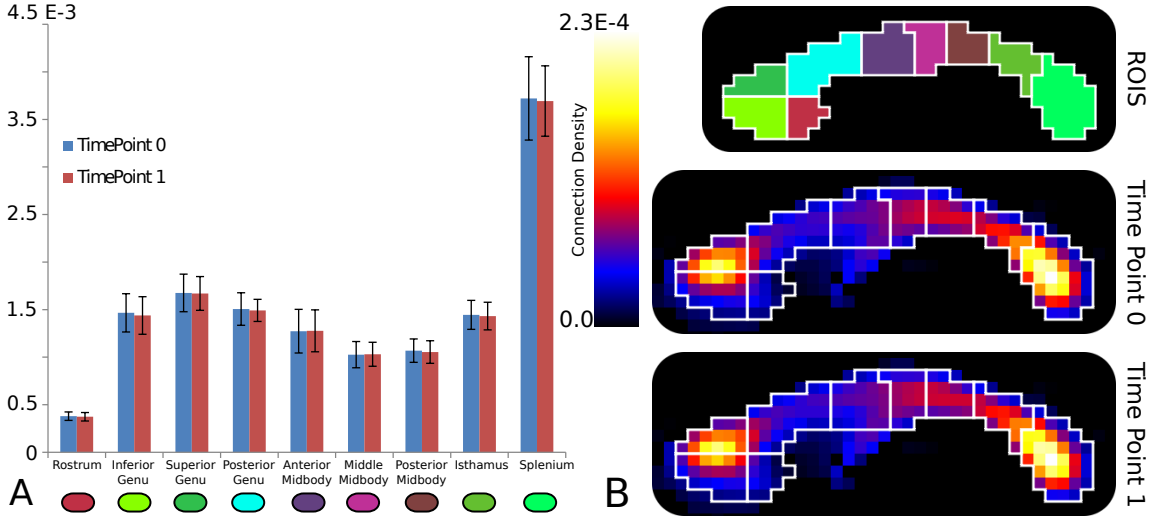

Figure 5.7: The spatial distribution of the connections through the mid-sagittal slice of the corpus callosum is shown. The distribution, with high concentrations in the splenium and genu, shows agreement with existing studies where fiber count was determined from histopathology [84]

quantifying, via histology, the number of axons that pass through it. The spatial distribution of connections passing through the mid-sagital CC was computed by summing the connection density images within each component of the CC thereby providing a means to compare the proposed method with the more invasive histological methods that have been used previously. The population average, for both timepoints, can be seen in figure 5.7-A, while the population average connection density images, as well as, the 9 sub-regions of the CC can be seen in figure 5.7-B.

Additionally, a comparison of the connection density images to an existing method was preformed. Track density images (TDI) were generated using a probabilistic tracking algorithm seeded in all brain voxels (TDI-WholeBrain), as well as, when seeded only in the GM (TDI-GM) nodal regions. TDI images were computed using a set of streamlines ($N = 750,000$) determined via probabilistic tractography using the MRtrix (Brain Research Institute, Melbourne, Australia, http://www.brain.org.au/software/) software and the parameters specified in [31]. The stopping threshold was decreased from 0.1 to 0.05, to better fit our datasets. The coefficient of variation (CV), the ratio of the standard deviation to the mean, was computed for each WM voxel yielding a CV image for each of these three images (connection density, TDI-WholeBrain and TDI-GM). Representative slices of the differently seeded TDI images, as well as, a histogram of their CV values can be seen in Figure 5.8. A contour of $CV = 0.25$ is overlayed on each image, indicating areas that have a low population variance to mean ratio. The TDI-wholebrain CV histogram consists of lower values indicative of a signal more conserved throughout the population. Population average TDI-WholeBrain and Connection Density images can be seen in figure 5.9-A. To provide a comparable contrast, these images were normalized by their average values in the mid-sagital corpus callosum prior to performing the averaging. The CV histogram of these images, prior to the normalization, can be seen in 5.9-B.

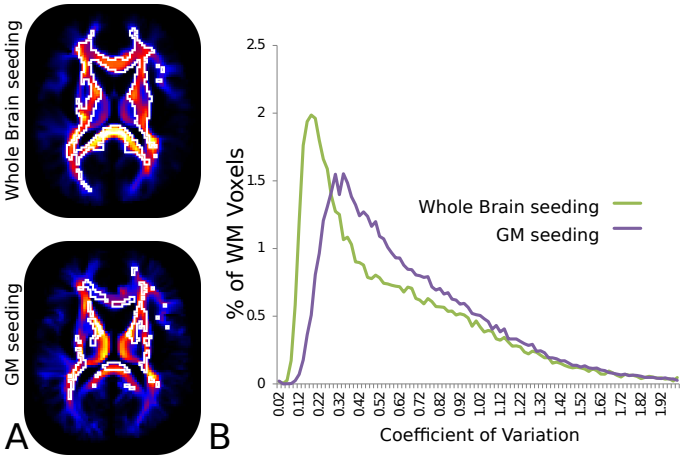

Figure 5.8: Population averaged TDIs generated using traditional probbalisitic tracking methods seeded in the whole brain and only in the GM are shown in **A**, where the white line delineates the contour of the CV thresholded at 0.25, indicating areas of low population variance. Coefficient of variation histograms(CV), **B**, computed from the WM voxels of the track density images.

5.4. Discussion

As the use of structural connectivity to investigate population differences becomes more common place, the need for reliable, efficient and interpretable structural connectivity measures and methods will grow. The goal of this work is to present a methodology for investigating the structural connectivity of an individual that meets these standards. The method strives to produce results with a clear physiological underpinning, an interpretation based on the basic assumption equating particle trajectories with underlying anatomical pathways and the incorporation of physical constraints that reflect both the physiology, as well as, the information content of the imaging modality.

Our approach requires the explicit determination of the proportion of connections with an end point in each node, a process based in the physiological expectations of connection symmetry and the conservation of connections. It is important to note that DW-MRI, and thus the structural connectivity methods based upon it, have no means to distinguish between afferent and efferent axonal fiber bundles. Thus the expectations of symmetry are not based on ideas of functional connectivity and directionality of information transfer, but are basic physical constraints. Thus, symmetry of connection strength implies that the number of fibers, both afferent and efferent, connecting nodes A and B, should be the same as that found connecting B to A. Similarly conservation of connections implies that the

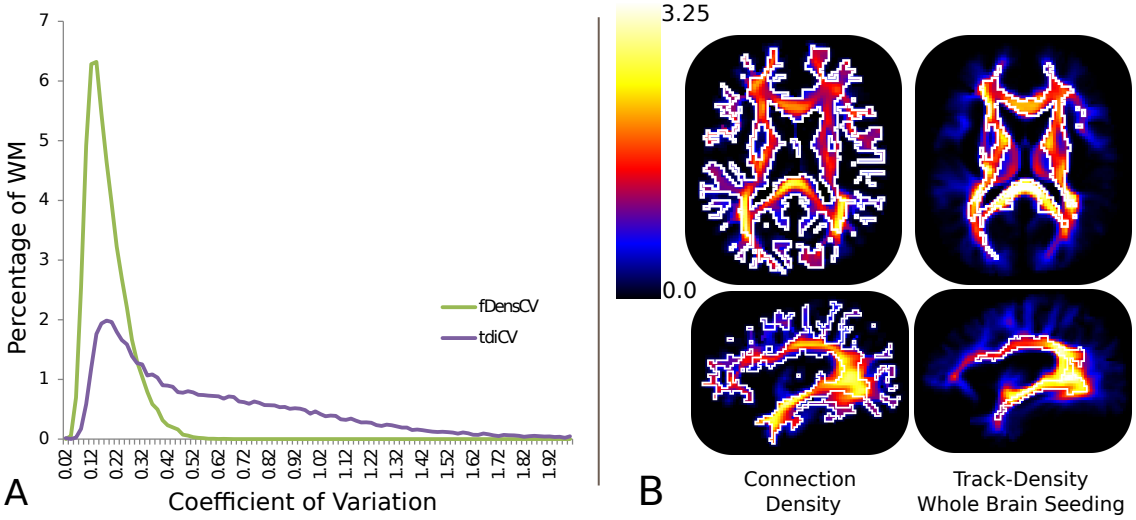

Figure 5.9: Population averaged track density images generated by seeding in the whole brain and connection density images are shown in **A**. Note that for visualization purposes each image was scaled by the number of connections passing through the mid sagittal corpus callosum prior to computing the average. These results indicate the more even contrast between the cortical and central WM pathways of our method.

number of fibers terminating in node A should be equal to the number modeled exiting it.

For each subject, the method produces three features related to the structural connectivity: 1) The *structural connectivity matrix*, describing the proportion of connections between pairs of nodes, 2) The *nodal connection distribution*, describing the proportion of connections that terminate in each node and 3) the *connection density image*, which describes density of connections as they traverse through the WM. These features demonstrate a high degree of reproducibility of their respective components, connectivity weights, GM nodes and WM voxels. This is evident by high (> 0.75) correlation coefficients and low ($< 5\%$) percent error, seen in Figure 5.3. Additionally, for each of these three measures, the difference between the same subject at two time points (Within) is roughly a quarter of the difference between different subjects (Between) at the same time point, indicating that these measures are specific to the individual. The population averages of these differences can be seen in Figure 5.4. When taken in concert these indicate measures that are both highly reliable and sensitive; thus are well suited to exploring population differences due to pathology.

The population average connectivity matrix, downsampled to the anatomical nodes (Figure 5.5), displays the expected bilateral symmetry and is qualitatively similar to those found in the literature [64, 193]. It is dominated by the diagonal elements, suggesting a high rate of short range self connections, when nodes are defined anatomically. At the higher resolution node parcellation, clear sub-circuits (Figure 5.5-B) are visible, which are unavailable with the more typical anatomical nodes. For instance, the connections between the lateral occipital cortex (LatOcc) and the fusiform gyrus stem form a clearly defined subnetwork, highlighted in blue.

The ability to efficiently measure structural connectivity, with a high spatial resolution, offers a number of intriguing avenues of future research. Such high resolution connectivity profiles may prove useful in providing contrasts to cortical registration algorithms that currently only utilize geometric features of the WM/GM boundary to drive the registration process. Similarly, they may enable improving cortical parcellations, providing better understanding of the structural/functional relationships between different regions and yielding more informative cortical atlases. This increase in spatial resolution does come at the expense of increasing the dimensionality of the connectivity matrix, causing statistical challenges when testing for group differences. However sophisticated dimensionality reduction techniques, such as manifold learning or sparse matrix decomposition, may be used to mitigate the loss of statistical power.

The nCD describes the proportion of connections that terminate in each node relative to the total number of connections in the connectivity network. Conceptually, it is similar to the nodal weighted degree or nodal strength that has been used in other network analysis [141]. The difference stems from the role that the nCD plays in determining the structural connectivity. As opposed to the nodal strength which is computed from the structural connectivity matrix and is thus a feature of the network, the nCD is explicitly computed from the conditional probability matrix and plays a key role in imparting the framework on a whole with its physiological interpretation. The population average nCD, seen in Figure 5.6-A, displays a general bilateral symmetry that would be expected from a measure of

anatomy. Variation in the nCD is visible with bilateral increases in regions of the superior temporal lobe. While an explicit verification of the spatial pattern is not possible here, the population histogram (Figure 5.6-B) of the coefficients of variation of the nodes indicates that it is relatively well preserved throughout the population. Additionally, this spatial contrast in connections lends credence to the idea that there exists topographical variability in the GM cytoarchitecture, such as the density of mini-columns [34], which may affect the connectivity of various regions, suggesting that the nodal connection distribution may prove useful in localizing group differences or serving as a feature used to improve GM parcellation schemes.

Finally, the connection density images provide a means to investigate and localize structural connectivity differences within WM volume, possibly enabling the identification of focal WM differences that may affect connections between a broad range of nodes. Figure 5.7 shows the connection densities of the mid-sagittal slice of the CC. The majority of the CC connections pass through the splenium and the genu, with a lower number in the mid-body. This spatial pattern has been seen in existing studies of CC which make use of histological fiber counting techniques to quantify the number of connections, as can be seen by comparing this result to figure 5 of [84] or Figure 1 of [1].

When investigating the connection density in the whole of the WM, we see that the proposed method has low CV values, indicative of low population variance. The CV histograms of the connection density and TDI-wholebrain images, seen in Figure 5.9-A, indicate that the connection density histogram is more concentrated in the lower ranges ($CV < 0.5$) indicating a tighter spread in the connection density values across the population than in either of the TDI approaches. Images of the population average TDI-WholeBrain and connection density image, 5.9-B, illustrate that the TDI-WholeBrain images yield higher connection density in central WM pathways than in the cortical WM, whereas the contrast in the connection density image is much more balanced. This emphasizes both the central pathways as well as the association or U fibers located in the cortical WM regions. It should be noted that the track density images presented here were generated using the tractography algorithm of

MRtrix. Other tractography algorithms [49, 109] could be utilized and may give different results.

It is important to note that without ground truth it is difficult to quantitatively validate these or any method that attempts to quantify structural connectivity. The qualitative findings are, however, encouraging and indicate that testable hypothesis could be garnered from the spatial patterns of nCD (Figure 5.6-A), as well as from the connection density images (Figure 5.9-B). One of the many strengths of this work is the presentation of an integrated structural connectivity framework, where connection density images and connectivity matrices are products of a single methodology. Thus future corroborating evidence, validating aspects of the methodology, such as the spatial patterns evident in the nCD or the connection density images, would lend support to the framework as a whole. A fact that is particularly important, considering the difficulty in validating whole brain structural connectivity matrices. The results of the test/retest reliability, as well as, the consistency of the results within the population, indicates the potential of the framework in elucidating group differences and in providing a unique means of identifying structurally homogenous GM regions.

By providing a representation of the physical connections between GM regions, structural connectivity networks provide a scaffold on which functional signals derived from fMRI or magnetoencephalography can be understood. The use of a single cohesive framework improves the ability of researchers to distinguish between different causes of connectivity deficits, such as focal changes in the underlying WM architecture (accessible by the connection density images) or by changes in the nodal connection patterns (obtained via an examination of the nodal connection distribution and connectivity networks). The ability of the framework to efficiently work with large networks, allows for higher spatial sensitivity, enabling finer node parcellations and a more detailed view of connectivity in the human brain.

CHAPTER 6 : Applications

6.1. Introduction

The methodological development of the last three chapters was motivated by the need for HARDI analysis methods that could be used within a clinical context to elucidate group differences.

The spatial normalization method plays a central role in all of the statistical analysis that are performed. The alignment of each subject's anatomy into a common template reference frame permits the investigation of HARDI based scalar measures at the individual voxel level. It also enables the computation of a population averaged HARDI data model that can be used by the WM parcellation algorithm to determine regions of homogeneous WM architecture, thereby facilitating regional statistics. Together these approaches allow the investigation of the local WM tissue architecture, at either voxel or regional level, as measured by the more complex HARDI data models. An additional analysis approach, enabled by these methods, is the statistical investigation of structural connectivity networks. Topological properties computed from these network models, in addition to the specific connections, can be examined to identify differences, at the global and network level, between the clinical populations under study.

In this chapter, we apply these analysis paradigms to the investigation of two pathologies thought to possess aberrant connectivity, schizophrenia (SCZ) and the autism spectrum disorders (ASDs). This is done with two aims in mind. First, how do the FOD-based scalars compare with the more traditional DTI-based scalars for the task of differentiating the groups under study? Secondly, and more critically, are our methods, specifically the connectivity framework, able to illustrate group differences in systems thought to be affected by pathology?

It should be stressed that both of these studies are exploratory in nature, meant to illustrate the ability of our methods to extract meaningful information from the WM. Population

studies striving to achieve true statistical group differences must typically be hypothesis driven to account for the small sample sizes available from imaging studies. The work here is meant to illustrate the breadth of problems addressable using our methodologies, as opposed to focusing specifically on areas of interest to each pathology.

6.2. Analysis Framework

The goal of both studies is the identification of population level differences in WM organization. This is facilitated through two analyses paradigms. The first strives to identify differences in the local WM architecture, while the second, utilizes network models of brain connectivity to identify differences in structural connectivity patterns and topology. Each of these approaches is described below, as is the model fitting procedure that serves as the starting point for both paradigms.

6.2.1. Imaging Datasets

The imaging dataset used in the SCZ study consists of a 64 direction, $b = 1000\,\mathrm{s/mm^2}$, DW-MRI acquisition acquired on 66 patients (37 Males/29 Females) diagnosed with SCZ as well 66 (37 Males/29 Females) age-matched control subjects. While the low b-value is not ideal for HARDI modeling, this approach provides a unique ability to compare and contrast the ability of each model for identify group differences *in-vivo*.

The ASD dataset consists of two DW-MRI acquisitions acquired on 39 subjects diagnosed with ASD (30 Males/9 Females) as well as 27 (14 Males/13 Females) age-matched typically developing children (TDC). The first acquisition, an optimized 30 direction, $b = 1000\,\mathrm{s/mm^2}$, DTI acquisition was acquired enabling the computation of DTI images for each subject. The second was a 64 direction, $b = 3000\,\mathrm{s/mm^2}$ acquisition, facilitating the computation of the FOD in a more optimal setting. Structural MP-RAGE acquisitions were also performed on each subject, in both studies, facilitating tissue segmentation. Please see Sections A.1.1 and A.1.2 for complete descriptions of the two datasets.

6.2.2. Model Fitting & Registration

Images from each subject underwent the preprocessing and model fitting procedures, discussed in Section A.2. Briefly, this process consisted of Rician and eddy current correction performed on each DWI dataset, followed by DT and FOD model fitting. In the case of the SCZ dataset both models were fit to the $b = 1000\,\mathrm{s/mm^2}$ set of DWIs, whereas in the ASD study, the FOD was fit to the set of $b = 3000\,\mathrm{s/mm^2}$ DWIs. Structural images were first corrected for field inhomogeneity and segmented into WM, GM and CSF. The resulting images were rigidly registered to the FOD space, yielding co-registered, DT, FOD image and tissue segmentation images for each subject.

A single subject from each study was chosen to act as that study's template. A 37 year old male subject was chosen to act the registration template for the SCZ study and a 10 year old male was chosen for the ASD study. The FOD-Demons registration method described in Chapter 3 was used to align the FOD images of both populations while the DTI-DROID [88] registration algorithm was used to align the DT images.

6.2.3. Regional WM Architecture

From the registered DTI and FOD images of each subject, a number of scalar measures can be computed and used to represent the local WM architecture at each location. From the FOD images, we compute the spectral power of each of the five orders (l levels) of the RSH expansion of the FOD, using equation B.3, yielding five scalar images, P0, P2, P4, P6 and P8, corresponding to the even RSH orders. Additionally the generalized fractional anisotropy (GFA) [172] of the FOD at each voxel, x, is computed as:

$$GFA(x) = \frac{std(f)}{rms(f)} = \sqrt{\frac{n\sum_{i=1}^{n}(f(\mathbf{u_i}) - \bar{f})^2}{(n-1)\sum_{i=1}^{n} f(\mathbf{u_i})^2}} \tag{6.1}$$

where $\{\mathbf{u_i}\}$ are a set of $(n = 1000)$ sampling directions, $f(\mathbf{u_i})$ and $\bar{f}$, are the FOD values in the $\mathbf{u_i}^{\text{th}}$ direction and the average value of f. This yields six scalar images computed from each subject's FOD images.

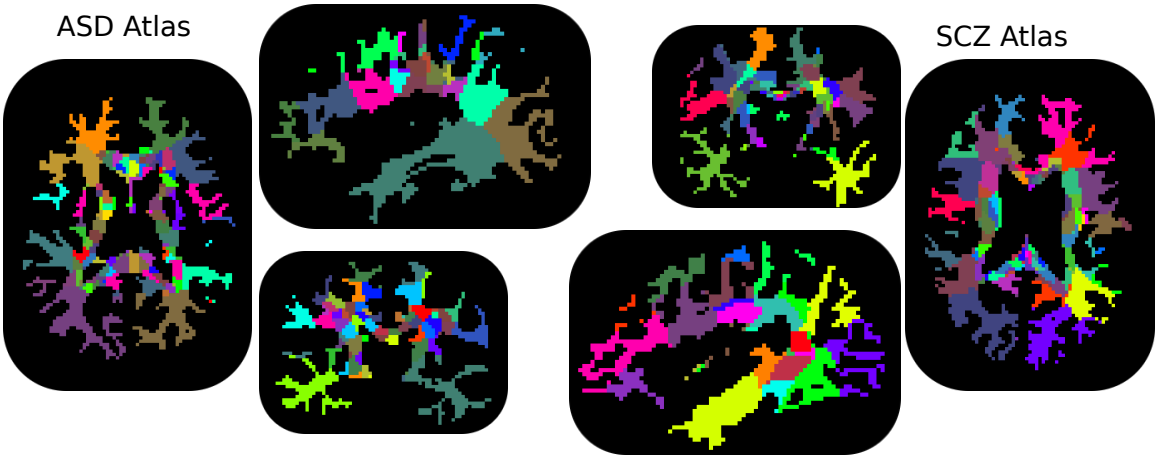

Figure 6.1: Population atlases generated from the control populations of the ASD and SCZ studies. Different parameters were used to compute the voxel similarities (equation 4.2) to control for difference characteristics of the population averaged FOD images. The ASD atlas was generated using $\sigma_f = 0.08$ and $\sigma_s = 6\,\text{mm}$, while the SCZ atlas used $\sigma_f = 0.12$ and $\sigma_s = 6\,\text{mm}$.

To serve as a comparison, two common DTI-based scalars were also computed:

$$FA(x) = \sqrt{\frac{3}{2}\frac{(\lambda_1 - \bar{\lambda})^2 + (\lambda_2 - \bar{\lambda})^2 + (\lambda_3 - \bar{\lambda})^2}{\lambda_1^2 + \lambda_2^2 + \lambda_3^2}}$$

$$TR(x) = 3\,ADC(x) = 3\,\bar{\lambda} = \lambda_1 + \lambda_2 + \lambda_3$$

where λ_1, λ_2 and λ_3 are the eigenvalues of the DT at voxel x.

WM Atlas Generation

For both control populations, average FOD images were computed and parcellated using the method described in Chapter 4. The process generated two atlases, each consisting of 500 ROIs. The generation of both atlases used $\sigma_s = 6\,\text{mm}$ to control the spatial component of the similarity kernel (Equation 4.2). However different values of σ_f were chosen to account for the different characteristics, due to the difference in b-value, of the population average FOD images. The SCZ atlas used $\sigma_f = 0.12$, while the ASD atlas used $\sigma_f = 0.08$. Representative slices of each can be seen in Figure 6.1. For each ROI defined, regional averages of the above computed scalars were collected into a feature vector used to represent the particular

ROI. This process reduces the dimensionality of each subject's representation from 8 scalar images of roughly 80,000 voxels to 500 feature vectors, each vector representing a single ROI.

6.2.4. Structural Connectivity

Structural connectivity networks are computed by first defining, in the template space, the GM regions that will serve as network nodes. This was accomplished by segmenting each study's template structural image, into GM, WM, CSF, using Freesurfer [55] software package. This process also segments the cortical and sub-cortical GM into regions defined in the Desikan atlas [50]. Connectivity networks, using these 86 regions as nodes, were then generated using the methods developed in Chapter 5.

From these networks, five global scalars are computed[1] and used to capture the topological properties of the structural connectivity networks:

1. The characteristic path length is the average shortest path length between all pairs of nodes and is commonly used as a measure of network integration.

2. Global efficiency is defined as the average inverse shortest path length. Like the characteristic path length, global efficiency is a measure of network integration. It is, however, more heavily influenced by shorter paths than the characteristic path length which is heavily influenced by long paths.

3. Network Density is the ratio of number of present connections to possible connections and is a measure of the overall degree of connectivity in the network.

4. Modularity quantifies the degree to which the network can be subdivided into clearly delineated non-overlapping groups. This approach seeks to define modules that maximize the number of intra-module edges and minimize inter-module edges.

[1] Topological features are computed from their weighted undirected definitions, using the brain-connectivity- toolbox [141]

5. Transitivity is a simpler approach to quantitate the modularity of a network. It is based on the average number of triangles, occurring when a node's connected neighbors are also connected to one another.

6.2.5. Processing Summary

These two processing approaches allow the connectivity of each subject to be investigated at a number of levels. At the voxel and regional level, the WM architecture can be investigated using the five spectral powers of the FOD and the GFA. At a global or systems level, the network connectivity structure can be investigated based on the topological properties or on the basis of individual network connections.

6.3. Schizophrenia: Results and Discussion

Schizophrenia (SCZ) is a chronic and disabling psychiatric disorder affecting approximately 1.1% of the adult population[2]. While its precise etiology is unknown, there is growing evidence suggesting that it arises from abnormal connectivity in the brain [29, 58]. Network based analysis of SCZ, using both functional connectivity [107, 192] and networks derived from cortical thickness measurements [20], have illustrated the different topological properties of the schizophrenic brain. When viewed in conjunction with evidence from task based fMRI [69], these findings are clearly suggestive of a failure of functional integration in SCZ. Studies using DTI, see Section 2.4, have focused primarily on identifying local differences in WM. These finding have been somewhat varied, but the general picture is one of decreased local FA, in a number of WM areas.

The DW-MRI dataset used here to investigate schizophrenia, is a typical DTI acquisition, acquired with a low b-value by HARDI standards. While not ideal for HARDI modeling, it does provide a means to evaluate the role of modeling within this type of acquisition and the potential benefits that such modeling has over the more common DT modeling.

[2]Source: National Institute for Mental Health

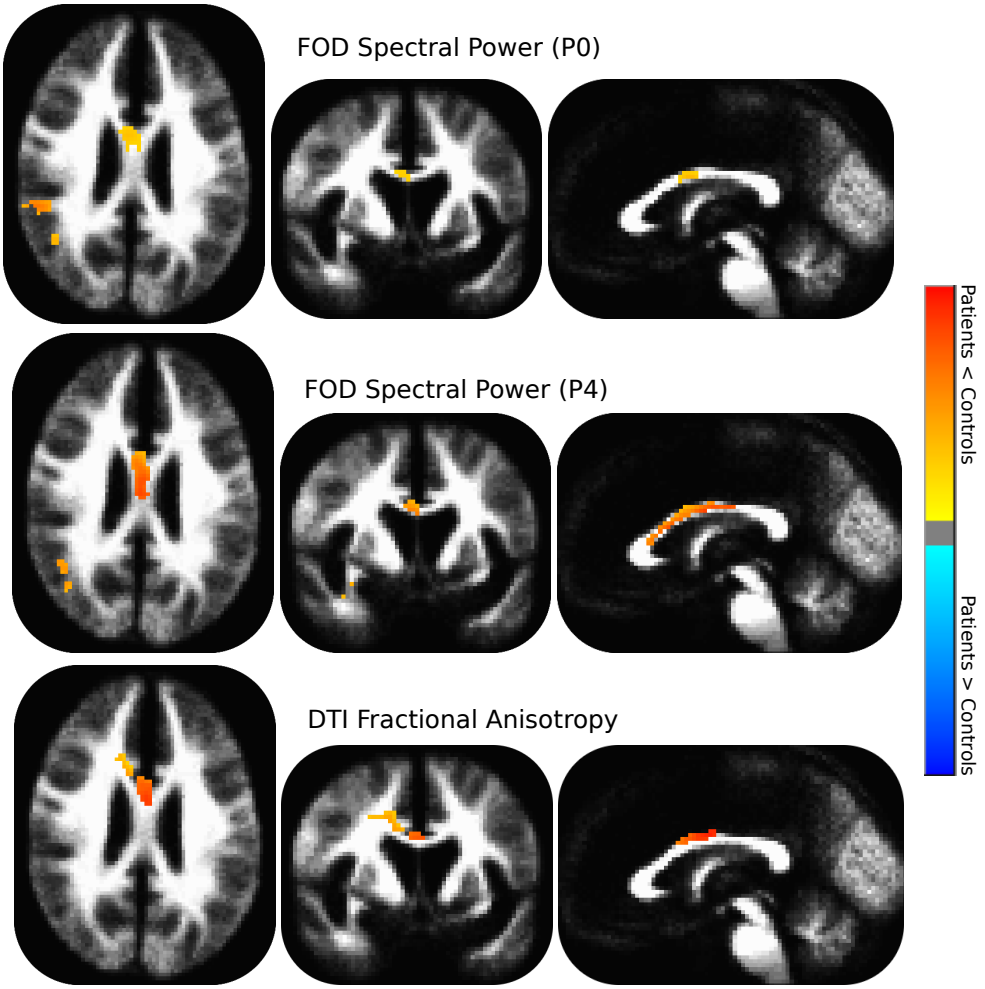

Figure 6.2: Representative slices of thresholded ($p < 0.01$, cluster size > 50 voxels) statistical maps indicating areas of difference between male schizophrenic patients and age matched controls. The three DW-MRI scalars are largely in agreement, with the most prominent difference being observed in the Corpus Callosum. The FOD spectral powers indicate a larger affected area of the CC, than FA.

6.3.1. Statistical Analysis

In order to account for the established role that gender [105] plays in the presentation of SCZ, the dataset was divided in two, based on gender. Thus males and females were investigated independently. Each of the scalar maps, FA, TR, GFA and the RSH powers (P0, P2, P4, P6, P8) were computed and spatially smoothed, using a Gaussian kernel with a full width half max (FWHM) of 4mm. Voxels outside of the WM, as determined by the

template's WM mask, were not included in the smoothing kernel, ensuring that only WM voxels contributed to each smoothed scalar image. Voxel-wise t-tests were then performed on each smoothed scalar image using the Afni [44] software package. Representative slices of these t-tests can be seen in Figures 6.2 and 6.3, for the male and female populations respectively. In the male population, patients were found to have diminished FOD spectral powers and FA in the anterior aspects of the CC midbody. Differences in GFA and TR failed to survive thresholding ($p < 0.01$, cluster size greater than 50 voxels). Interestingly, the areas of difference in the female population were focused in an area of complex WM, the superior longitudinal fasciculus (SLF). Patients had lowered P0 and P4 spectral powers and higher TR values in this region. The other spectral powers show similar spatial patters to P4 but with lower significance. Findings in GFA and FA did not survive thresholding.

Regional features were extracted from registered DTIs (FA and TR) and FOD images (P0 and P2) from each subject. A multivariate Hotelling T^2 statistical test was then performed on each ROI to indicate regions of group difference. Images of these t-scores are shown in Figure 6.4. In males, both the DTI and FOD statistics indicate abnormalities in the frontal and temporal WM, with the differences being more significant when using the DTI measures. In females, the spatial pattern of FOD differences shift away from the frontal WM, and become greatly reduced when using the DTI measures.

Analysis of structural connectivity was performed at two levels. T-matrices were determined for each group (males and females), using a two sided t-test at each edge of the connectivity network. These matrices were then thresholded at T=2.5 ($p < 0.01$) to indicate the individual connections, between the 86 nodal regions, that display a group difference. They can similarly be colored to indicate the magnitude of group difference between the populations. Figure 6.5 displays the average connectivity matrix for each group, in addition to maps indicating the nodes higher in controls than in patients and vice versa. Connections displaying the largest group difference, indicated in red in Figure 6.5 are listed in Table 6.1. Topological properties were similarly tested for group difference. Of the five global network properties, two (density and global efficiency) were found to be significantly higher ($p < 0.05$) in male

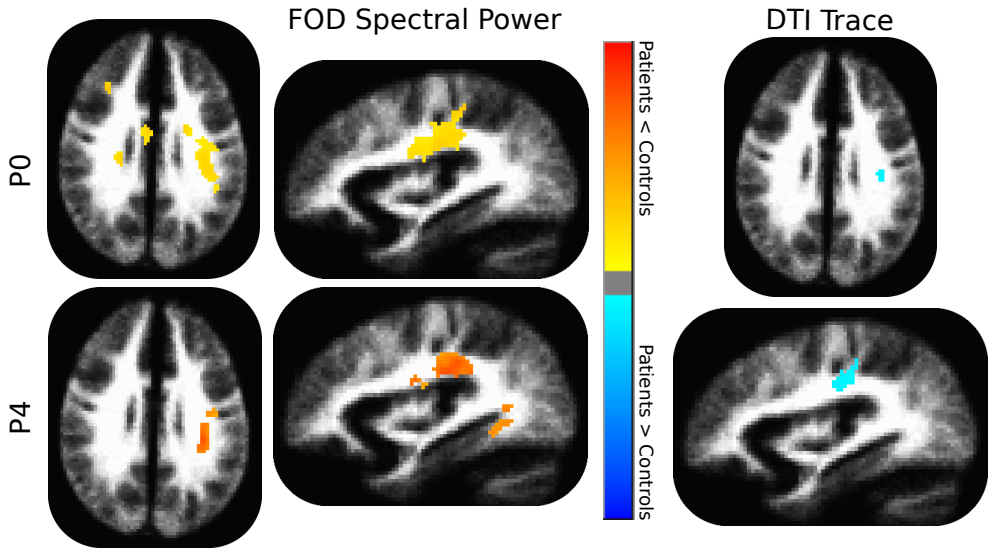

Figure 6.3: Representative slices of thresholded ($p < 0.01$, cluster size > 50 voxels) statistical maps indicating areas of difference between female schizophrenic patients and age matched controls. FOD spectral powers (orders 0 and 4) indicate a large portion of the SLF is affected in females. The mean diffusivity, as measured by DTI, is seen to increase in a portion of this area.

patients and only transitivity was significantly lower in male patients. Similar trends were found in the female topological properties, but failed to reach significance.

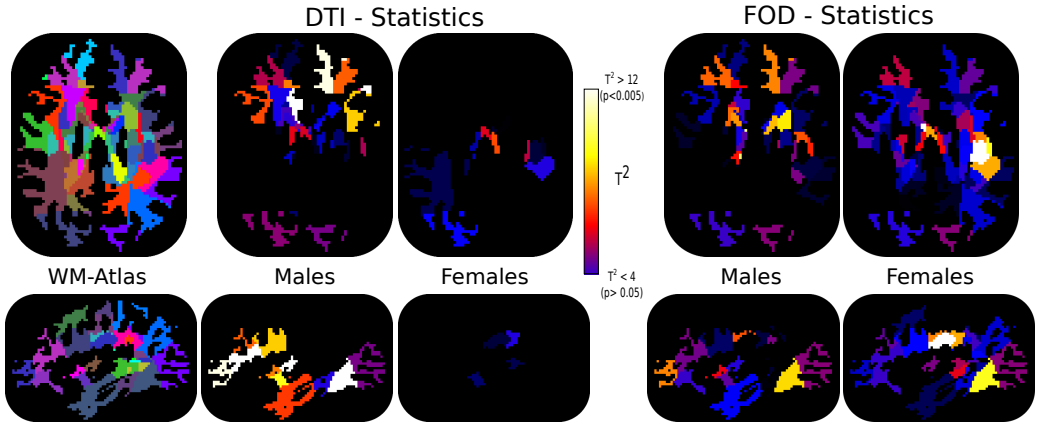

Figure 6.4: Hotelling T^2 tests were performed on each ROI defined in the WM atlas. For the DTI image, MD and FA were used as features, while the 0th and 2nd order spectral powers were used as features of the FOD images. Both the DTI and FOD based approaches indicate group differences in the Frontal WM in males. However, only the FOD based statistics indicate group differences in females.

Males

Node 1		Node 2		
Lobe	Area	Lobe	Area	Difference
R Temporal	Superior Temporal	R Subcortical	Caudate	Cnts>Pats
R Temporal	Transverse Temporal	R Subcortical	Thalamus	Cnts>Pats
R Temporal	Insula	R Subcortical	Accumbens	Cnts>Pats
R Temporal	Bankssts	R Subcortical	Thalamus	Cnts>Pats
R Temporal	Superior Temporal	R Subcortical	Thalamus	Cnts>Pats
R Temporal	Insula	R Frontal	Pars Triangularis	Cnts>Pats
R Frontal	Lateral Orbito Frontal	R Subcortical	Accumbens	Cnts>Pats
R Frontal	Pars Triangularis	R Frontal	Rost Mid Frontal	Cnts>Pats
R Subcortical	Caudate	R Subcortical	Putamen	Cnts>Pats
L Parietal	Posterior Cingulate	R Frontal	Superior Frontal	Cnts>Pats
L Frontal	Superior Frontal	R Frontal	Anterior Cingulate	Cnts>Pats
L Temporal	Inferior Temporal	L Parietal	Sup. Parietal	Pats>Cnts
R Temporal	Isthmus Cingulate	R Temporal	Parahippocampal	Pats>Cnts
R Temporal	Fusiform	R Parietal	Precuneus	Pats>Cnts
R Parietal	Precuneus	R Subcortical	VentralDC	Pats>Cnts
R Frontal	Pars Opercularis	R Frontal	Pars Orbitalis	Pats>Cnts

Females

R Temporal	Fusiform	R Subcortical	Amygdala	Cnts>Pats
L Temporal	Fusiform	L Subcortical	Amygdala	Cnts>Pats
L Temporal	Middle Temporal	L Temporal	Trans. Temporal	Cnts>Pats
L Frontal	Rostral Middle Frontal	R Frontal	Lat. Orb. Frontal	Cnts>Pats
L Subcortical	Thalamus	L Subcortical	Putamen	Cnts<Pats
L Frontal	Lateral Orbito Frontal	L Subcortical	Caudate	Cnts>Pats
L Subcortical	Thalamus	L Subcortical	Pallidum	Cnts>Pats
R Frontal	Pars Opercularis	R Frontal	Superior Frontal	Pats>Cnts
R Frontal	Pars Opercularis	R Frontal	Pars Triangularis	Pats>Cnts
R Frontal	Medial Orbito Frontal	R Frontal	Superior Frontal	Pats>Cnts
R Frontal	Pars Opercularis	R Parietal	Post. Cingulate	Pats>Cnts
R Temporal	Entorhinal	R Subcortical	Hippocampus	Pats>Cnts
R Temporal	Inferior Temporal	R Parietal	Precuneus	Pats>Cnts
L Parietal	Supramarginal	L Subcortical	VentralDC	Pats>Cnts
L Parietal	Supramarginal	L Subcortica	Hippocampus	Pats>Cnts
L Occipital	Lingual	L Parietal	Superior Parietal	Pats>Cnts

Table 6.1: Structural connections showing group differences in SCZ. Represented as red lines in Figure 6.5.

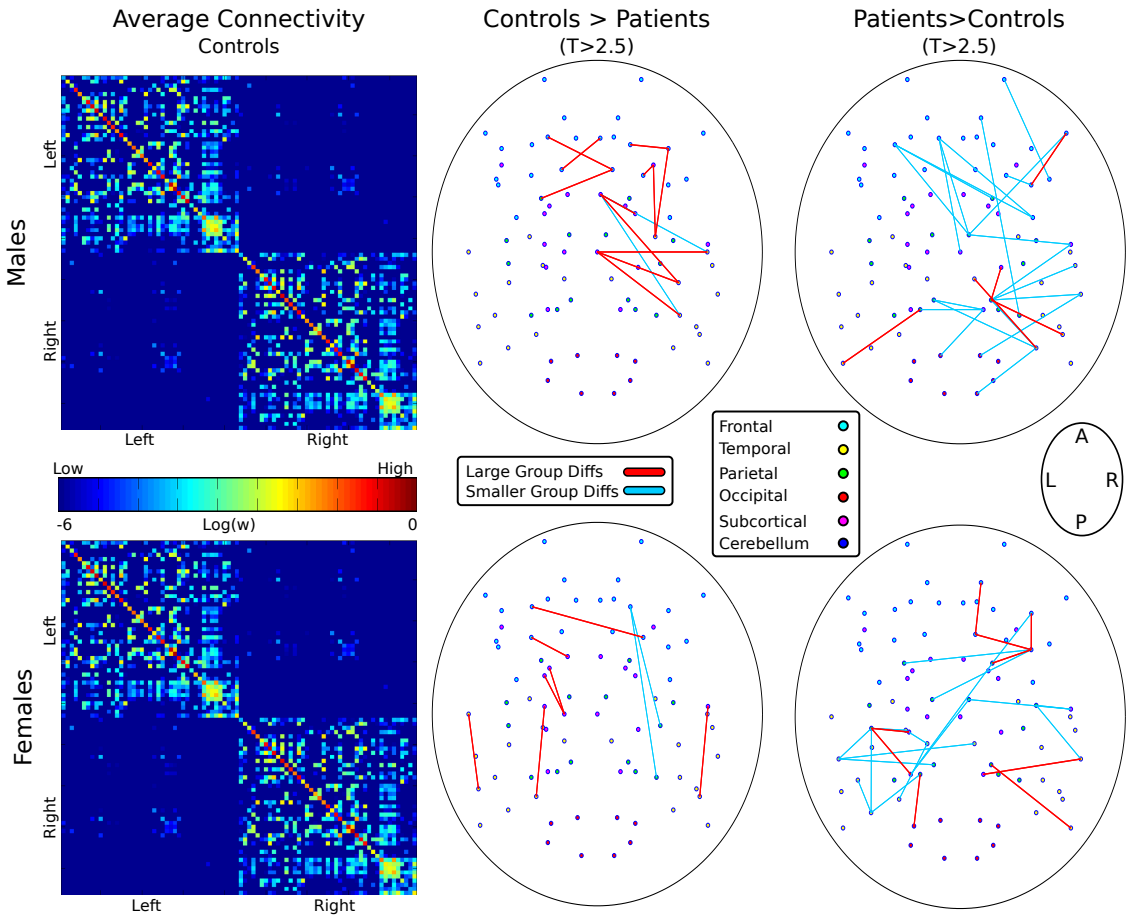

Figure 6.5: Statistics were performed on each network connection using a student's t-test. Edges with T-score magnitudes above 2.5 are shown separately for both males and females and for two cases: Controls having higher connections than patients and vice-versa. Connections are colored by the difference between the two groups, with blue connections being lower, by two orders of magnitude, than the largest group connection difference. A Table of the red connections can be found in Table 6.1.

6.3.2. Discussion

One of the prominent hypotheses in SCZ research revolves around its characterization as a connectivity disorder. The findings presented here clearly support the existence of altered structural connectivity in schizophrenic subjects. In males, this manifests as decreases in FA and in the spectral powers of the FOD, in the CC and the frontal/temporal WM. The FOD spectral powers indicate a slightly larger affected region of the CC than is found in FA. These local effects manifest in the global connectivity analysis in a number of ways. The

connections that are lower in patients tended to involve stronger connections and to occur between regions that are thought to be affected by schizophrenia. These areas include the Thalamus [30, 147], the Caudate [156], the Insular cortex [62, 127] and the Cingulate [56]. Interpretation of the increased patient connection strengths of certain connections is more difficult, but supports the premise of dysconnectivity [29, 58, 160], as opposed to purely diminished connectivity, in schizophrenia.

Perhaps the most striking facet of these results is the effect of gender on the patterns of group difference. The principal area of difference between female patients and controls was found in the left SLF. This difference is robustly shown by the spectral powers and to a certain extent in the TR. When using the DTI-based regional statistics very little difference was observed between the groups. The regional FOD statistics (Figure 6.4) indicate similar frontal WM patterns to those seen in males, but display a strong group difference in the left SLF regions.

The growing consensus, supported by this study, is that the integration of the various functional units making up the human brain, is altered in schizophrenia. Our findings suggest that while there are deficiencies in the structural connectivity of particular areas, there are also connections that are strengthened. In both genders, although more strongly in males, we see increases in global connection density and decreases in transitivity, implying a more connected but less organized connectivity pattern in schizophrenia. Moving forward, the joint analysis of functional and structural connectivity may offer significant insights into the role altered structural connectivity has on functional connectivity perhaps signaling areas where functional deficiencies are due to local differences in synaptic plasticity [58, 160] as opposed to anatomical (axonal) connectivity differences.

6.4. Autism: Results and Discussion

The autism spectrum disorders (ASDs) are a set of complex, heterogeneous neurodevelopmental disorders. They are defined by clinical assessment in three core domains: social

interaction, communication or language use and restricted or repetitive behaviors and interests. Deficits in all three domains are required for a classical autism diagnosis, whereas individuals diagnosed on the spectrum, reflect varying degrees of the abnormalities in each of the three domains.

Structural MRI studies have identified altered brain growth trajectories [43] in subjects diagnosed with ASD. This altered developmental trajectory, characterized by an early rapid overgrowth in total volume followed by a plateau and possible decline to normal volumes, is not uniform across all parts of the anatomy. The most consistent findings indicate volumetric changes in the frontal and temporal lobes [28, 77] with a particular increase in the cortical WM volume of the frontal lobe. These areas have also been implicated in recent DTI studies [6, 104, 161]. Functional connectivity [93, 171, 187] studies have indicated decreases in long range connectivity and increases in short range connectivity commensurate with the hypotheses of overgrowth in short range cortical fiber pathways. The culmination of this evidence has led to an understanding of the ASDs as connectivity disorders, characterized by particularly aberrant connectivity patterns involving the frontal and temporal lobes.

This study focuses on the ability of our HARDI tools to elucidate these connectivity differences. A high b-value ($3000\,\mathrm{s/mm^2}$) DW-MRI acquisition was used to provide optimal data for the FOD modeling. Traditional DTI acquisitions ($b = 1000\,\mathrm{s/mm^2}$) were also performed, providing a comparison of our methods with the DTI techniques that are currently being utilized in clinical research studies.

6.4.1. Statistical Analysis

Statistical analysis proceeded along similar lines to those used in the SCZ study. The principal difference is the inclusion of age as a cofactor in our statistical analysis of ASD. While the ASD and TDC groups are age matched, both groups encompass a wide age range (6-16 years). Early adolescence is a time of rapid development, thus the inclusion of age as a co-factor was deemed prudent. Analysis of each scalar map, FA, TR, GFA and the RSH powers (P0, P2, P4, P6, P8), was performed by first smoothing each using 4mm FWHM

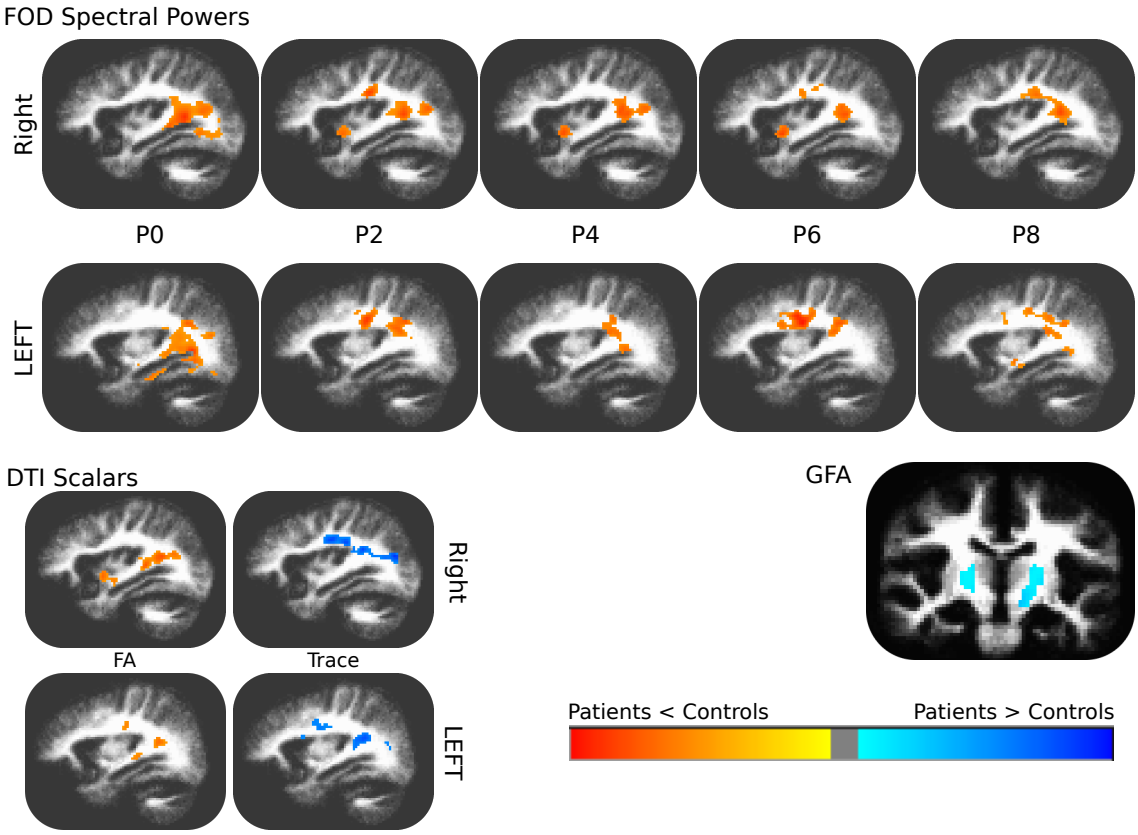

Figure 6.6: Representative slices of thresholded ($p < 0.01$, cluster size > 50 voxels) statistical maps indicating areas of difference between subjects diagnosed with ASD and typically developing controls. The HARDI based scalars, specifically P0, capture differences in sagittal stratum of the temporal lobe.

Gaussian kernel. The template WM mask was used to ensure only WM voxels contributed to the resulting images. These images were then analyzed using multiple linear regression to determine the diagnoses effect independently from the effect of age. Bilateral decreases, see Figure 6.6, in ASD were observed in the FA, TR and the RSH powers of SS and parts of the SLF. Differences in WM architecture of the posterior internal capsule was found using GFA, but were not observed in the other scalars.

Analysis of the global topological features computed from the structural connectivity matrices showed no significant difference when corrected for age. Each connection of the structural connectivity networks were analyzed using an analysis of covariance[3]. These were

[3]Analysis of covariance was performed using the Mancovan Matlab toolbox [5]

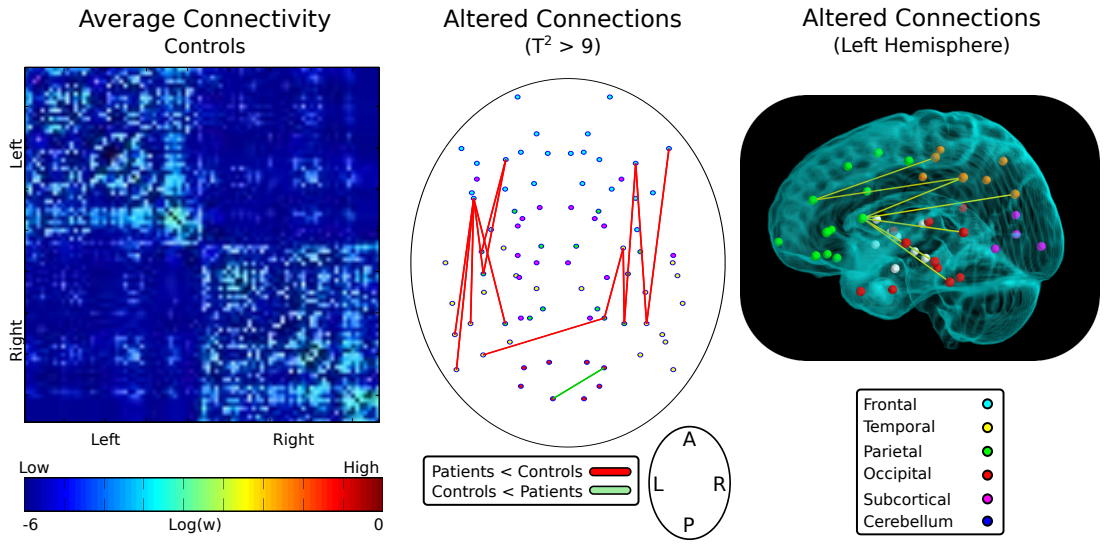

Figure 6.7: Statistics were performed on each network connection. Edges with T^2-scores above 3 are shown. Red lines indicate connections where patients have a decreased connectivity weight, while green indicates the reverse. A 3D rendering illustrates the connections between the frontal and temporal and parietal lobes. A table of these connections can be found in Table 6.2.

collected into a T^2-matrix, thresholded at $T^2 > 9.0$ to indicate the individual connections that display a prominent group difference. Figure 6.7 displays the average connectivity matrix for the control group, as well as network representations of connections indicating a group difference. Table 6.2 lists the connections with T^2 values above 9.

6.4.2. Discussion

The diverse behavior and cognitive symptomatologies associated with the ASDs, likely indicate a heterogeneous patient population, with perhaps a number of different etiologies. Despite this, the role of abnormal frontal and temporal connectivity is becoming more prominent [34, 42, 43]. The voxel-wise statistics, seen in Figure 6.6, indicate clear decreases in the FOD spectral powers of the SS region of the temporal lobe and in aspects of the SLF. These differences co-localize with decreases in the FA of the SS and with increases in trace of the SS and SLF, in agreement with reported [6, 123] increases in the mean diffusivity (1/3 of the trace) of the SLF.

Node 1		Node 2		
Lobe	Area	Lobe	Area	Difference
R Frontal	Pars Orbitalis	R Temporal	Bankssts	Cnt > Pat
R Frontal	Pars Triangularis	R Temporal	Bankssts	Cnt > Pat
R Frontal	Pars Triangularis	R Parietal	Inferior Parietal	Cnt > Pat
R Temporal	Insula	R Parietal	Inferior Parietal	Cnt > Pat
R Temporal	Insula	R Parietal	Superior Parietal	Cnt > Pat
L Frontal	Pars Opercularis	L Temporal	Inferior Temporal	Cnt > Pat
L Frontal	Pars Opercularis	L Temporal	Middle Temporal	Cnt > Pat
L Frontal	Pars Opercularis	L Temporal	Bankssts	Cnt > Pat
L Frontal	Pars Opercularis	L Parietal	Inferior Parietal	Cnt > Pat
L Frontal	Pars Opercularis	L Parietal	Supra Marginal	Cnt > Pat
L Frontal	Rostral Middle Frontal	L Parietal	Supra Marginal	Cnt > Pat
L Frontal	Rostral Middle Frontal	L Parietal	Post Central	Cnt > Pat
L Temporal	Parahippocampal	R Parietal	Superior Parietal	Cnt > Pat
L Occipital	Pericalcarine	R Occipital	Lingual	Pat > Cnt

Table 6.2: Structural Connections showing group differences in ASD. Of particular interest are the nodes comprising the language areas, the Pars Opercularis and Pars Triangularis (Broca's area) and the posterior banks of the superior temporal sulcus (Bankssts), where Wernicke's area is located.

As a number of the major temporal WM tracks, IFOF, ILF and the inferior aspects of SLF, pass through SS, local WM deficiencies there would have implications for much of the connectivity of the temporal lobe. The results of our structural connectivity analysis (Figure 6.7 and Table 6.2) indicate that 60% of the connections shown to be lower in ASD involve the temporal lobe. Of particular interest are those connections involving the language regions of the brain, as communication/language use is one of the core domains affected in ASD. Our findings indicate lower connectivity strengths between the orbital part of inferior frontal gyrus (containing the Pars Opercularis, Pars Triangularis and Pars Orbitalis) to the temporal lobe, particularly the posterior banks of the superior temporal sulcus (Bankssts) in both the right and left hemisphere. This suggests that even in this population, which did not present as specifically language impaired, the language pathways are affected in ASD. As this is an ongoing multi-modality study, it will be interesting to see how the functional modalities, specifically those focused on language processing [139, 146], correlate with these differences in structural connectivity.

6.5. Conclusion

The goal of this chapter was to illustrate the application of our HARDI analysis framework to the study of a clinical population. These preliminary studies illustrate that the proposed methodologies are able to identify differences in WM architecture beyond what is currently available using DTI-based approaches. In male SCZ subjects and in ASD subjects the HARDI-based scalars identified larger affected regions than those found using either of the DTI scalars investigated. Whereas in female SCZ subjects, the HARDI measures were able to distinguish differences in complex regions that the DT model did not capture.

From examining the voxel statistics in both studies, Figures 6.2, 6.3 and 6.6, it is clear the RSH powers of the FOD are not simply better versions of FA or trace, but are sensitive to different aspects of the WM architecture. The 0^{th} order spectral power (P0) is the integral of the FOD over all directions, suggesting that decreases in P0 could be due to decreases in local fiber density. As discussed in Section B.3, higher order powers are required to represent both complex fiber configurations, as well as, sharp focused peaks. This makes their physiological interpretation difficult, although, we suspect that as with other scalar measures of diffusion their interpretation will develop as their utilization increases.

Clearly, these studies demonstrate the ability of our tools to find group differences in biologically meaningful regions and systems. In SCZ, we show connectivity deficits in known systems, such as the cortical-thalamic connections [108, 134], but also increases in connectivity in regions less well understood in SCZ. Further investigation of these connections via functional connectivity is certainly warranted. Similarly, the analysis of structural connectivity in ASD indicated deficiencies between the frontal, temporal and parietal lobes as well as deficiencies in connectivity between prominent language areas, fitting closely to the current understanding of ASD pathology.

CHAPTER 7 : Conclusion

The utilization of neuroimaging to study neuropsychiatric disorders is a difficult undertaking. These disorders typically do not present as clear focal abnormalities, such as tumors or WM lesions, but instead are often characterized by subtle and diffuse differences through out the brain. The hope is that by identifying intermediate imaging-based phenotypes, ostensibly due to degenerative and/or altered developmental mechanisms, researchers will gain valuable insight into the mechanisms of the pathology while also highlighting the affected functional systems. Possible uses of these phenotypes include providing a quantitative measure that may correlate with behavior markers, aid in diagnosis [87, 100] or may be useful in predicting the effectiveness of various treatments.

Increasingly the role of structural and functional neural connectivity is being viewed as central to our understanding of the brain and the disorders that affect it. At present DW-MRI is the sole imaging modality able to investigate structural connectivity *in-vivo* and is now being routinely used, in the form of DTI, to investigate a wide range of neuropathologies. While the limitation of the DT diffusion model has spurned the development of a number of more complex HARDI models, little focus has been placed on the development of analysis methodologies utilizing this improved contrast which are required for population based group studies. Addressing this need has been the central focus of this thesis.

Three HARDI-based image analysis algorithms have been developed in this work, a spatial normalization algorithm, a WM parcellation algorithm and a method for quantifying structural connectivity. In Chapter 3 we described and validated our spatial normalization algorithm. This method makes use of the RSH coefficients of the diffusion model, the FOD in our case, to align each subjects' anatomy with that of a template. Simulation studies were performed to demonstrate the accuracy and efficiency of the proposed method. Similarly, the proposed approach was compared with state of the art DTI-based registration techniques, illustrating its ability to better align the WM anatomy, as indicated by

lower population variances, lower residuals and improved overlap of the population's WM volumes.

A data-driven WM parcellation algorithm was discussed in Chapter 4. This process uses local variations in an FOD image to delineate regions of homogeneous tissue architecture, facilitating the generation of population specific atlases. The data-driven nature of these atlases provide control of the granularity of the resulting ROIs, while maintaining lower regional variances compared with traditional anatomically defined ROIs. The HARDI-based structural connectivity methodology, presented in Chapter 5, utilizes efficient algorithms and physiologically inspired constraints to compute highly reliable network models of anatomical connectivity from the FOD images of each subject. These models are shown to be highly repeatable within the same subject while retaining that ability to discriminate between the connectivity patterns of different individuals, a critical trait for any measure to be used to differentiate clinical populations.

Individually each of these developments represent the state of the art in DW-MRI analysis methods, while together forming the core of a comprehensive HARDI analysis toolkit. Specifically, the development of these methods directly facilitates two analysis approaches for the investigation of WM pathologies. The first uses local features of WM integrity, derived directly from the HARDI diffusion models, to investigate regional differences in WM architecture. This requires spatial normalization to establish the spatial correspondence between the WM anatomy of each subject and WM parcellation to generate population specific atlases and facilitate regional statistics. The structural connectivity algorithm developed enables the second analysis approach, wherein population level differences are investigated at both the global level and at the individual connection level.

These analysis paradigms were applied to two disorders, schizophrenia and autism, demonstrating the ability of our methods to elucidate physiologically relevant group differences. In both studies the HARDI-based analysis of the local WM architecture was able to indicate levels of population difference above those found using current DTI-based approaches. Sim-

ilarly, our structural connectivity methods were able to demonstrate altered connectivity patterns within systems thought to be affected by pathology, suggesting that a component of the functional abnormalities in these systems may be due to aberrant axonal connectivity. It should be stressed that while these findings are intriguing additional studies are needed to replicate these findings.

Future Directions

The methodological development, contained in this thesis, presents a number of interesting avenues for further development. The most immediate path forward is the investigation of HARDI based scalar measures able to discriminate between normal and pathological WM tissue. It is clear from the voxel statistics presented in Chapter 6, that the RSH spectral powers possess discriminating power above those offered by DTI. However, their in depth study in relation to underlying tissue structure has not yet been fully explored. Other promising scalars [25, 61, 137] have focused on characterizing individual peaks within each voxel. The ability to extract peak related measures will offer a continuous representation of fiber integrity, allowing researchers to investigate how these measures vary as the fiber pathway passes though various architectures, such as fiber crossings etc. Such representations may offer a unique insight into the characterization of particular fiber bundles and how they are affected by pathology.

The clustering technique used to identify homogeneous WM regions offers a number of possible extensions. The proposed method relies on the FOD model to define the similarity between WM voxels. The extension of this definition to include additional information available from either structural connectivity or fiber tracking could feasibly increase the specificity of the determined ROIs. Such a similarity measure would better capture the role that each ROI plays in the global connectivity of the brain, providing the regions with additional anatomical meaning. One of the drawbacks of the clustering approach is that ROIs are generated from a population average or a template subject, requiring accurate registration to establish correspondence between subjects. An intriguing alternative is to

use registration and the proposed method to generate population level ROIs which are then mapped back into the subject space. The boundaries of the ROIs can then be adjusted to better match the individual boundaries of the subject's anatomy. In this way correspondence between ROIs would be maintained but the individual boundaries would be based on the specific subject.

The use of structural and functional network models to quantitatively investigate neuronal connectivity continues to grow. One critical area of these models that is just now beginning to garner attention, is the way that the GM nodal regions are defined. Most structural connectivity methods, including ours, rely on registration to establish correspondence between the anatomically defined nodal regions. Typically, registration is based on cortical features, such as sulcal and gyral patterns, or using volumetric registration, as is done here. Such approaches fail to account for the variability in size and location of functional regions [7, 199]. An alternative approach attempts to directly parcellate the cortex [38] into functionally coherent regions using functional or structural connectivity. The efficient nature of our structural connectivity method facilitates the computation of high spatial resolution structural connectivity networks allowing for the development of clustering methods, such as those utilized to parcellate the WM, to be applied to the cortex. Such methods would identify GM regions that have similar connectivity profiles, which could be construed as representing a functional unit.

The final area where research focus is needed, centers on the need to develop sophisticated statistical approaches able to efficiently analyze structural connectivity matrices. The increase in the spatial resolution of the GM nodal regions comes at the expense of increasing the dimensionality of the connectivity matrix, which causes statistical challenges when testing for group differences. While improved regional delineation, via methods like those discussed above, may somewhat ameliorate this issue, the development of sophisticated dimensionality reduction techniques, such as manifold learning or sparse matrix decomposition, will be needed to mitigate the loss of statistical power.

Summary

DW-MRI has emerged as a powerful tool enabling the quantitative analysis of neuronal WM and connectivity. The recent development of advanced diffusion modeling techniques allows for improved modeling fidelity in regions of complex WM, which is unavailable from the DT model used commonly today. To date these improved methods have mainly been utilized within individuals, a fact partially owing to the lack of analysis tools necessary for successful population-level analysis. This thesis presents a core set of tools, built around the HARDI diffusion models, that enables the use of these complex diffusion models within a clinical research setting. As MR acquisition techniques, such as compressed sensing, continue to lower the acquisition times for DW-MRI pulse sequences, the clinical use of these new models will increase, as will the utility and necessity of analysis methods such as those presented here.

APPENDIX A : Datasets and Common Preprocessing

This appendix describes the three datasets that were used to validate the methods presented in this thesis, as well as, the preprocessing and model fitting pipelines, that serve as the initial steps of the analysis framework.

A.1. Imaging Datasets

There are three datasets that are used throughout this thesis. The first focuses on investigating subjects diagnosed with an ASD, using a high b-value HARDI acquisition and low b-value DTI acquisition (Chapter 6). The TDCs, used as control subjects for this study, were also used to validate the registration and WM parcellation algorithms, presented in Chapters 3 and 4 respectively. The second dataset was used to evaluate the repeatability and sensitivity of the proposed structural connectivity framework, discussed in Chapter 5. Lastly, a low b-value dataset was acquired to investigate the utility of the proposed framework in subjects diagnosed with schizophrenia.

A.1.1. ASD Imaging Dataset

The ASD dataset consisted of 39 subjects diagnosed with ASD (30 males and 9 females) and 27 TDCs (14 males and 13 females) serving as control subjects. The groups did not differ in age (TDC: 11.3 ± 3.0 years, ASD: 11.7 ± 3.2 years). All participants were carefully screened, using parent report questionnaires and a telephone interview, to ensure that they did not have a history of current or prior neuropsychiatric symptomatology. Moreover, structural images were evaluated clinically by a board certified neuroradiologist and all participants were found to be completely anomaly free.

All imaging was performed using a Siemens 3T Verio^{TM}scanner using a 32 channel head coil. Structural images were acquired on all subjects using an MP-RAGE imaging sequence (TR/TE/TI = 19s/2.54ms/.9s, 0.8mm in plane resolution, 0.9mm slice thickness). Addi-

tionally two DW-MRI acquisitions were acquired:

1. A DTI acquisition was performed using single shot spin-echo, echo-planar imaging sequence with the following parameters: TR/TE = 11.0s/75 ms, b-value of $1000\,\mathrm{s/\,mm^2}$, isotropic 2mm resolution and 30 gradient directions as well as a single $b = 0\,\mathrm{s/\,mm^2}$ (b0) image.

2. A HARDI acquisition was also performed using a monopolar Stejskal-Tanner diffusion weighted spin-echo, echo-planar imaging sequence with the following parameters: TR/TE=14.8s/110ms, $b = 3000\,\mathrm{s/\,mm^2}$, 2mm isotropic resolution, and 64 gradient directions as well as two b0 images.

A.1.2. Schizophrenia Imaging

The SCZ dataset consisted of 66 controls and 66 patients. The dataset was divided based on gender and each gender group was analyzed separately, to control for the established differences observed in SCZ between the two genders [105]. The female group consisted of 29 patients and 29 controls while the group of males consisted of 37 controls and 37 patients. The groups did not differ in age (female controls: 36.6 ± 12.0 years, female patients: 40.2 ± 11.2 years, male controls: 36.3 ± 11.4 years, male patients: 36.0 ± 11.3 years) or in education. The clinical condition of the patients was evaluated by a psychiatrist and diagnosed as schizophrenia or schizoaffective type disorder. The University of Pennsylvania institutional review board approved all procedures, including recruitment and consent. Written informed consent or assent was obtained from participants.

Imaging was performed using a Siemens Trio$^{\mathrm{TM}}$3T scanner with a 12 channel head coil. Structural images were acquired on all subjects using an MP-RAGE imaging sequence with the following parameters TR/TE/TI = 1630ms/3.87ms/1.1s, 0.9375mm in plane resolution, 1mm slice thickness. A single shot spin-echo, echo planar imaging (TR/TE=6400/97ms, 1.7mm inplane resolution and 3mm contiguous slices), with 64 diffusion directions with a b-value of $1000\,\mathrm{s/\,mm^2}$, six b0 images were also acquired on each subject.

A.1.3. Test-Retest Imaging Dataset

Imaging was performed on 9 subjects (2 Female/7 Male, Age 31.25 $\pm$ 4.2 years) at two time points separated by two weeks. All participants were carefully screened to ensure that they did not have a history of current or prior neuropsychiatric symptomatology. For each subject at each timepoint, a whole brain HARDI dataset was acquired using a Siemens 3T Verio^{TM}scanner using a monopolar Stejskal-Tanner diffusion weighted spin-echo, echo-planar imaging sequence (TR/TE=14.8s/111ms, 2mm isotropic voxels, $b = 3000\,\mathrm{s/mm^2}$, number of diffusion directions=64, 2 b0 images, scan time 18 minutes). A structural image was acquired, using an MP-RAGE imaging sequence (TR/TE/TI = 19s/2.54ms/.9s, 0.8mm in plane resolution, 0.9mm slice thickness) to facilitate tissue segmentation.

A.2. Processing Pipeline

Two types of processing pipelines are utilized in these studies. One begins with a subject's DW-MRI dataset and culminates in the generation of either an FOD image or a DT image. The second is used to identify the WM and GM volumes of the subject via the segmentation of the MP-RAGE structural image.

DWI Processing

Each subject's DWI datasets were submitted to an analysis pipeline consisting of:

- **Artifact Removal:** The DW-MRI images for both acquisitions of each subject were filtered using a joint linear minimum mean squared error filter for removal of Rician noise [169].
- **Eddy Current Correction:** was then performed using affine registration of each DWI volume to the unweighted b0 image [92].
- **DT Fitting:** The subject's DT image was fit to dataset using linear least squares fitting routine

- **FOD Fitting:** Central WM voxels were first determined via affine registration to an atlas image. From these WM voxels, those with a high FA (generally 0.6) were chosen to compute the FIR. The CSD method [166] was then used to compute FOD images of order 8 ($l_{\max} = 8$) from the subject's DW-MRI dataset and their FIR.

Tissue segmentation

White matter volumes were determined from each subject's structural MP-RAGE image using the following procedure. Skull-stripping and bias field correction were performed using the BET [153] tool and N3 bias correction [152]. Tissue segmentation was then performed, to identify CSF, GM and WM voxels, using an adaptive K-means clustering [131]. A rigid body registration, between the HARDI b0 image and the bias corrected structural image was performed. Using this deformation field, the WM segmentation mask was then resampled into the diffusion space yielding a WM segmentation mask for each subject co-registered to the FOD image.

Full Pipeline

These pipelines are used in concert resulting in the following preprocessing steps:

1. FOD images are computed using the DWI processing pipeline, this is only mitigated by the choice of FA threshold used to determine the FIR.

2. If required by the specific study, DT images are also computed using the DWI processing pipeline.

3. WM and GM masks are computed using the tissue segmentation pipeline.

4. All output images are co-registered using a rigid body registration into the space of the FOD images using the FLIRT [91] software.

At the culmination of this pipeline, a subject's imaging dataset consists of co-registered FOD, WM and GM images, as well as an optional DT image.

APPENDIX B : The Real Spherical Harmonics

B.1. Mathematical Definition

The complex spherical harmonic functions (Y_l^m) are solutions to the spherical part of the Laplace equation computed in spherical coordinates and form a complete orthonormal basis for complex valued functions on the sphere.

$$Y_l^m(\theta,\phi) = \sqrt{\frac{2l+1}{4\pi}\frac{(l-m)!}{(l+m)!}} P_l^m(\cos\theta) e^{im\phi}$$

The odd ordered spherical harmonics are not antipodally symmetric, thus are often not included in expansions of symmetric functions such as those used as HARDI data models. HARDI models are also real-valued functions, thus the real spherical harmonic functions provide a more intuitive basis for functions of this type.

We use the normalized real spherical harmonics in order to maintain orthonomality. The basic definition of our basis set is as follows:

$$R_l^m(\theta,\phi) = \begin{cases} Y_l^m(\theta,\phi) & m = 0\,,\, l \text{ even} \\ \sqrt{2}\,\mathfrak{Re}\, Y_l^m(\theta,\phi) & m < 0\,,\, l \text{ even} \\ \sqrt{2}\,\mathfrak{Im}\, Y_l^m(\theta,\phi) & m > 0\,,\, l \text{ even} \end{cases} \tag{B.1}$$

A representation of a real-valued spherical function, f, can be obtained using its projection into each of these basis functions. These projections yield a succinct representation of f using its real spherical harmonic (RSH) coefficients ($\tilde{f}$).

Often there are operators that have been defined in the complex spherical harmonics, such as rotation, that are needed in the RSH space. For this reason it is also often useful to express R_l^m directly in terms of the Y_l^m functions. Allowing us to describe a change of basis operation ($\mathbf{M}$) between the two functional basis sets directly. Using the following identity

for the complex conjugate of Y_l^m,

$$\overline{Y_l^m} = (-1)^m Y_l^{-m}$$

$\mathfrak{Re}\, Y_l^m$ and $\mathfrak{Im}\, Y_l^m$ can be expressed as follows:

$$\begin{aligned}
\mathfrak{Re}\, Y_l^m &= \frac{1}{2}\left(Y_l^m + \overline{Y_l^m}\right) = \frac{1}{2}\left(Y_l^m + (-1)^m Y_l^{-m}\right) \\
\mathfrak{Im}\, Y_l^m &= \frac{1}{2i}\left(Y_l^m - \overline{Y_l^m}\right) = \frac{i}{2}\left(-Y_l^m + (-1)^m Y_l^{-m}\right)
\end{aligned}$$

This yields the following expression of equation B.1:

$$R_l^m(\theta,\phi) = \begin{cases} Y_l^m(\theta,\phi) & m = 0\,,\, l \text{ even} \\ \frac{\sqrt{2}}{2}\left(Y_l^m + (-1)^m Y_l^{-m}\right) & m < 0\,,\, l \text{ even} \\ \frac{\sqrt{2}i}{2}\left(-Y_l^m + (-1)^m Y_l^{-m}\right) & m > 0\,,\, l \text{ even} \end{cases}$$

Our implementation of the complex spherical harmonics does not include the Condon-Shortley phase [9] which is included in the definition of the associated Legendre polynomials (P_l^m). This definition yields the final RSH basis used in this work

$$R_l^m(\theta,\phi) = \begin{cases} \sqrt{\frac{(2l+1)}{4\pi}} P_l^0(\cos\theta) & m = 0\,,\, l \text{ even} \\ \sqrt{2}\sqrt{\frac{(2l+1)}{4\pi}\frac{(l-m)!}{(l+m)!}} P_l^m(\cos\theta)\cos(m\phi) & m < 0\,,\, l \text{ even} \\ \sqrt{2}\sqrt{\frac{(2l+1)}{4\pi}\frac{(l-m)!}{(l+m)!}} P_l^m(\cos\theta)\sin(m\phi) & m > 0\,,\, l \text{ even} \end{cases} \tag{B.2}$$

B.2. Rotations in the RSH basis

In order to represent a rotation operator R in $\mathbb{R}^3$, we are interested in knowing the RSH representation of $f \circ R$, where f is a given spherical function. It is well known that using the complex spherical harmonic (SH) representation $\widehat{f \circ R}$ can be expressed as $\hat{R}\,\hat{f}$, where

$\hat{R}$ is a block diagonal matrix and $\hat{f}$ are the SH coefficients of f. Each block of $\hat{R}$, there is one block matrix for each order (l) of the SH expansion, consists of a Wigner D matrix, D^l [52], that can be best described using Euler angles, $D^l(\alpha,\beta,\gamma) = D^l_z(\alpha)D^l_y(\beta)D^l_z(\gamma)$, where $D^l_z(\alpha)$ is a diagonal matrix whose diagonal elements are $e^{-im\alpha}$, while the elements of $D^l_y(\beta)$ can be expressed as

$$D^l_y(\beta)_{[m',m]} = [(l+m')!(l-m')!(l+m)!(l-m)!]^{\frac{1}{2}} \sum_{\sigma} \frac{(-1)^{l-m'-\sigma}(\cos\frac{\beta}{2})^{2\sigma+m'+m}(\sin\frac{\beta}{2})^{2l-2\sigma-m'-m}}{(m-mp-\sigma)!(l-m'-\sigma)!(l-m-\sigma)!}$$

Clearly the computation of D^l_y is more extensive then that of D^l_z, so in applications where many reorientations must be performed, such as spatial normalization, it is advantageous to decompose $D^l_y(\beta)$ into rotations about y and z

$$D^l_y(\beta) = D^l_z(\frac{\pi}{2})D^l_y(\frac{\pi}{2})D^l_z(\beta)D^l_y(-\frac{\pi}{2})D^l_z(-\frac{\pi}{2})$$

allowing $D^l_z(\frac{\pi}{2})$, $D^l_y(\frac{\pi}{2})$, $D^l_y(-\frac{\pi}{2})$ and $D^l_z(-\frac{\pi}{2})$ to be precomputed, leaving only the diagonal matrices $D^l_z(\alpha)$, $D^l_z(\beta)$ and $D^l_z(\gamma)$ to be computed for each rotation operation performed.

Once $\hat{R}$ is computed the rotation operation in RSH space ($\tilde{R}$) can be expressed as $\tilde{R} = M^{-1}\hat{R}M$, where M is the change of basis operation from the RSH basis to the SH basis.

B.3. Spectral Powers of the RSH

As discussed above the basis functions of each RSH order (l level) span a subspace which is closed under rotations [52, 57, 67], since $\hat{R}$ is block diagonal. This allows us to compute the spectral power within each order as a rotational invariant feature vector $\mathbf{v}$ of a function

f:

$$\mathbf{v}_l = \sum_m (\tilde{f}_{l,m})^2 \tag{B.3}$$

where $\tilde{f}$ are the RSH coefficients of f. This orientation invariant representation is used a number of places throughout this thesis, most crucially in the spatial normalization methods (Chapter 3) and in preforming voxel and regional statistics (Chapter 6).

The interpretation of the RSH spectral powers is of particular interest due to their sensitivity to the shape of the underlying diffusion model. The most straight forward interpretation derives from the basis functions that make up each RSH order. The 0^{th} order basis is isotropic, while the basis functions of the 2^{nd}, 4^{th} and 6^{th} orders respectively have 2, 3 and 4 antipodally symmetric peaks. This certainly encourages the interpretation that the spectral powers above the 2^{nd} order represent increases in the amount of complex structure. It is important to consider that, similar to the linear harmonics where higher frequencies are required to represent shaper features, higher orders of the RSH basis are required to model sharper, more anisotropic, peaks. For instance, the highest regions of all spectral powers of the FOD diffusion model, occur in the CC.

B.4. Established Metrics

From an analysis perspective, the utility of the RSH derives from the fact that it provides a simple linear space to represent many of HARDI diffusion models. This permits the development of analysis methods which can be applied to any DW-MRI model provided it is a spherical function.

The inner product provided by the RSH functions

$$\langle f, g \rangle = \int_{\mathbb{S}} d\theta d\phi f(\theta, \phi) g(\theta, \phi) = \sum_{l=0, l \text{ even}}^{\infty} \sum_{m=-l}^{l} \tilde{f}_{lm} \, \tilde{g}_{lm} \tag{B.4}$$

allows the definition of two metrics that are used in the various analysis methods presented

in this thesis

$$d_f(f,g) = \sqrt{\langle f-g, f-g\rangle} = \sqrt{\sum_{l=0,l \text{ even}}^{\infty} \sum_{m=-l}^{l} (\tilde{f}_{l,m} - \tilde{g}_{l,m})^2} \tag{B.5}$$

$$d_N(f,g) = \sqrt{\sum_{l=0,l \text{ even}}^{\infty} \sum_{m=-l}^{l} \frac{1}{2\sqrt{\pi}\tilde{f}_{0,0}}\tilde{f}_{l,m} - \frac{1}{2\sqrt{\pi}\tilde{g}_{0,0}}\tilde{g}_{l,m})^2} \tag{B.6}$$

$$d_{OI}(f,g) = \sqrt{\sum_{l=0,l \text{ even}}^{\infty} (\sum(\tilde{f}_{l,m})^2 - \sum(\tilde{g}_{l,m})^2)} \tag{B.7}$$

The first of these, equation B.5, is the L_2 distance between the RSH coefficients and is thus sensitive the all aspects of the diffusion model being represented. The second, equation B.6, is the L_2 distance between the RSH coefficients of the normalized functions, and is thus more sensitive the shape and orientation of the functions than to there overall size. The L_2 distance in the spectral power space, equation B.7, is invariant to the orientation of the functions and only sensitive their respective shapes.

APPENDIX C : Thesis Publications

Peer-Reviewed Journal Publications

1. Luke Bloy, Madhura Ingalhalikar, Nematollah K. Batmanghelich, Robert T. Schultz, Timothy P. L. Roberts, and Ragini Verma. An integrated framework for HARDI-based investigation of structural connectivity. *Brain Connectivity*, [in Press], Apr 2012.

2. Luke Bloy, Madhura Ingalhalikar, Harini Eavani, Robert T. Schultz, Timothy P. L. Roberts, and Ragini Verma. White matter atlas generation using HARDI based automated parcellation. *Neuroimage*, 59(4):4055–4063, Feb 2012.

3. Madhura Ingalhalikar, Drew Parker, Luke Bloy, Timothy P. L. Roberts, and Ragini Verma. Diffusion based abnormality markers of pathology: Toward learned diagnostic prediction of ASD. *Neuroimage*, 57(3):918–927, Aug 2011.

4. Demian Wassermann, Luke Bloy, Efstathios Kanterakis, Ragini Verma, and Rachid Deriche. Unsupervised white matter fiber clustering and tract probability map generation: applications of a Gaussian process framework for white matter fibers. *Neuroimage*, 51(1):228–241, May 2010.

Peer-Reviewed Conference Publications

1. Luke Bloy, Madhura Ingalhalikar, and Ragini Verma. Neuronal white matter parcellation using spatially coherent normalized cuts. *Proc IEEE International Symposium on Biomedical Imaging*, pages 2061–2065, 2011.

2. Luke Bloy, Madhura Ingalhalikar, Harini Eavani, Timothy P. L. Roberts, Robert T. Schultz, and Ragini Verma. HARDI based pattern classifiers for the identification of white matter pathologies. *Medical Image Computing and Computer Assisted Inter-*

vention, 14(Pt 2):234–241, 2011.

3. Luke Bloy and Ragini Verma. Demons registration of high angular resolution diffusion images. *Proc IEEE International Symposium on Biomedical Imaging*, pages 1013–1016, 2010.

4. Luke Bloy and Ragini Verma. On computing the underlying fiber directions from the diffusion orientation distribution function. *Medical Image Computing and Computer Assisted Intervention*, 11(Pt 1):1–8, 2008.

5. Yasser Ghanbari, Luke Bloy, Kayhan Batmanghelich, Timothy P.L. Roberts, and Ragini Verma. Dominant component analysis of electrophysiological connectivity networks. *Medical Image Computing and Computer Assisted Intervention*, Submitted, 2012.

6. Madhura Ingalhalikar, Drew Parker, Luke Bloy, Timothy P. L. Roberts, and Ragini Verma. Using multiparametric data with missing features for learning patterns of pathology. *Medical Image Computing and Computer Assisted Intervention*, Accepted, 2012.

7. Madhura Ingalhalikar, Alex Smith, Drew Parker, Luke Bloy, Ruben Gur, Timothy P. L. Roberts, and Ragini Verma. Identifying sub-populations via unsupervised cluster analysis on multi-edge similarity graphs. *Medical Image Computing and Computer Assisted Intervention*, Accepted, 2012.

Conference Abstracts

1. Luke Bloy, Madhura Ingalhalikar, Robert T. Schultz, Timothy P.L. Roberts, and Ragini Verma. Neuronal white matter atlas creation using diffusion imaging. In *Proceedings of the 20th Annual Meeting of ISMRM*, 2012.

2. Luke Bloy, Alex Smith, Madhura Ingalhalikar, Robert T. Schultz, Timothy P.L.

Roberts, and Ragini Verma. Towards assessing spatial normalizations employing DTI and HARDI models. In *Proceedings of the 20th Annual Meeting of ISMRM*, 2012.

3. Harini Eavani, Luke Bloy, John Herrington, Robert T. Schultz, and Ragini Verma. Fiber tracking of the arcuate fasciculus in autism using high angular resolution diffusion imaging. In *Proceedings of the 19th Annual Meeting of ISMRM*, 2011.

4. Luke Bloy and Ragini Verma. Featured based deformable registration of diffusion MRI using the fiber orientation distribution. In *Proceedings of the 18th Annual Meeting of ISMRM*, 2010.

Acronyms

ADC	Apparent Diffusion Coefficient
ASD	Autism Spectrum Disorder
CC	Corpus Callosum
CSD	Constrained Spherical Deconvolution
CSF	Cerebrospinal Fluid
CST	Cortical Spinal Tract
DSI	Diffusion Spectrum Imaging
DT	Diffusion Tensor
DTI	Diffusion Tensor Imaging
DW-MRI	Diffusion Weighted Magnetic Resonance Imaging
DWI	Diffusion Weighted Image
FA	Fractional Anisotropy
FIR	Fiber Impulse Response
fMRI	Functional Magnetic Resonance Imaging
FOD	Fiber Orientation Distribution
FS	Finite Strain
GFA	Generalized Fractional Anisotropy
GM	Gray Matter
HARDI	High Angular Resolution Diffusion Imaging
IC	Internal Capsule
IFOF	Inferior Fronto-occipital Fasciculus
ILF	Inferior Longitudinal Fasciculus
MC	Monte-Carlo
MR	Magnetic Resonance
MRI	Magnetic Resonance Imaging
nCD	Nodal Connection Density
ODF	Orientation Distribution Function
OI	Orientation Invariant
OS	Orientation Sensitive
PGSE	Pulsed Gradient Spin Echo
QBI	Q-ball Imaging

QSI	Q-space Imaging
ROI	Region of Interest
RSH	Real Spherical Harmonic
SCZ	Schizophrenia
SD	Spherical Deconvolution
SLF	Superior Longitudinal Fasciculus
SNR	Signal to Noise
SS	Sagittal Stratum
TDC	Typically Developing Children
TDI	Track Density Imaging
WM	White Matter

BIBLIOGRAPHY

[1] F. Aboitiz, A. B. Scheibel, R. S. Fisher, and E. Zaidel. Fiber composition of the human corpus callosum. *Brain Research*, 598(1-2):143–153, Dec 1992. 74

[2] I. Aganj, C. Lenglet, G. Sapiro, E. Yacoub, K. Ugurbil, and N. Harel. Reconstruction of the orientation distribution function in single- and multiple-shell q-ball imaging within constant solid angle. *Magnetic Resonance in Medicine*, 64(2):554–566, Aug 2010. 3, 15

[3] D. Alexander, G. Barker, and S. Arridge. Detection and modeling of non-gaussian apparent diffusion coefficient profiles in human brain data. *Magnetic Resonance in Medicine*, 48(2):331–340, 2002. 15

[4] D. Alexander, C. Pierpaoli, P. Basser, and J. Gee. Spatial transformations of diffusion tensor magnetic resonance images. *IEEE Transactions on Medical Imaging*, 20(11):1131–1139, 2001. 27

[5] E. A. Allen, E. B. Erhardt, E. Damaraju, W. Gruner, J. M. Segall, R. F. Silva, M. Havlicek, S. Rachakonda, J. Fries, R. Kalyanam, A. M. Michael, A. Caprihan, J. A. Turner, T. Eichele, S. Adelsheim, A. D. Bryan, J. Bustillo, V. P. Clark, S. W. F. Ewing, F. Filbey, C. C. Ford, K. Hutchison, R. E. Jung, K. A. Kiehl, P. Kodituwakku, Y. M. Komesu, A. R. Mayer, G. D. Pearlson, J. P. Phillips, J. R. Sadek, M. Stevens, U. Teuscher, R. J. Thoma, and V. D. Calhoun. A baseline for the multivariate comparison of resting-state networks. *Frontiers in Systems Neuroscience*, 5:2, 2011. 89

[6] S. H. Ameis, J. Fan, C. Rockel, A. N. Voineskos, N. J. Lobaugh, L. Soorya, A. T. Wang, E. Hollander, and E. Anagnostou. Impaired structural connectivity of socio-emotional circuits in autism spectrum disorders: a diffusion tensor imaging study. *PLoS One*, 6(11):e28044, 2011. 19, 88, 90

[7] K. Amunts, A. Schleicher, U. Brgel, H. Mohlberg, H. B. Uylings, and K. Zilles. Broca's region revisited: cytoarchitecture and intersubject variability. *Journal of Comparative Neurology*, 412(2):319–341, Sep 1999. 96

[8] A. W. Anderson. Measurement of fiber orientation distributions using high angular resolution diffusion imaging. *Magnetic Resonance in Medicine*, 54(5):1194–1206, 2005. 3, 16

[9] G. Arfken. *Mathematical Methods for Physicists*. Academic Press, 3rd edition edition, 1985. 103

[10] F. Arnold. *Tabulae Anatomicae. Fasciculus I. Continens Icones cerebri et medullae spinalis*. Turici, Imprensisi Orelii, Fuesslini et sociorum, 1838. 2

[11] V. Arsigny, P. Fillard, X. Pennec, and N. Ayache. Log-euclidean metrics for fast and simple calculus on diffusion tensors. *Magnetic Resonance in Medicine*, 56(2):411–421, Aug 2006. 11, 33, 34

[12] J. Ashburner. Computational anatomy with the spm software. *Magnetic Resonance Imaging*, 27(8):1163–1174, Oct 2009. 39

[13] J. Ashburner and K. J. Friston. Voxel-based morphometry–the methods. *Neuroimage*, 11(6 Pt 1):805–821, Jun 2000. 23, 37

[14] J. Ashburner, C. Hutton, R. Frackowiak, I. Johnsrude, C. Price, and K. Friston. Identifying global anatomical differences: deformation-based morphometry. *Human Brain Mapping*, 6(5-6):348–357, 1998. 23, 37

[15] Y. Assaf, M. Kafri, H. Shinar, J. Chapman, A. D. Korczyn, G. Navon, and Y. Cohen. Changes in axonal morphology in experimental autoimmune neuritis as studied by high b-value q-space (1)h and (2)h dqf diffusion magnetic resonance spectroscopy. *Magnetic Resonance in Medicine*, 48(1):71–81, Jul 2002. 14

[16] S. Balay, W. D. Gropp, L. C. McInnes, and B. F. Smith. *Efficient management of parallelism in object-oriented numerical software libraries*, pages 163–202. Birkhauser Boston Inc., Cambridge, MA, USA, 1997. 62

[17] P. J. Basser, J. Mattiello, and D. LeBihan. Estimation of the effective self-diffusion tensor from the nmr spin echo. *Journal of Magnetic Resonance B*, 103(3):247–254, Mar 1994. 2, 10

[18] P. J. Basser, S. Pajevic, C. Pierpaoli, J. Duda, and A. Aldroubi. In vivo fiber tractography using dt-mri data. *Magnetic Resonance in Medicine*, 44(4):625–632, Oct 2000. 22

[19] P. J. Basser and C. Pierpaoli. Microstructural and physiological features of tissues elucidated by quantitative-diffusion-tensor mri. *Journal of Magnetic Resonance B*, 111(3):209–219, Jun 1996. 11

[20] D. S. Bassett, E. Bullmore, B. A. Verchinski, V. S. Mattay, D. R. Weinberger, and A. Meyer-Lindenberg. Hierarchical organization of human cortical networks in health and schizophrenia. *Journal of Neuroscience*, 28(37):9239–9248, Sep 2008. 81

[21] T. E. J. Behrens, H. J. Berg, S. Jbabdi, M. F. S. Rushworth, and M. W. Woolrich. Probabilistic diffusion tractography with multiple fibre orientations: What can we gain? *Neuroimage*, 34(1):144–155, Jan 2007. 3, 22

[22] T. E. J. Behrens, M. W. Woolrich, M. Jenkinson, H. Johansen-Berg, R. G. Nunes, S. Clare, P. M. Matthews, J. M. Brady, and S. M. Smith. Characterization and propagation of uncertainty in diffusion-weighted mr imaging. *Magnetic Resonance in Medicine*, 50(5):1077–1088, Nov 2003. 12, 22, 56, 59

[23] D. L. Bihan, E. Breton, D. Lallemand, P. Grenier, E. Cabanis, and M. Laval-Jeantet. Mr imaging of intravoxel incoherent motions: application to diffusion and perfusion in neurologic disorders. *Radiology*, 161(2):401–407, Nov 1986. 1, 2, 10

[24] D. L. Bihan and H. Johansen-Berg. Diffusion mri at 25: Exploring brain tissue structure and function. *Neuroimage*, Nov 2011. 19

[25] L. Bloy and R. Verma. On computing the underlying fiber directions from the diffusion orientation distribution function. *Medical Image Computing and Computer Assisted Intervention*, 11(Pt 1):1–8, 2008. 95

[26] M. K. Bode, M.-L. Mattila, V. Kiviniemi, J. Rahko, I. Moilanen, H. Ebeling, O. Tervonen, and J. Nikkinen. White matter in autism spectrum disorders - evidence of impaired fiber formation. *Acta Radiologica*, 52(10):1169–1174, Dec 2011. 2

[27] K. Brodmann. *Vergleichende Lokalisationslehre der Grosshirnrinde in ihren Prinzipien dargestellt auf Grund des Zellenbaues*. Johann Ambrosius Barth Verlag, 1909. 52

[28] C. C. Brun, R. Nicolson, N. Lepor, Y.-Y. Chou, C. N. Vidal, T. J. DeVito, D. J. Drost, P. C. Williamson, N. Rajakumar, A. W. Toga, and P. M. Thompson. Mapping brain abnormalities in boys with autism. *Human Brain Mapping*, 30(12):3887–3900, Dec 2009. 88

[29] E. T. Bullmore, S. Frangou, and R. M. Murray. The dysplastic net hypothesis: an integration of developmental and dysconnectivity theories of schizophrenia. *Schizophrenia Research*, 28(2-3):143–156, Dec 1997. 18, 81, 87

[30] W. Byne, E. A. Hazlett, M. S. Buchsbaum, and E. Kemether. The thalamus and schizophrenia: current status of research. *Acta Neuropathologica*, 117(4):347–368, Apr 2009. 87

[31] F. Calamante, J.-D. Tournier, G. D. Jackson, and A. Connelly. Track-density imaging (tdi): super-resolution white matter imaging using whole-brain track-density mapping. *Neuroimage*, 53(4):1233–1243, Dec 2010. 55, 70

[32] P. T. Callaghan. *Principles of Nuclear Magnetic Resonance Microscopy*. Oxford University Press, New York., 1993. 14

[33] P. T. Callaghan, C. D. Eccles, and Y. Xia. Nmr microscopy of dynamic displacements: k-space and q-space imaging. *Journal of Physics E: Scientific Instruments*, 21(8):820–, 1988. 14

[34] M. F. Casanova, A. El-Baz, E. Vanbogaert, P. Narahari, and A. Switala. A topographic study of minicolumnar core width by lamina comparison between autistic subjects and controls: possible minicolumnar disruption due to an anatomical ele-

ment in-common to multiple laminae. *Brain Pathology*, 20(2):451–458, Mar 2010. 74, 90

[35] E. Cassol, J.-P. Ranjeva, D. Ibarrola, C. Mkies, C. Manelfe, M. Clanet, and I. Berry. Diffusion tensor imaging in multiple sclerosis: a tool for monitoring changes in normal-appearing white matter. *Multiple Sclerosis*, 10(2):188–196, Apr 2004. 2

[36] M. C. Chiang, A. D. Leow, A. D. Klunder, R. A. Dutton, M. Barysheva, S. E. Rose, K. L. McMahon, G. I. de Zubicaray, A. W. Toga, and P. M. Thompson. Fluid registration of diffusion tensor images using information theory. *IEEE Transactions on Medical Imaging*, 27(4):442–456, Apr 2008. 24

[37] T. G. Close, J.-D. Tournier, F. Calamante, L. A. Johnston, I. Mareels, and A. Connelly. A software tool to generate simulated white matter structures for the assessment of fibre-tracking algorithms. *Neuroimage*, 47(4):1288–1300, Oct. 2009. 46, 47

[38] A. L. Cohen, D. A. Fair, N. U. F. Dosenbach, F. M. Miezin, D. Dierker, D. C. V. Essen, B. L. Schlaggar, and S. E. Petersen. Defining functional areas in individual human brains using resting functional connectivity mri. *Neuroimage*, 41(1):45–57, May 2008. 96

[39] D. L. Collins, C. J. Holmes, T. M. Peters, and A. C. Evans. Automatic 3-d model-based neuroanatomical segmentation. *Human Brain Mapping*, 3(3):190–208, 1995. 39

[40] T. E. Conturo, N. F. Lori, T. S. Cull, E. Akbudak, A. Z. Snyder, J. S. Shimony, R. C. McKinstry, H. Burton, and M. E. Raichle. Tracking neuronal fiber pathways in the living human brain. *Proceedings of the National Academy of Sciences of the United States of America*, 96(18):10422–10427, Aug 1999. 22

[41] I. Corouge, P. T. Fletcher, S. Joshi, S. Gouttard, and G. Gerig. Fiber tract-oriented statistics for quantitative diffusion tensor mri analysis. *Medical Image Analysis*, 10(5):786–798, Oct 2006. 21

[42] E. Courchesne and K. Pierce. Why the frontal cortex in autism might be talking only to itself: local over-connectivity but long-distance disconnection. *Current Opinion in Neurobiology*, 15(2):225–230, Apr 2005. 19, 90

[43] E. Courchesne, K. Pierce, C. M. Schumann, E. Redcay, J. A. Buckwalter, D. P. Kennedy, and J. Morgan. Mapping early brain development in autism. *Neuron*, 56(2):399–413, Oct 2007. 88, 90

[44] R. W. Cox. Afni: software for analysis and visualization of functional magnetic resonance neuroimages. *Computers and Biomedical Research*, 29(3):162–173, Jun 1996. 83

[45] C. Davatzikos, A. Genc, D. Xu, and S. M. Resnick. Voxel-based morphometry using the ravens maps: methods and validation using simulated longitudinal atrophy. *Neuroimage*, 14(6):1361–1369, Dec 2001. 23, 37

[46] M. A. Deeley, A. Chen, R. Datteri, J. H. Noble, A. J. Cmelak, E. F. Donnelly, A. W. Malcolm, L. Moretti, J. Jaboin, K. Niermann, E. S. Yang, D. S. Yu, F. Yei, T. Koyama, G. X. Ding, and B. M. Dawant. Comparison of manual and automatic segmentation methods for brain structures in the presence of space-occupying lesions: a multi-expert study. *Physics in Medicine and Biology*, 56(14):4557–4577, Jul 2011. 40

[47] M. Descoteaux, E. Angelino, S. Fitzgibbons, and R. Deriche. Regularized, fast, and robust analytical q-ball imaging. *Magnetic Resonance in Medicine*, 58(3):497–510, 2007. 3, 15

[48] M. Descoteaux, R. Deriche, D. L. Bihan, J.-F. Mangin, and C. Poupon. Multiple q-shell diffusion propagator imaging. *Medical Image Analysis*, 15(4):603–621, Aug 2011. 14

[49] M. Descoteaux, R. Deriche, T. R. Knsche, and A. Anwander. Deterministic and probabilistic tractography based on complex fibre orientation distributions. *IEEE Transactions on Medical Imaging*, 28(2):269–286, Feb 2009. 75

[50] R. S. Desikan, F. Sgonne, B. Fischl, B. T. Quinn, B. C. Dickerson, D. Blacker, R. L. Buckner, A. M. Dale, R. P. Maguire, B. T. Hyman, M. S. Albert, and R. J. Killiany. An automated labeling system for subdividing the human cerebral cortex on mri scans into gyral based regions of interest. *Neuroimage*, 31(3):968–980, Jul 2006. 65, 80

[51] Q. Dong, R. C. Welsh, T. L. Chenevert, R. C. Carlos, P. Maly-Sundgren, D. M. Gomez-Hassan, and S. K. Mukherji. Clinical applications of diffusion tensor imaging. *Journal of Magnetic Resonance Imaging*, 19(1):6–18, Jan 2004. 19

[52] A. R. Edmonds. *Angular Momentum in Quantum Mechanics*. Princeton University Press, 1960. 104

[53] A. Einstein. *Investigations on the Theory of the Brownian Movement*. Dover Publishing, 1956. 8

[54] P. Fillard, X. Pennec, V. Arsigny, and N. Ayache. Clinical dt-mri estimation, smoothing, and fiber tracking with log-euclidean metrics. *IEEE Transactions on Medical Imaging*, 26(11):1472–1482, Nov 2007. 11, 22

[55] B. Fischl, M. I. Sereno, and A. M. Dale. Cortical surface-based analysis. ii: Inflation, flattening, and a surface-based coordinate system. *Neuroimage*, 9(2):195–207, Feb 1999. 65, 80

[56] A. Fornito, M. Ycel, S. J. Wood, C. Adamson, D. Velakoulis, M. M. Saling, P. D. McGorry, and C. Pantelis. Surface-based morphometry of the anterior cingulate cortex in first episode schizophrenia. *Human Brain Mapping*, 29(4):478–489, Apr 2008. 87

[57] L. R. Frank. Characterization of anisotropy in high angular resolution diffusion-weighted mri. *Magnetic Resonance in Medicine*, 47(6):1083–1099, 2002. 15, 104

[58] K. J. Friston. The disconnection hypothesis. *Schizophrenia Research*, 30(2):115–125, Mar 1998. 18, 81, 87

[59] X. Geng, T. Ross, W. Zhan, H. Gu, Y.-P. Chao, C.-P. Lin, G. Christensen, N. Schuff, and Y. Yang. Diffusion mri registration using orientation distribution functions. *Information Processing in Medical Imaging*, pages 626–637, 2009. 25

[60] C. Genovese, N. Lazar, and T. Nichols. Thresholding of statistical maps in functional neuroimaging using the false discovery rate. *Neuroimage*, 15(4):870–878, 2002. 35

[61] A. Ghosh and R. Deriche. Extracting geometrical features & peak fractional anisotropy from the odf for white matter characterization. In *Biomedical Imaging: From Nano to Macro, 2011 IEEE International Symposium on*, pages 266–271, 2011. 95

[62] D. C. Glahn, A. R. Laird, I. Ellison-Wright, S. M. Thelen, J. L. Robinson, J. L. Lancaster, E. Bullmore, and P. T. Fox. Meta-analysis of gray matter anomalies in schizophrenia: application of anatomic likelihood estimation and network analysis. *Biological Psychiatry*, 64(9):774–781, Nov 2008. 87

[63] G. Gong, Y. He, L. Concha, C. Lebel, D. W. Gross, A. C. Evans, and C. Beaulieu. Mapping anatomical connectivity patterns of human cerebral cortex using in vivo diffusion tensor imaging tractography. *Cerebral Cortex*, 19(3):524–536, Mar 2009. 56

[64] G. Gong, P. Rosa-Neto, F. Carbonell, Z. J. Chen, Y. He, and A. C. Evans. Age- and gender-related differences in the cortical anatomical network. *Journal of Neuroscience*, 29(50):15684–15693, Dec 2009. 2, 18, 56, 59, 73

[65] C. B. Goodlett, P. T. Fletcher, J. H. Gilmore, and G. Gerig. Group analysis of dti fiber tract statistics with application to neurodevelopment. *Neuroimage*, 45(1 Suppl):S133–S142, Mar 2009. 21

[66] H. Gray. *Grays Anatomy of the Human Body*. LEA & FEBIGER, 1918. 1

[67] R. Green. Spherical harmonic lighting: The gritty details. In *Archives of the Game Developers Conference*, 2003. 104

[68] A. Guimond, C. Guttmann, S. Warfield, and C.-F. Westin. Deformable registration of dt-mri data based on transformation invariant tensor characteristics. In *Proc. IEEE International Symposium on Biomedical Imaging*, pages 761–764, 2002. 22

[69] R. E. Gur and R. C. Gur. Functional magnetic resonance imaging in schizophrenia. *Dialogues in Clinical Neuroscience*, 12(3):333–343, 2010. 81

[70] P. Hagmann, L. Cammoun, X. Gigandet, R. Meuli, C. J. Honey, V. J. Wedeen, and O. Sporns. Mapping the structural core of human cerebral cortex. *PLoS Biology*, 6(7):e159, Jul 2008. 1, 55

[71] P. Hagmann, M. Kurant, X. Gigandet, P. Thiran, V. J. Wedeen, R. Meuli, and J.-P. Thiran. Mapping human whole-brain structural networks with diffusion mri. *PLoS One*, 2(7):e597, 2007. 55

[72] P. Hagmann, O. Sporns, N. Madan, L. Cammoun, R. Pienaar, V. J. Wedeen, R. Meuli, J.-P. Thiran, and P. E. Grant. White matter maturation reshapes structural connectivity in the late developing human brain. *Proceedings of the National Academy of Sciences of the United States of America*, 107(44):19067–19072, Nov 2010. 18, 55

[73] P. Hagmann, J.-P. Thiran, L. Jonasson, P. Vandergheynst, S. Clarke, P. Maeder, and R. Meuli. Dti mapping of human brain connectivity: statistical fibre tracking and virtual dissection. *Neuroimage*, 19(3):545–554, Jul 2003. 12

[74] J. Hamm, D. H. Ye, R. Verma, and C. Davatzikos. Gram: A framework for geodesic registration on anatomical manifolds. *Medical Image Analysis*, 14(5):633–642, Oct 2010. 40

[75] S. Hannoun, F. Durand-Dubief, C. Confavreux, D. Ibarrola, N. Streichenberger, F. Cotton, C. R. G. Guttmann, and D. Sappey-Marinier. Diffusion tensor-mri evidence for extra-axonal neuronal degeneration in caudate and thalamic nuclei of patients with multiple sclerosis. *American Journal of Neuroradiology*, Mar 2012. 2

[76] K. M. Hasan, A. Sankar, C. Halphen, L. A. Kramer, M. E. Brandt, J. Juranek, P. T. Cirino, J. M. Fletcher, A. C. Papanicolaou, and L. Ewing-Cobbs. Development and organization of the human brain tissue compartments across the lifespan using diffusion tensor imaging. *Neuroreport*, 18(16):1735–1739, Oct 2007. 18

[77] H. C. Hazlett, M. D. Poe, G. Gerig, R. G. Smith, and J. Piven. Cortical gray and white brain tissue volume in adolescents and adults with autism. *Biological Psychiatry*, 59(1):1–6, Jan 2006. 88

[78] D. M. Healy, H. Hendriks, and P. T. Kim. Spherical deconvolution. *Journal of Multivariate Analysis*, 67(1):1–22, Oct. 1998. 16

[79] W. V. Hecke, A. Leemans, C. A. Sage, L. Emsell, J. Veraart, J. Sijbers, S. Sunaert, and P. M. Parizel. The effect of template selection on diffusion tensor voxel-based analysis results. *Neuroimage*, 55(2):566–573, Mar 2011. 40

[80] W. V. Hecke, J. Sijbers, E. D'Agostino, F. Maes, S. D. Backer, E. Vandervliet, P. M. Parizel, and A. Leemans. On the construction of an inter-subject diffusion tensor

magnetic resonance atlas of the healthy human brain. *Neuroimage*, 43(1):69–80, Oct 2008. 40

[81] V. Hernandez, J. E. Roman, and V. Vidal. SLEPc: A scalable and flexible toolkit for the solution of eigenvalue problems. *ACM Transactions on Mathematical Software*, 31(3):351–362, Sept. 2005. 45

[82] M. A. Heroux, R. A. Bartlett, V. E. Howle, R. J. Hoekstra, J. J. Hu, T. G. Kolda, R. B. Lehoucq, K. R. Long, R. P. Pawlowski, E. T. Phipps, A. G. Salinger, H. K. Thornquist, R. S. Tuminaro, J. M. Willenbring, A. Williams, and K. S. Stanley. An overview of the trilinos project. *ACM Transactions on Mathematical Software*, 31(3):397–423, 2005. 62

[83] C. P. Hess, P. Mukherjee, E. T. Han, D. Xu, and D. B. Vigneron. Q-ball reconstruction of multimodal fiber orientations using the spherical harmonic basis. *Magnetic Resonance in Medicine*, 56(1):104–117, 2006. 15

[84] J. R. Highley, M. M. Esiri, B. McDonald, M. Cortina-Borja, B. M. Herron, and T. J. Crow. The size and fibre composition of the corpus callosum with respect to gender and schizophrenia: a post-mortem study. *Brain*, 122 (Pt 1):99–110, Jan 1999. 69, 74

[85] X. Hong, L. R. Arlinghaus, and A. W. Anderson. Spatial normalization of the fiber orientation distribution based on high angular resolution diffusion imaging data. *Magnetic Resonance in Medicine*, 61(6):1520–1527, Jun 2009. 25

[86] J. Iglesias, P. Thompson, C.-Y. Liu, and Z. Tu. Discretizing stochastic tractography: A fast implementation. In *IEEE International Symposium on Biomedical Imaging: From Nano to Macro*, pages 1381–1384, 2010. 56, 62

[87] M. Ingalhalikar, D. Parker, L. Bloy, T. P. L. Roberts, and R. Verma. Diffusion based abnormality markers of pathology: Toward learned diagnostic prediction of asd. *Neuroimage*, 57(3):918–927, Aug 2011. 2, 93

[88] M. Ingalhalikar, J. Yang, C. Davatzikos, and R. Verma. Dti-droid: Diffusion tensor imaging-deformable registration using orientation and intensity descriptors. *International Journal of Imaging Systems and Technology*, 20(2):99–107, 2010. 22, 24, 33, 78

[89] Y. Iturria-Medina, E. J. Canales-Rodrguez, L. Melie-Garca, P. A. Valds-Hernndez, E. Martnez-Montes, Y. Alemn-Gmez, and J. M. Snchez-Bornot. Characterizing brain anatomical connections using diffusion weighted mri and graph theory. *Neuroimage*, 36(3):645–660, Jul 2007. 56

[90] Y. Iturria-Medina, R. C. Sotero, E. J. Canales-Rodrguez, Y. Alemn-Gmez, and L. Melie-Garca. Studying the human brain anatomical network via diffusion-weighted mri and graph theory. *Neuroimage*, 40(3):1064–1076, Apr 2008. 56

[91] M. Jenkinson and S. Smith. A global optimisation method for robust affine registration of brain images. *Medical Image Analysis*, 5(2):143–156, Jun 2001. 101

[92] P. Jezzard, A. S. Barnett, and C. Pierpaoli. Characterization of and correction for eddy current artifacts in echo planar diffusion imaging. *Magnetic Resonance in Medicine*, 39(5):801–812, May 1998. 100

[93] M. A. Just, V. L. Cherkassky, T. A. Keller, R. K. Kana, and N. J. Minshew. Functional and anatomical cortical underconnectivity in autism: evidence from an fmri study of an executive function task and corpus callosum morphometry. *Cerebral Cortex*, 17(4):951–961, Apr 2007. 88

[94] K. Konrad and S. B. Eickhoff. Is the adhd brain wired differently? a review on structural and functional connectivity in attention deficit hyperactivity disorder. *Human Brain Mapping*, 31(6):904–916, Jun 2010. 55

[95] B. W. Kreher, J. F. Schneider, I. Mader, E. Martin, J. Hennig, and K. A. Il'yasov. Multitensor approach for analysis and tracking of complex fiber configurations. *Magnetic Resonance in Medicine*, 54(5):1216–1225, Nov 2005. 17

[96] M. Kubicki, R. McCarley, C.-F. Westin, H.-J. Park, S. Maier, R. Kikinis, F. A. Jolesz, and M. E. Shenton. A review of diffusion tensor imaging studies in schizophrenia. *Journal of Psychiatric Research*, 41(1-2):15–30, 2007. 2, 19, 48

[97] J. L. Lancaster, D. Tordesillas-Gutirrez, M. Martinez, F. Salinas, A. Evans, K. Zilles, J. C. Mazziotta, and P. T. Fox. Bias between mni and talairach coordinates analyzed using the icbm-152 brain template. *Human Brain Mapping*, 28(11):1194–1205, Nov 2007. 39

[98] J. L. Lancaster, M. G. Woldorff, L. M. Parsons, M. Liotti, C. S. Freitas, L. Rainey, P. V. Kochunov, D. Nickerson, S. A. Mikiten, and P. T. Fox. Automated talairach atlas labels for functional brain mapping. *Human Brain Mapping*, 10(3):120–131, Jul 2000. 39

[99] B. A. Landman, J. A. Bogovic, H. Wan, F. E. Z. ElShahaby, P.-L. Bazin, and J. L. Prince. Resolution of crossing fibers with constrained compressed sensing using diffusion tensor mri. *Neuroimage*, 59(3):2175–2186, Feb 2012. 14

[100] N. Lange, M. B. Dubray, J. E. Lee, M. P. Froimowitz, A. Froehlich, N. Adluru, B. Wright, C. Ravichandran, P. T. Fletcher, E. D. Bigler, A. L. Alexander, and J. E. Lainhart. Atypical diffusion tensor hemispheric asymmetry in autism. *Autism Research*, 3(6):350–358, Dec 2010. 93

[101] M. Lazar, D. M. Weinstein, J. S. Tsuruda, K. M. Hasan, K. Arfanakis, M. E. Meyerand, B. Badie, H. A. Rowley, V. Haughton, A. Field, and A. L. Alexander. White matter tractography using diffusion tensor deflection. *Human Brain Mapping*, 18(4):306–321, Apr 2003. 12, 22

[102] C. Lebel, M. Gee, R. Camicioli, M. Wieler, W. Martin, and C. Beaulieu. Diffusion tensor imaging of white matter tract evolution over the lifespan. *Neuroimage*, 60(1):340–352, Mar 2012. 18

[103] D. Leclercq, C. Delmaire, N. M. de Champfleur, J. Chiras, and S. Lehricy. Diffusion tractography: methods, validation and applications in patients with neurosurgical lesions. *Neurosurgery Clinics of North America*, 22(2):253–68, ix, Apr 2011. 20

[104] J. E. Lee, E. D. Bigler, A. L. Alexander, M. Lazar, M. B. DuBray, M. K. Chung, M. Johnson, J. Morgan, J. N. Miller, W. M. McMahon, J. Lu, E.-K. Jeong, and J. E. Lainhart. Diffusion tensor imaging of white matter in the superior temporal gyrus and temporal stem in autism. *Neuroscience Letters*, 424(2):127–132, Sep 2007. 19, 88

[105] A. Leung and P. Chue. Sex differences in schizophrenia, a review of the literature. *Acta Psychiatrica Scandinavica Supplementum*, 401:3–38, 2000. 82, 99

[106] C.-P. Lin, V. J. Wedeen, J.-H. Chen, C. Yao, and W.-Y. I. Tseng. Validation of diffusion spectrum magnetic resonance imaging with manganese-enhanced rat optic tracts and ex vivo phantoms. *Neuroimage*, 19(3):482–495, Jul 2003. 14

[107] M.-E. Lynall, D. S. Bassett, R. Kerwin, P. J. McKenna, M. Kitzbichler, U. Muller, and E. Bullmore. Functional connectivity and brain networks in schizophrenia. *Journal of Neuroscience*, 30(28):9477–9487, Jul 2010. 81

[108] V. A. Magnotta, M. L. Adix, A. Caprahan, K. Lim, R. Gollub, and N. C. Andreasen. Investigating connectivity between the cerebellum and thalamus in schizophrenia using diffusion tensor tractography: a pilot study. *Psychiatry Research*, 163(3):193–200, Aug 2008. 92

[109] J. G. Malcolm, M. E. Shenton, and Y. Rathi. Filtered multitensor tractography. *IEEE Transactions on Medical Imaging*, 29(9):1664–1675, Sep 2010. 75

[110] N. T. Markov, P. Misery, A. Falchier, C. Lamy, J. Vezoli, R. Quilodran, M. A. Gariel, P. Giroud, M. Ercsey-Ravasz, L. J. Pilaz, C. Huissoud, P. Barone, C. Dehay, Z. Toroczkai, D. C. V. Essen, H. Kennedy, and K. Knoblauch. Weight consistency specifies regularities of macaque cortical networks. *Cerebral Cortex*, 21(6):1254–1272, Jun 2011. 1

[111] J. Mazziotta, A. Toga, A. Evans, P. Fox, J. Lancaster, K. Zilles, R. Woods, T. Paus, G. Simpson, B. Pike, C. Holmes, L. Collins, P. Thompson, D. MacDonald, M. Iacoboni, T. Schormann, K. Amunts, N. Palomero-Gallagher, S. Geyer, L. Parsons, K. Narr, N. Kabani, G. L. Goualher, D. Boomsma, T. Cannon, R. Kawashima, and B. Mazoyer. A probabilistic atlas and reference system for the human brain: International consortium for brain mapping (icbm). *Philosophical Transactions of the Royal Society B: Biological Sciences*, 356(1412):1293–1322, Aug 2001. 39

[112] J. C. Mazziotta, A. W. Toga, A. Evans, P. Fox, and J. Lancaster. A probabilistic atlas of the human brain: theory and rationale for its development. the international consortium for brain mapping (icbm). *Neuroimage*, 2(2):89–101, Jun 1995. 39

[113] T. McGraw, B. C. Vemuri, B. Yezierski, and T. Mareci. Von mises-fisher mixture model of the diffusion odf. *Proc IEEE Int Symp Biomed Imaging*, 2006:65–68, 2006. 17

[114] M. I. Menzel, E. T. Tan, K. Khare, J. I. Sperl, K. F. King, X. Tao, C. J. Hardy, and L. Marinelli. Accelerated diffusion spectrum imaging in the human brain using compressed sensing. *Magnetic Resonance in Medicine*, 66(5):1226–1233, Nov 2011. 14

[115] K.-D. Merboldt, W. Hanicke, and J. Frahm. Self-diffusion nmr imaging using stimulated echoes. *Journal of Magnetic Resonance (1969)*, 64(3):479–486, Oct. 1985. 1

[116] J. Mintorovitch, M. E. Moseley, L. Chileuitt, H. Shimizu, Y. Cohen, and P. R. Weinstein. Comparison of diffusion- and t2-weighted mri for the early detection of cerebral ischemia and reperfusion in rats. *Magnetic Resonance in Medicine*, 18(1):39–50, Mar 1991. 17

[117] G. Mori. Guiding model search using segmentation. *IEEE International Conference on Computer Vision*, 2:1417–1423, 2005. 42

[118] S. Mori, B. J. Crain, V. P. Chacko, and P. C. van Zijl. Three-dimensional tracking of axonal projections in the brain by magnetic resonance imaging. *Annals of Neurology*, 45(2):265–269, Feb 1999. 12

[119] S. Mori, K. Oishi, H. Jiang, L. Jiang, X. Li, K. Akhter, K. Hua, A. V. Faria, A. Mahmood, R. Woods, A. W. Toga, G. B. Pike, P. R. Neto, A. Evans, J. Zhang, H. Huang, M. I. Miller, P. van Zijl, and J. Mazziotta. Stereotaxic white matter atlas based on diffusion tensor imaging in an icbm template. *Neuroimage*, 40(2):570–582, Apr 2008. 22, 39, 45, 54

[120] N. Morita, M. Harada, H. Otsuka, E. R. Melhem, and H. Nishitani. Clinical application of mr spectroscopy and imaging of brain tumor. *Magnetic Resonance in Medical Sciences*, 9(4):167–175, 2010. 20

[121] M. E. Moseley, Y. Cohen, J. Mintorovitch, L. Chileuitt, H. Shimizu, J. Kucharczyk, M. F. Wendland, and P. R. Weinstein. Early detection of regional cerebral ischemia in cats: comparison of diffusion- and t2-weighted mri and spectroscopy. *Magnetic Resonance in Medicine*, 14(2):330–346, May 1990. 17

[122] M. E. Moseley, J. Kucharczyk, H. S. Asgari, and D. Norman. Anisotropy in diffusion-weighted mri. *Magnetic Resonance in Medicine*, 19(2):321–326, Jun 1991. 10

[123] L. M. Nagae, D. M. Zarnow, L. Blaskey, J. Dell, S. Y. Khan, S. Qasmieh, S. E. Levy, and T. P. L. Roberts. Elevated mean diffusivity in the left hemisphere superior longitudinal fasciculus in autism spectrum disorders increases with more profound language impairment. *American Journal of Neuroradiology*, Apr 2012. 19, 90

[124] K. Oishi, A. Faria, H. Jiang, X. Li, K. Akhter, J. Zhang, J. T. Hsu, M. I. Miller, P. C. M. van Zijl, M. Albert, C. G. Lyketsos, R. Woods, A. W. Toga, G. B. Pike, P. Rosa-Neto, A. Evans, J. Mazziotta, and S. Mori. Atlas-based whole brain white matter analysis using large deformation diffeomorphic metric mapping: application to normal elderly and alzheimer's disease participants. *Neuroimage*, 46(2):486–499, Jun 2009. 22, 30, 39, 41, 45

[125] H. H. Ong, A. C. Wright, S. L. Wehrli, A. Souza, E. D. Schwartz, S. N. Hwang, and F. W. Wehrli. Indirect measurement of regional axon diameter in excised mouse spinal cord with q-space imaging: simulation and experimental studies. *Neuroimage*, 40(4):1619–1632, May 2008. 14

[126] E. Özarslan and T. H. Mareci. Generalized diffusion tensor imaging and analytical relationships between diffusion tensor imaging and high angular resolution diffusion imaging. *Magnetic Resonance in Medicine*, 50(5):955–965, 2003. 15

[127] L. Palaniyappan, V. Balain, J. Radua, and P. F. Liddle. Structural correlates of auditory hallucinations in schizophrenia: A meta-analysis. *Schizophrenia Research*, Feb 2012. 87

[128] R. E. Passingham, K. E. Stephan, and R. Ktter. The anatomical basis of functional localization in the cortex. *Nature Reviews Neuroscience*, 3(8):606–616, Aug 2002. 1

[129] S. Peled, O. Friman, F. Jolesz, and C.-F. Westin. Geometrically constrained two-tensor model for crossing tracts in dwi. *Magnetic Resonance Imaging*, 24(9):1263–1270, Nov 2006. 17

[130] M. Perrin, C. Poupon, B. Rieul, P. Leroux, A. Constantinesco, J.-F. Mangin, and D. Lebihan. Validation of q-ball imaging with a diffusion fibre-crossing phantom on a clinical scanner. *Philosophical Transactions of the Royal Society B: Biological Sciences*, 360(1457):881–891, May 2005. 16

[131] D. L. Pham and J. L. Prince. Adaptive fuzzy segmentation of magnetic resonance images. *IEEE Transactions on Medical Imaging*, 18(9):737–752, Sep 1999. 101

[132] S. Pieper, B. Lorensen, W. Schroeder, and R. Kikinis. The na-mic kit: Itk, vtk, pipelines, grids and 3d slicer as an open platform for the medical image computing community. 04 2006. 7

[133] C. Pierpaoli, P. Jezzard, P. J. Basser, A. Barnett, and G. D. Chiro. Diffusion tensor mr imaging of the human brain. *Radiology*, 201(3):637–648, Dec 1996. 3

[134] D. Pinault. Dysfunctional thalamus-related networks in schizophrenia. *Schizophrenia Bulletin*, 37(2):238–243, Mar 2011. 92

[135] D. Raffelt, J.-D. Tournier, J. Fripp, S. Crozier, A. Connelly, and O. Salvado. Symmetric diffeomorphic registration of fibre orientation distributions. *Neuroimage*, 56(3):1171–1180, Jun 2011. 25

[136] A. Rahimi and B. Recht. Clustering with normalized cuts is clustering with a hyperplane. In *Statistical Learning in Computer Vision*, 2004. 44

[137] A. Rao, A. Smith, R. Schultz, T. Roberts, and R. Verma. Peak geodesic concentration: A measure of wm complexity in hardi. In *IEEE Workshop on Mathematical Methods in Biomedical Image Analysis*, pages 233–238, 2012. 95

[138] Y. Rathi, O. Michailovich, M. E. Shenton, and S. Bouix. Directional functions for orientation distribution estimation. *Medical Image Analysis*, 13(3):432–444, Jun 2009. 17

[139] T. P. L. Roberts, K. M. Cannon, K. Tavabi, L. Blaskey, S. Y. Khan, J. F. Monroe, S. Qasmieh, S. E. Levy, and J. C. Edgar. Auditory magnetic mismatch field latency: a biomarker for language impairment in autism. *Biological Psychiatry*, 70(3):263–269, Aug 2011. 91

[140] E. C. Robinson, A. Hammers, A. Ericsson, A. D. Edwards, and D. Rueckert. Identifying population differences in whole-brain structural networks: a machine learning approach. *Neuroimage*, 50(3):910–919, Apr 2010. 56

[141] M. Rubinov and O. Sporns. Complex network measures of brain connectivity: uses and interpretations. *Neuroimage*, 52(3):1059–1069, Sep 2010. 73, 80

[142] B. Scherrer and S. K. Warfield. Optimal hardi acquisition schemes for multi-tensor models. In *Proceedings of the 18th Annual Meeting of ISMRM*, 2010. 17

[143] B. Scherrer and S. K. Warfield. Why multiple b-values are required for multi-tensor models. evaluation with a constrained log-euclidean model. In *Proc. IEEE Int Biomedical Imaging: From Nano to Macro Symp*, pages 1389–1392, 2010. 17

[144] J. D. Schmahmann and D. N. Pandya. Cerebral white matter–historical evolution of facts and notions concerning the organization of the fiber pathways of the brain. *Journal of the History of the Neurosciences*, 16(3):237–267, 2007. 1

[145] J. D. Schmahmann, D. N. Pandya, R. Wang, G. Dai, H. E. D'Arceuil, A. J. de Crespigny, and V. J. Wedeen. Association fibre pathways of the brain: parallel observations from diffusion spectrum imaging and autoradiography. *Brain*, 130(Pt 3):630–653, Mar 2007. 1, 2

[146] G. L. Schmidt, M. M. Rey, J. E. O. Cardy, and T. P. L. Roberts. Absence of m100 source asymmetry in autism associated with language functioning. *Neuroreport*, 20(11):1037–1041, Jul 2009. 91

[147] M. E. Shenton, C. C. Dickey, M. Frumin, and R. W. McCarley. A review of mri findings in schizophrenia. *Schizophrenia Research*, 49(1-2):1–52, Apr 2001. 87

[148] J. H. Sherman, K. Hoes, J. Marcus, R. J. Komotar, C. W. Brennan, and P. H. Gutin. Neurosurgery for brain tumors: update on recent technical advances. *Current Neurology and Neuroscience Reports*, 11(3):313–319, Jun 2011. 20

[149] J. Shi and J. Malik. Normalized cuts and image segmentation. *IEEE Transactions on Pattern Analysis and Machine Intelligence*, 22(8):888–905, 2000. 44

[150] D. K. Shukla, B. Keehn, A. J. Lincoln, and R.-A. Mller. White matter compromise of callosal and subcortical fiber tracts in children with autism spectrum disorder: a diffusion tensor imaging study. *Journal of the American Academy of Child and Adolescent Psychiatry*, 49(12):1269–78, 1278.e1–2, Dec 2010. 19

[151] D. K. Shukla, B. Keehn, and R.-A. Mller. Tract-specific analyses of diffusion tensor imaging show widespread white matter compromise in autism spectrum disorder. *Journal of Child Psychology and Psychiatry*, 52(3):286–295, Mar 2011. 19

[152] J. G. Sled, A. P. Zijdenbos, and A. C. Evans. A nonparametric method for automatic correction of intensity nonuniformity in mri data. *IEEE Transactions on Medical Imaging*, 17(1):87–97, Feb 1998. 101

[153] S. M. Smith. Fast robust automated brain extraction. *Human Brain Mapping*, 17(3):143–155, Nov 2002. 101

[154] A. G. Sorensen, O. Wu, W. A. Copen, T. L. Davis, R. G. Gonzalez, W. J. Koroshetz, T. G. Reese, B. R. Rosen, V. J. Wedeen, and R. M. Weisskoff. Human acute cerebral ischemia: detection of changes in water diffusion anisotropy by using mr imaging. *Radiology*, 212(3):785–792, Sep 1999. 17

[155] C. H. Sotak. The role of diffusion tensor imaging in the evaluation of ischemic brain injury - a review. *NMR in Biomedicine*, 15(7-8):561–569, 2002. 17, 18

[156] E. R. Sowell, A. W. Toga, and R. Asarnow. Brain abnormalities observed in childhood-onset schizophrenia: a review of the structural magnetic resonance imaging literature. *Mental Retardation and Developmental Disabilities Research Reviews*, 6(3):180–185, 2000. 87

[157] O. Sporns. The human connectome: a complex network. *Annals of the New York Academy of Sciences*, 1224(1):109–125, Apr 2011. 1

[158] E. O. Stejskal. Use of spin echoes in a pulsed magnetic-field gradient to study anisotropic, restricted diffusion and flow. *The Journal of Chemical Physics*, 43(10):3597–3603, 1965. 1, 9

[159] E. O. Stejskal and J. E. Tanner. Spin diffusion measurements: Spin echoes in the presence of a time-dependent field gradient. *The Journal of Chemical Physics*, 42(1):288–292, 1965. 1

[160] K. E. Stephan, K. J. Friston, and C. D. Frith. Dysconnection in schizophrenia: from abnormal synaptic plasticity to failures of self-monitoring. *Schizophrenia Bulletin*, 35(3):509–527, May 2009. 87

[161] S. K. Sundaram, A. Kumar, M. I. Makki, M. E. Behen, H. T. Chugani, and D. C. Chugani. Diffusion tensor imaging of frontal lobe in autism spectrum disorder. *Cerebral Cortex*, 18(11):2659–2665, Nov 2008. 19, 88

[162] J. Talairach. *Co-Planar Stereotaxic Atlas of the Human Brain: 3-D Proportional System: An Approach to Cerebral Imaging*. Thieme, 1988. 39

[163] J. P. Thirion. Image matching as a diffusion process: an analogy with maxwell's demons. *Medical Image Analysis*, 2(3):243–260, Sep 1998. 25

[164] M. E. Thomason and P. M. Thompson. Diffusion imaging, white matter, and psychopathology. *Annual Review of Clinical Psychology*, 7:63–85, Apr 2011. 18, 19

[165] A. W. Toga, P. M. Thompson, S. Mori, K. Amunts, and K. Zilles. Towards multimodal atlases of the human brain. *Nature Reviews Neuroscience*, 7(12):952–966, Dec 2006. 24, 39

[166] J.-D. Tournier, F. Calamante, and A. Connelly. Robust determination of the fibre orientation distribution in diffusion mri: Non-negativity constrained super-resolved spherical deconvolution. *Neuroimage*, 35(4):1459–1472, May 2007. 16, 46, 101

[167] J.-D. Tournier, F. Calamante, D. G. Gadian, and A. Connelly. Direct estimation of the fiber orientation density function from diffusion-weighted mri data using spherical deconvolution. *NeuroImage*, 23(3):1176–1185, Nov. 2004. 16

[168] J.-D. Tournier, C.-H. Yeh, F. Calamante, K.-H. Cho, A. Connelly, and C.-P. Lin. Resolving crossing fibres using constrained spherical deconvolution: Validation using diffusion-weighted imaging phantom data. *Neuroimage*, May 2008. 3, 4, 5

[169] A. Tristn-Vega and S. Aja-Fernndez. Dwi filtering using joint information for dti and hardi. *Medical Image Analysis*, 14(2):205–218, Apr 2010. 100

[170] A. Tristn-Vega, C.-F. Westin, and S. Aja-Fernndez. A new methodology for the estimation of fiber populations in the white matter of the brain with the funk-radon transform. *Neuroimage*, 49(2):1301–1315, Jan 2010. 3, 15

[171] V. Tsiaras, P. G. Simos, R. Rezaie, B. R. Sheth, E. Garyfallidis, E. M. Castillo, and A. C. Papanicolaou. Extracting biomarkers of autism from meg resting-state functional connectivity networks. *Computers in Biology and Medicine*, 41(12):1166–1177, Dec 2011. 88

[172] D. S. Tuch. *Diffusion MRI of Complex Tissue Structure*. PhD thesis, Harvard University and Massachusetts Institute of Technology, 2002. 3, 14, 15, 78

[173] D. S. Tuch. Q-ball imaging. *Magnetic Resonance in Medicine*, 52(6):1358–1372, Dec 2004. 3

[174] D. S. Tuch, R. Weisskoff, J. W. Belliveau, and V. J. Wedeen. High angular resolution diffusion imaging of the human brain. In *In: Proc 7th Annual Meeting ISMRM*, page 321, 1999. 3, 13

[175] M. P. van den Heuvel, R. C. W. Mandl, C. J. Stam, R. S. Kahn, and H. E. H. Pol. Aberrant frontal and temporal complex network structure in schizophrenia: a graph theoretical analysis. *Journal of Neuroscience*, 30(47):15915–15926, Nov 2010. 19

[176] T. Vercauteren, X. Pennec, A. Perchant, and N. Ayache. Diffeomorphic demons: efficient non-parametric image registration. *Neuroimage*, 45(1 Suppl):S61–S72, Mar 2009. 25

[177] J. S. Verhoeven, P. D. Cock, L. Lagae, and S. Sunaert. Neuroimaging of autism. *Neuroradiology*, 52(1):3–14, Jan 2010. 48

[178] S. Wakana, H. Jiang, L. M. Nagae-Poetscher, P. C. M. van Zijl, and S. Mori. Fiber tract-based atlas of human white matter anatomy. *Radiology*, 230(1):77–87, Jan 2004. 22, 39

[179] Q. Wang, T.-P. Su, Y. Zhou, K.-H. Chou, I.-Y. Chen, T. Jiang, and C.-P. Lin. Anatomical insights into disrupted small-world networks in schizophrenia. *Neuroimage*, 59(2):1085–1093, Jan 2012. 19

[180] S. K. Warfield, K. H. Zou, and W. M. Wells. Simultaneous truth and performance level estimation (staple): an algorithm for the validation of image segmentation. *IEEE Transactions on Medical Imaging*, 23(7):903–921, Jul 2004. 40

[181] V. J. Wedeen, P. Hagmann, W.-Y. I. Tseng, T. G. Reese, and R. M. Weisskoff. Mapping complex tissue architecture with diffusion spectrum magnetic resonance imaging. *Magnetic Resonance in Medicine*, 54(6):1377–1386, Dec 2005. 3

[182] V. J. Wedeen, T. G. Reese, D. S. Tuch, M. Wiegel, J. Dou, R. Weisskoff, and D. Chessler. Mapping fiber orientation spectra in cerebral white matter with fourier transform diffusion mri. In *Proceedings of the International Society of Magnetic Resonance in Medicine*, 2000. 14, 15

[183] V. J. Wedeen, R. P. Wang, J. D. Schmahmann, T. Benner, W. Y. I. Tseng, G. Dai, D. N. Pandya, P. Hagmann, H. D'Arceuil, and A. J. de Crespigny. Diffusion spectrum magnetic resonance imaging (dsi) tractography of crossing fibers. *Neuroimage*, 41(4):1267–1277, Jul 2008. 3

[184] G. E. Wesbey, M. E. Moseley, and R. L. Ehman. Translational molecular self-diffusion in magnetic resonance imaging. ii. measurement of the self-diffusion coefficient. *Investigative Radiology*, 19(6):491–498, 1984. 1

[185] C.-F. Westin, S. E. Maier, H. Mamata, A. Nabavi, F. A. Jolesz, and R. Kikinis. Processing and visualization for diffusion tensor mri. *Medical Image Analysis*, 6(2):93–108, Jun 2002. 9, 11

[186] T. White, M. Nelson, and K. O. Lim. Diffusion tensor imaging in psychiatric disorders. *Topics in Magnetic Resonance Imaging*, 19(2):97–109, Apr 2008. 19

[187] B. Wicker, P. Fonlupt, B. Hubert, C. Tardif, B. Gepner, and C. Deruelle. Abnormal cerebral effective connectivity during explicit emotional processing in adults with autism spectrum disorder. *Social Cognitive and Affective Neuroscience*, 3(2):135–143, Jun 2008. 88

[188] D. Xu, S. Mori, D. Shen, P. C. M. van Zijl, and C. Davatzikos. Spatial normalization of diffusion tensor fields. *Magnetic Resonance in Medicine*, 50(1):175–182, Jul 2003. 22, 27

[189] J. Yang, D. Shen, C. Davatzikos, and R. Verma. Diffusion tensor image registration using tensor geometry and orientation features. In *Medical Image Computing and Computer Assisted Intervention*, 2008. 24

[190] P.-T. Yap, Y. Chen, H. An, Y. Yang, J. H. Gilmore, W. Lin, and D. Shen. Sphere: Spherical harmonic elastic registration of hardi data. *Neuroimage*, 55(2):545–556, Mar 2011. 25

[191] B. Yeo, T. Vercauteren, P. Fillard, X. Pennec, P. Golland, N. Ayache, and O. Clatz. Dt-refind: Diffusion tensor registration with exact finite-strain differential. *IEEE Transactions on Medical Imaging*, Jun 2009. 22, 24

[192] Q. Yu, J. Sui, S. Rachakonda, H. He, W. Gruner, G. Pearlson, K. A. Kiehl, and V. D. Calhoun. Altered topological properties of functional network connectivity in schizophrenia during resting state: a small-world brain network study. *PLoS One*, 6(9):e25423, 2011. 55, 81

[193] A. Zalesky, A. Fornito, I. H. Harding, L. Cocchi, M. Ycel, C. Pantelis, and E. T. Bullmore. Whole-brain anatomical networks: does the choice of nodes matter? *Neuroimage*, 50(3):970–983, Apr 2010. 55, 73

[194] A. Zalesky, A. Fornito, M. L. Seal, L. Cocchi, C.-F. Westin, E. T. Bullmore, G. F. Egan, and C. Pantelis. Disrupted axonal fiber connectivity in schizophrenia. *Biological Psychiatry*, 69(1):80–89, Jan 2011. 19

[195] W. Zhan and Y. Yang. How accurately can the diffusion profiles indicate multiple fiber orientations? a study on general fiber crossings in diffusion mri. *Journal of Magnetic Resonance*, 183(2):193–202, Dec 2006. 15

[196] H. Zhang, B. B. Avants, P. A. Yushkevich, J. H. Woo, S. Wang, L. F. McCluskey, L. B. Elman, E. R. Melhem, and J. C. Gee. High-dimensional spatial normalization of diffusion tensor images improves the detection of white matter differences: an example study using amyotrophic lateral sclerosis. *IEEE Transactions on Medical Imaging*, 26(11):1585–1597, Nov 2007. 24, 40

[197] H. Zhang, P. A. Yushkevich, D. C. Alexander, and J. C. Gee. Deformable registration of diffusion tensor mr images with explicit orientation optimization. *Medical Image Analysis*, 10(5):764–785, Oct 2006. 22

[198] Y. Zhang, M. Brady, and S. Smith. Segmentation of brain mr images through a hidden markov random field model and the expectation-maximization algorithm. *IEEE Transactions on Medical Imaging*, 20(1):45–57, Jan 2001. 30

[199] K. Zilles and K. Amunts. Receptor mapping: architecture of the human cerebral cortex. *Curr Opin Neurol*, 22(4):331–339, Aug 2009. 96